NASA Contractor Report 3471

Analytical and Experimental Study of Flow Phenomena in Noncavitating Rocket Pump Inducers

B. Lakshminarayana

GRANT NGL-39-009-007
OCTOBER 1981

NASA

NASA Contractor Report 3471

Analytical and Experimental Study of Flow Phenomena in Noncavitating Rocket Pump Inducers

B. Lakshminarayana
The Pennsylvania State University
University Park, Pennsylvania

Prepared for
Lewis Research Center
under Grant NGL-39-009-007

National Aeronautics
and Space Administration

**Scientific and Technical
Information Branch**

1981

TABLE OF CONTENTS

NOMENCLATURE

C	chord length
C_f	skin friction coefficient $(2\tau_o/\rho W_e^2)$
d_h	hydraulic mean diameter
E	output D.C. voltage of anemometer
e	output A.C. voltage of anemometer
E_o	D.C. voltage of hot wire anemometer at zero velocity
H	stagnation head rise (in absolute flow)/shape factor
H_E	head rise derived from Euler's Equation (UV_θ/g)
H_{loss}	$H_E - H_m$
H_m	measured stagnation head rise (in absolute flow)
H_{sv}	net positive suction head, ft.
h	static head
N	number of blades
O	throttle opening
p	static pressure
P_o	stagnation pressure
P_{OR}	stagnation pressure of the relative flow
Q	flow rate, gpm
R	r/r_t
R_e	Reynolds number based on blade tip speed $(U_t\ r_t/\nu)$
R_{ht}	hub/tip ratio
R_N	Reynolds number, $\bar{W}\ d_h/\nu$
r,θ,z	radial, tangential, and axial coordinates
SS	suction specific speed, $N\sqrt{Q}/H_{sv}^{3/4}$, $RPM\sqrt{GPM}/(Feet)^{3/4}$
S	blade spacing
U	blade speed
V	resultant absolute velocity
v	fluctuating component of absolute velocity
V_r,V_θ,V_z	radial, tangential and axial component of absolute velocity
W	resultant relative velocity
W_r,W_θ,W_z	radial, tangential and axial component of relative velocity
w	fluctuating component of relative velocity
x,y	coordinates parallel to and perpendicular to blade camber line and lying on a cylindrical surface
x_t	distance between leading edge and the location of transition point
ε	angle between limiting streamline and x direction
β	relative air angle measured from axial direction
λ_R	friction coefficient for a rotating channel
ν	kinematic viscosity
ρ	density
ϕ	flow coefficient, $W_z/\Omega r_t$

ψ_E	$2gH_E/U_t^2$
ψ_{loss}	$2gH_{loss}/U_t^2$
ψ_S	$2gH/U_t^2$ (static head rise coefficient)
ψ_t	stagnation head rise coefficient, $2gH/U_t^2$
ψ_R	stagnation head coefficient of relative flow, $2P_{OR}/\rho U_t^2$
Ω	angular velocity
η	hydraulic efficiency, ψ_t/ψ_E
ζ	$\psi_E - \psi_t$
θ_{11}	momentum thickness in x direction
$R_{\theta_{11}}$	$W_e\theta_{11}/\nu$
σ	solidity (C/S)
τ	shear stress
σ	normal stress

Subscripts

o	free stream values
h	hub
m	values at mid passage
r,θ,z	components along r,θ,z directions
t	tip
x,y	components along x,y directions
1	inlet
2	outlet
e	edge of the boundary layer

Superscript

—	mass averaged over the entire passage/circumferential average

SUMMARY

The investigation of the flow phenomena in rocket pump inducers carried out at The Pennsylvania State University is summarized in this report. All the experimental investigations were carried out with air as the test medium.

The major characteristic features of the rocket pump inducers are low flow coefficient (0.05 to 0.2), large stagger angle (70 deg to 85 deg) and high-solidity (few blades of very long chord length as opposed to short chord of many bladed compressor rotor) blades of little or no camber. The resulting configuration, even though beneficial from the point of view of cavitation, results in highly viscous, turbulent, and, almost invariably, fully developed flow inside these passages. This results in a large departure from idealized and design fluid-dynamic performance. Under these circumstances, the flow will be dominated by viscous and secondary flow with a large departure from the design flow. While the characteristic form of the inducer is dictated by cavitation requirements, the flow is subjected to major effects of viscosity and turbulence of the flow in the long and narrow passages. The investigations reported here are concerned with the effect of viscosity, not the effects of cavitation.

One of the major objectives of this investigation is to understand the flow phenomena in these inducers, through flow visualization, conventional and hot-wire probe measurement inside and at the exit of the blade passage, and to provide analytical methods for the prediction of flow through inducers. To achieve the objectives mentioned above, the experimental work was carried out using four-, three-, and two-bladed inducers with cambered blades. Both the passage and the exit flow were measured. The basic research and boundary layer investigation was carried out using a helical flat plate (of same dimensions as the inducer blades tested), and a flat plate helical inducer (four-bladed). The flow measurements were carried out using tri-axial hot wire probes and pitot probes. Detailed mean and turbulence flow field inside the passage as well as the exit of the rotor were derived from these measurements. The boundary layer, endwall and other passage data revealed extremely complex nature of the flow, with major effects of viscosity present across the entire passage.

Several analyses were carried out to predict the flow field in inducers. These included an approximate analysis, the shear pumping analysis, and a numerical solution of exact viscous equations with approximate modelling for the viscous terms. The agreement between these analyses and the experiment is reasonably good.

INTRODUCTION

The turbopumps used in liquid rocket feed systems operate at high speeds so as to minimize weight and size of the system--an important design criteria for an aerospace vehicle. The conventional pumps cavitate at suction-specific speeds (S) in excess of 8,000. The need to increase the speed led to the development of a cavitation-resistance inducer, which is essentially an axial-flow pump with high-solidity blades used in front of the main pump. Inducers are also used in other industrial (e.g., centrifugal compressors, fire-fighting equipment, etc.) and marine propulsion systems.

The inducer usually contains fewer blades (usually three to four) than conventional pumps. Long and narrow passages provide the time and space for the collapse of the cavitation bubbles and for the gradual addition of energy. The blades in most practical inducers used in rocket pumps wrap around almost 360 deg. The purpose of the inducer is to pressurize the flow sufficiently to enable the main pump to operate satisfactorily. The physical reasoning for the selection of such unconventional pumps is described by Acosta [1]. Inducers have operated successfully at suction-specific speeds (S) in excess of 30,000. The test inducer described later is designed for a suction specific speed (S) of 50,000.

The major characteristic features of the inducer are low flow coefficient (0.05 to 0.2), large stagger angle (70 deg to 85 deg), and high-solidity (few blades of very long chord length as opposed to short chords of a many-bladed compressor rotor) blades of little or no camber. The resulting configuration, even though beneficial from the point of view of cavitation, results in highly viscous, turbulent, and, almost invariably, fully developed flow inside these passages. This results in a large departure from idealized and design fluid dynamic performance. Under these circumstances, the flow will be dominated by viscous and secondary flow, with a large departure from the design flow.

While the characteristic form of the inducer is dictated by cavitation requirements, the flow is subjected to major effects of viscosity and turbulence of the flow in the long and narrow passages. The investigations reported here are concerned with the effect of viscosity, not the effects of cavitation. The results reported in the paper are based on a systematic investigation of flow behavior in an inducer undertaken at the Department of Aerospace Engineering at The Pennsylvania State University. One of the major objectives of this investigation is to understand the flow phenomena in these inducers, through flow visualization and conventional and hot-wire probe measurement inside and at the exit of the blade passage, and to provide analytical methods for the prediction of flow through inducers.

The mechanism by which the stagnation- and static-pressure rise takes place in inducers is due to a curious combination of inviscid turning effects and shear forces; while the former has a dominant influence in conventional machinery such as compressors and pumps, the shear forces dominate the flow in inducers, at least near the tip. The viscous and turbulence effects in these blade rows are not confined to thin regions at the blades and in the end zones, but extend over the entire cross section of the flow. It is therefore also an objective of the investigation to gain qualitative and quantitative understanding of viscous, turbulent, and secondary flows in such turbomachinery. It is hoped that the analysis, data, and correlations developed in this investigation will serve to establish analytical methods for the analysis and modelling of turbomachinery flows dominated by viscous, turbulent, and secondary flow effects and under conditions where the real fluid effects are at least as important as the ideal effects which form the basis of the existing design.

The boundary layers that develop on the blades of rotating machinery such as compressors, pumps, inducers, propellers, and turbines are not two-dimensional. The rotation of the blade produces spanwise flow, resulting in a skewed or three-dimensional boundary layer. The extent of three-dimensionality depends on the angular velocity, the flow coefficient, space/chord ratio, aspect ratio, stagger angle of the blade, etc. A basic understanding of the effects of centrifugal and Coriolis forces on the boundary layer behavior is essential for the improved analysis and performance of such rotating fluid machinery. The radial flow inside the boundary layer, when encountered by the annulus wall, produces a complex flow near the tip, resulting in radially inward flow. These and other interaction effects result in extremely complex boundary layer characteristics. It is one of the additional objectives of this report to study the influence of these rotation and "channel effects" on the three-dimensional turbulent boundary layers encountered in turbomachinery passages. In view of our limited knowledge of the effects of Coriolis and centrifugal forces, it is desirable to use a model where the pressure gradient effects are small, so that the major effects of rotation can be discerned. With this in mind, the flow in and around a single helical blade and a rotating channel with mild pressure gradient is studied. This is accomplished by operating the rotor without any throttle. However, the analysis developed is more general and not restricted to any particular pressure gradient.

To achieve the objectives mentioned above, the experimental work was carried out using four-, three-, and two-bladed inducers with cambered blades. Both the passage and the exit flow were measured. The basic research and boundary layer investigation was carried out using a helical flat plate (of the same dimensions as the inducer blades tested) and a flat-plate helical inducer (four-bladed).

Acosta [1] was the first one to provide experimental evidence on the unusual behavior of such pumps; namely, large head rise near the tip and low axial velocities near the hub. Later measurements by Sandercock et al. [2], Soltis et al. [3], and Anderson et al. [4] brought out clearly the complicated nature of the flow in such inducers. These extensive measurements related to overall performance led to the subsequent study carried out at The Pennsylvania State University and reported in references [5] through [25]. The study reported in references [5] through [25] are carried out with air as the test medium, using several 0.915 m diameter inducers, the number of blades varying from 1 to 4. Most of these inducers are operated at a flow coefficient, ϕ, of 0.065. A summary of the configurations used, the nature of measurements taken, and the references where they were reported are tabulated in Table 1. Only a brief summary of the results and re-interpretation of some of the data are given here. No attempt is made to present all the results; mention is made of only those results that are of significant interest. The reader is referred to references [5] through [25] for details. Wherever possible, some of the unpublished results are presented.

Table 1

SUMMARY OF THE INDUCER INVESTIGATION AT THE PENNSYLVANIA STATE UNIVERSITY

Tip Diameter = 0.915 m, Reynolds number based on radius and blade speed at tip = 6.6×10^5

Configuration	Design	C^* in.	(C^*/S^*)	β_1^* degrees	$(\beta_1)_{hub}$ degrees	ϕ	Measurements and analysis carried out	Refs. where reported
Four-bladed inducer	Cambered blades-free vortex design	83	2.86	86° 15'	75° 30'	0.065	Flow visualization inside the passage; exit, entry, and passage flow measured with a pitot probe. Approximate analyses	5, 6, 7, 11, 12, 15, 16, 25
Four-bladed inducer	Flat plate	95	3.4	84°	78°	0.04 to 0.067 & open throttle	Exit flow measurement; extensive hot-wire measurement at 1600 locations inside the passage to define mean velocity, turbulence intensity, and stress; blade static-pressure and skin-friction stress. Boundary layer analysis	10, 14, 22, 23, 24
Three-bladed inducer	Cambered blades	83	2.14	86° 15'	75° 30'	0.065	Exit and entry flow using both hot-wire and pitot probe, hot-wire probe measurements inside the passage. Numerical solution of inviscid and viscid equations.	10, 11, 14, 16, 17, 18, 19, 20, 21, 25

Table 1 (continued)

Configuration	Design	C* in.	(C*/S*)	β_1^* degrees	$(\beta_1)_{hub}$ degrees	ϕ	Measurements and analysis carried out	Refs. where reported
Two-bladed inducer	Cambered blades	83	2.14	86° 15'	75° 30'	0.065	Exit and entry flow measurements.	11
Single blade	Flat plate	95		84°	78°	open throttle	Mostly three-dimensional turbulent boundary layer measurements.	8, 9, 10, 13

* Values at the tip

EXPERIMENTAL FACILITIES AND MEASUREMENT TECHNIQUES

Experimental Facilities

A photograph of the test facility used in the experimental investigation of flow phenomena in inducers is shown in Figure 1a. All the inducers, rotating helical blade and rotating helical channel, were driven at 450 rpm by a 5 hp variable-speed motor. The flow medium was air.

The inducer was designed by the mean streamline method presented by Wislicenus [26], taking into account the change in axial velocity through the blade row. The blade sections are shown in Figure 1b and some important geometrical and design parameters are listed in Table 2. The blades were made of fiberglass using the mold construction shown in Figure 1c. Details of the design techniques and the facility are given in references [5] and [15]. The inducer blades and the facility shown in Figure 1a were employed for all the inducers tested (four-, three-, and two-bladed).

The inducer facility was modified for the boundary layer investigation. The modified facility for a single blade is shown in Figure 2. The facility for the flat-plate helical inducer experiment is shown schematically in Figure 3a, and a photograph of the rotor is shown in Figure 3b. The rotor consisted of four, equally spaced, transparent plexiglass helical blades of constant thickness (1.27 cm), an axial advance of 25.4 cm, and an angular extent of 300 deg. The blade stagger angle varied from 78 deg at the hub to 84 deg at the tip. Other dimensions of the rotor and facility are shown in Figure 3a. To facilitate blade static pressure and limiting of streamline angle measurements, the adjoining blades of the channel had 11 static-pressure taps at each of the five axial locations. One of the unique features of this facility was the traverse unit for the rotating probe measurements. It consisted of a light traverse disk driven by a fractional-horsepower step motor. The probe holder and the probe were mounted on the traverse disk. The probe, which was located inside the passage, traversed in a slot in the hub. The traverse disk and the probe could be traversed circumferentially in steps of 1.8 deg by the stepping motor, thus enabling accurate location and measurement of the flow characteristics inside the blade boundary layers. The motor was powered and controlled by a stationary traverse indexing device through an eight-channel slip-ring unit. The traverse unit and the probe were locked, except when indexed. Thus, the circumferential traverse could be accomplished, through the remotely controlled index device, without stopping the rotor. The radial movement of the probe was carried out manually. Once all the radial and circumferential traverses had been completed, the entire traverse assembly was moved to a different axial location and the measurements repeated. The instrument package, consisting of a commercial slip-ring unit, a mercury slip-ring unit, and a pressure transfer device, were housed in a stationary cowling attached to the nose cone, as shown in Figure 3a. This inducer was operated at various flow coefficients at 450 rpm, as shown in Table 1.

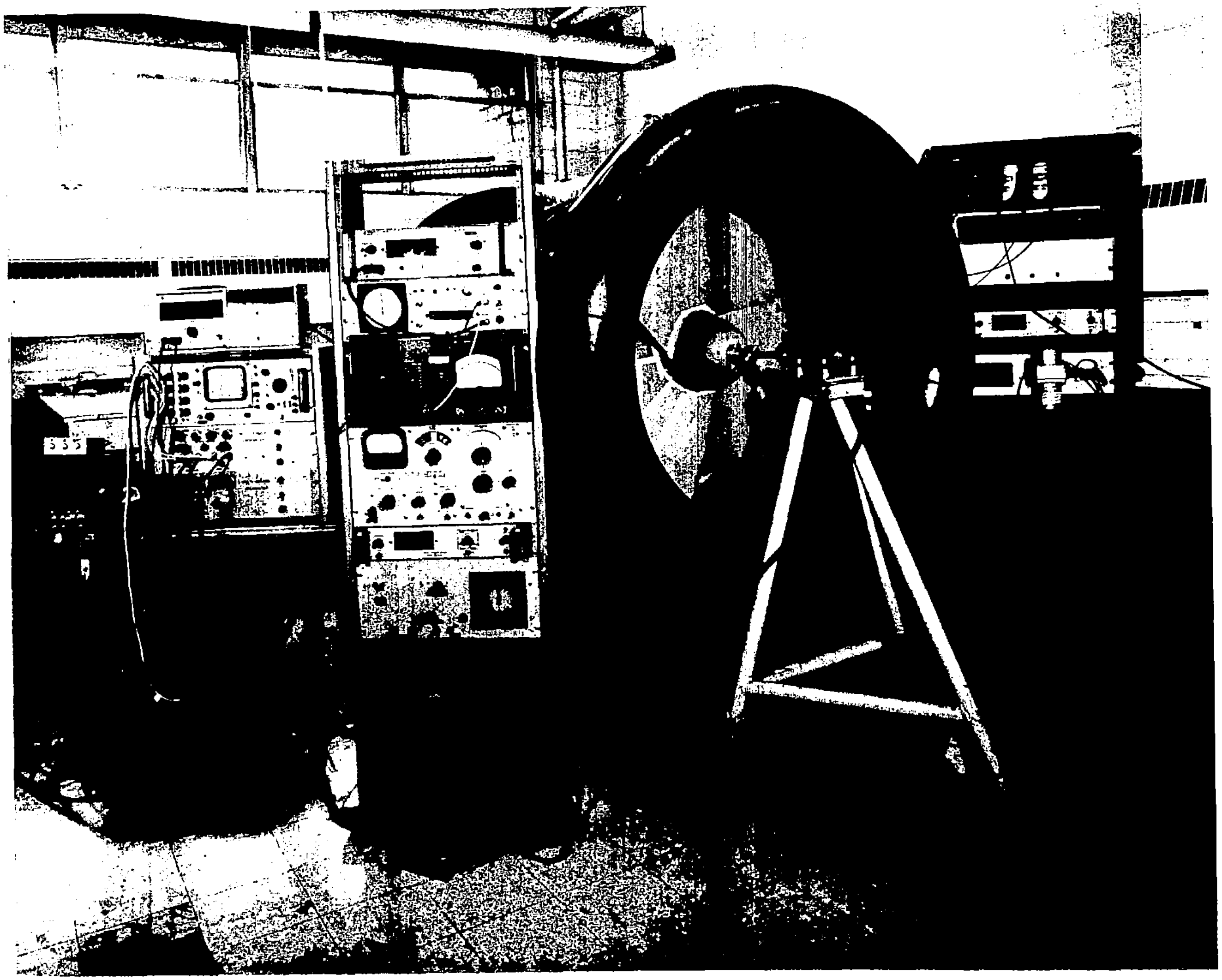

Figure 1a. Photograph of the Inducer Test Facility

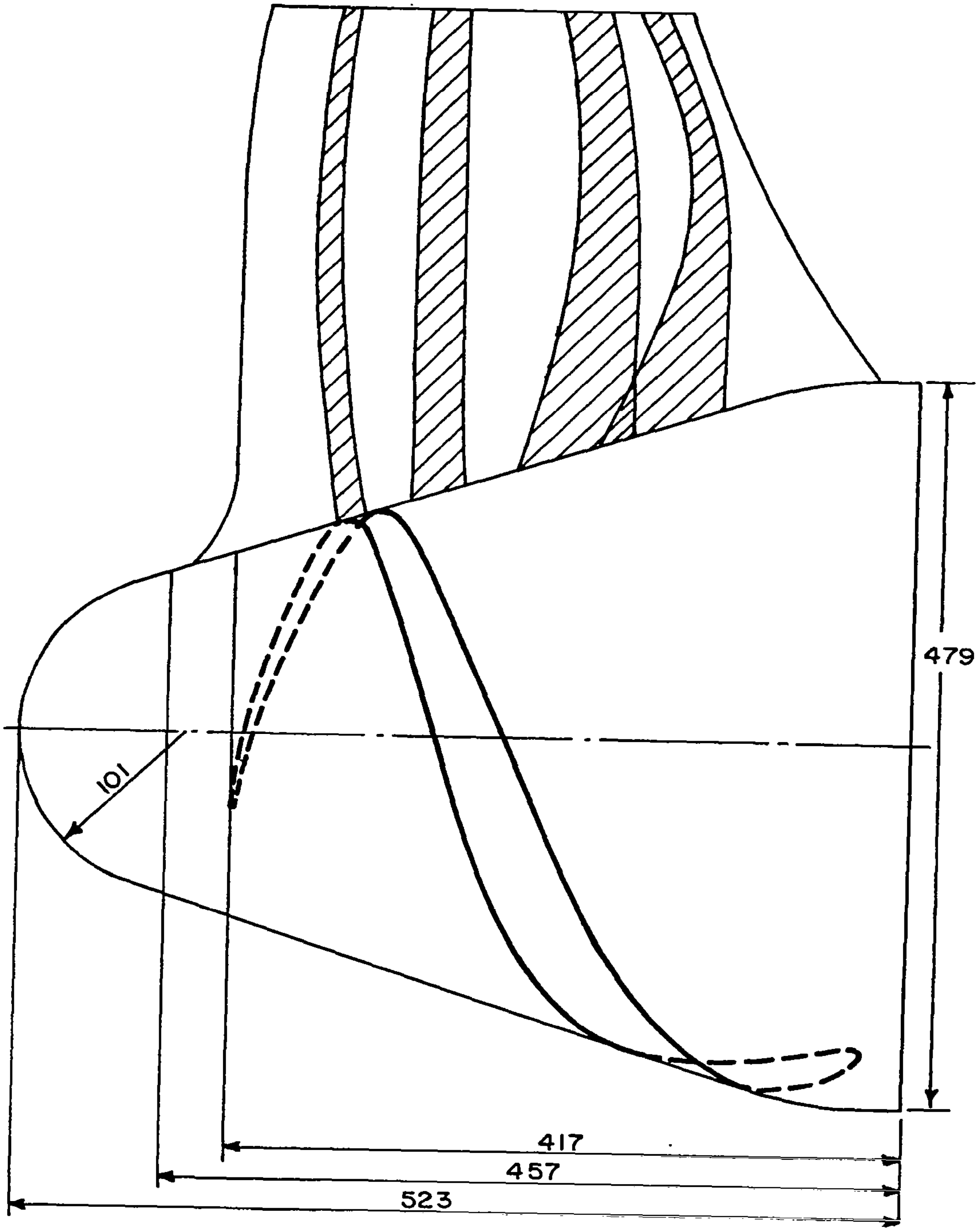

ALL DIMENSIONS ARE IN M.M.

Figure 1b. Chordwise and Radial Profiles of the Inducer Blade

Table 2

INDUCER CHARACTERISTICS

Tip diameter		0.915 m
Hub/tip ratio at outlet		0.5
Hub/tip ratio at inlet		0.25
Radial clearance		1.5 mm
Suction specific speed SS (design)		50.000
Flow coefficient ($\phi = V_z/U_t$) (design)		0.065
Blade chord	Tip ($R = 1.0$)	2.1 m
	Mid-span ($R = 0.75$)	1.6 m
	Hub ($R = 0.5$)	1.26 m
Solidity (four-bladed inducer)	Tip ($R = 1.0$)	2.86
	Mid-span ($R = 0.75$)	2.91
	Hub ($R = 0.5$)	3.50
Number of vanes		4, 3, 2
Angular wrap (average)		290°
Lift coefficient of the blade based on mean velocity (four-bladed inducer)	Tip	0.0966
	Mid-span	0.163
	Hub	0.307
Reynolds number based on tip radius		6.60×10^5
Reynolds number based on relative velocity and chord at mid-radius		1.75×10^6
Maximum deviation of camber line from mean streamline $(\Delta\eta/L)_{max}$	($R = 0.5$)	0.02
	($R = 0.75$)	0.01075
	($R = 1.0$)	0.00637
Blade angles at inlet	($R = 0.25$)	75°30'
	($R = 0.625$)	83°30'
	($R = 1.0$)	86°15'

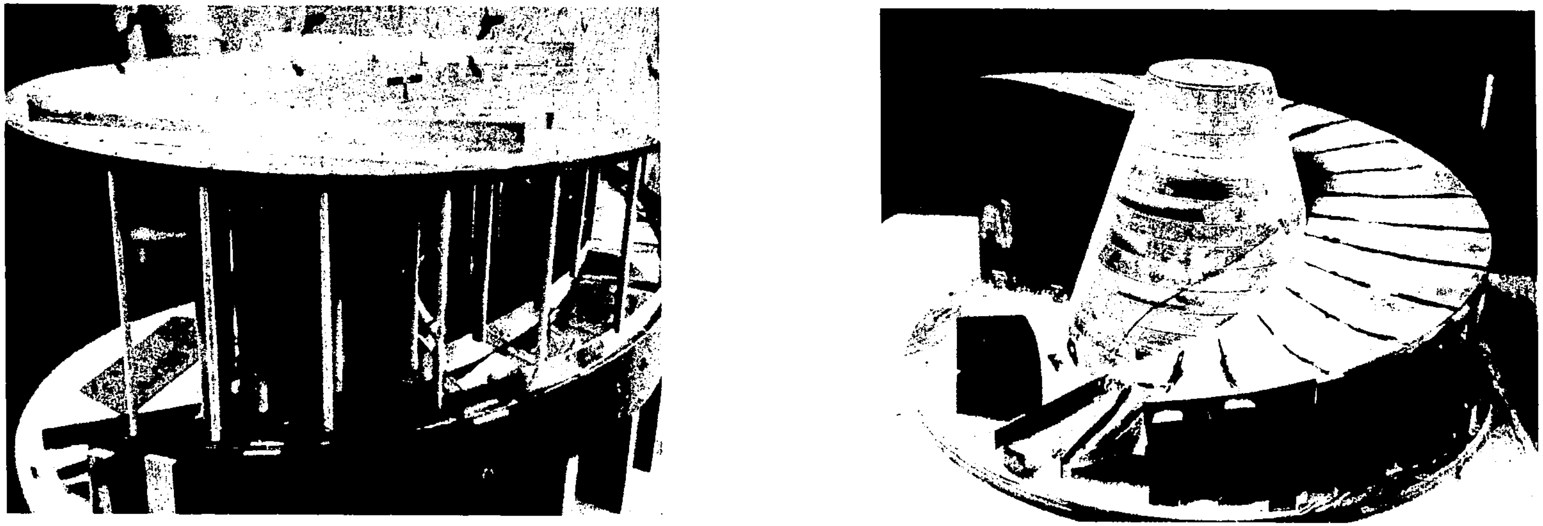

Mold Framework for the Suction Surface

Mold Assembly for Both Pressure and Suction Surface

Figure 1c. Mold Assembly for Inducer Blade.

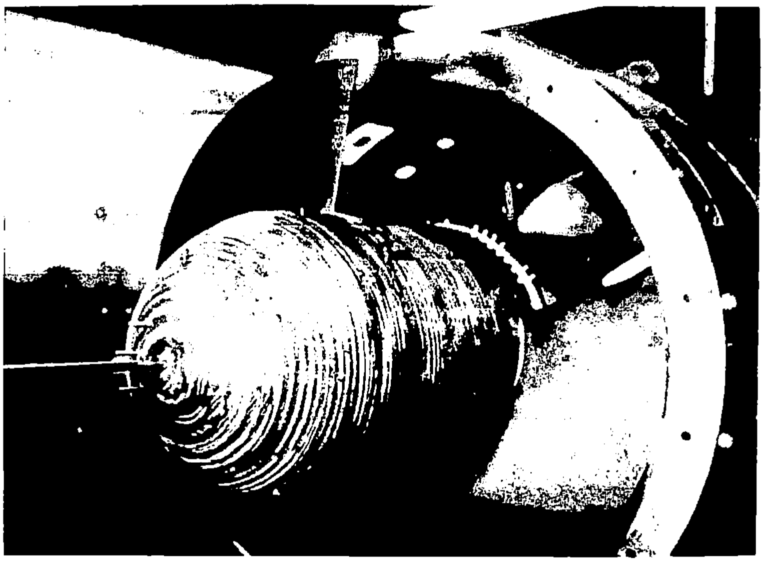

Photograph of the Helical Blade

(with annulus wall removed)

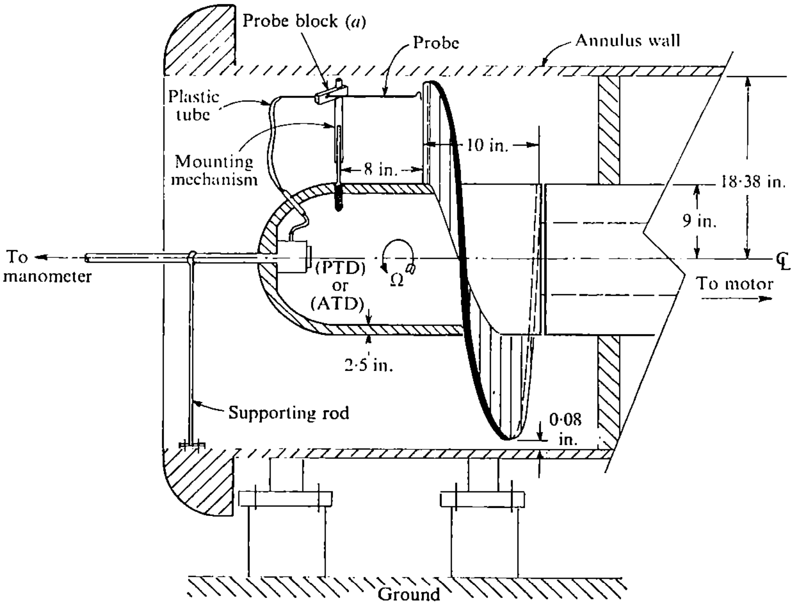

Figure 2. Photograph and Schematic of the Test Assembly for the Boundary Layer on a Single Rotating Blade.

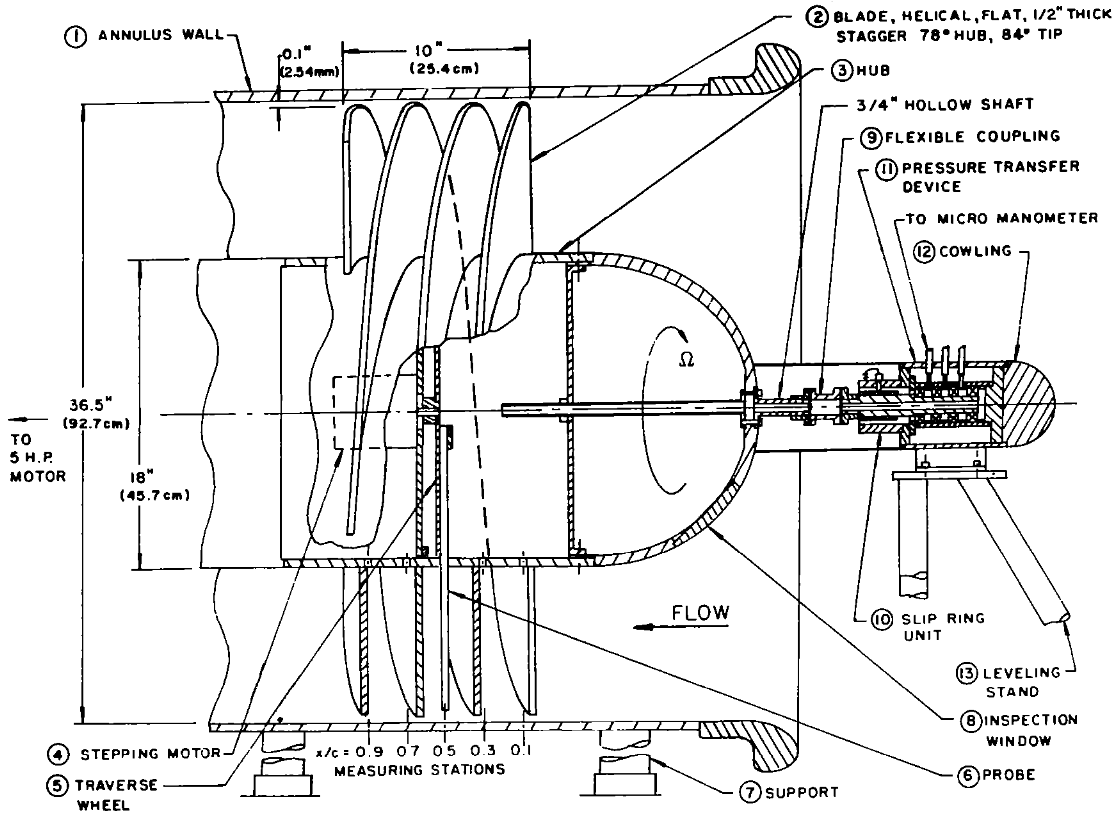

Figure 3a. Flatplate Inducer Facility and Rotating Probe Traverse Mechanism.

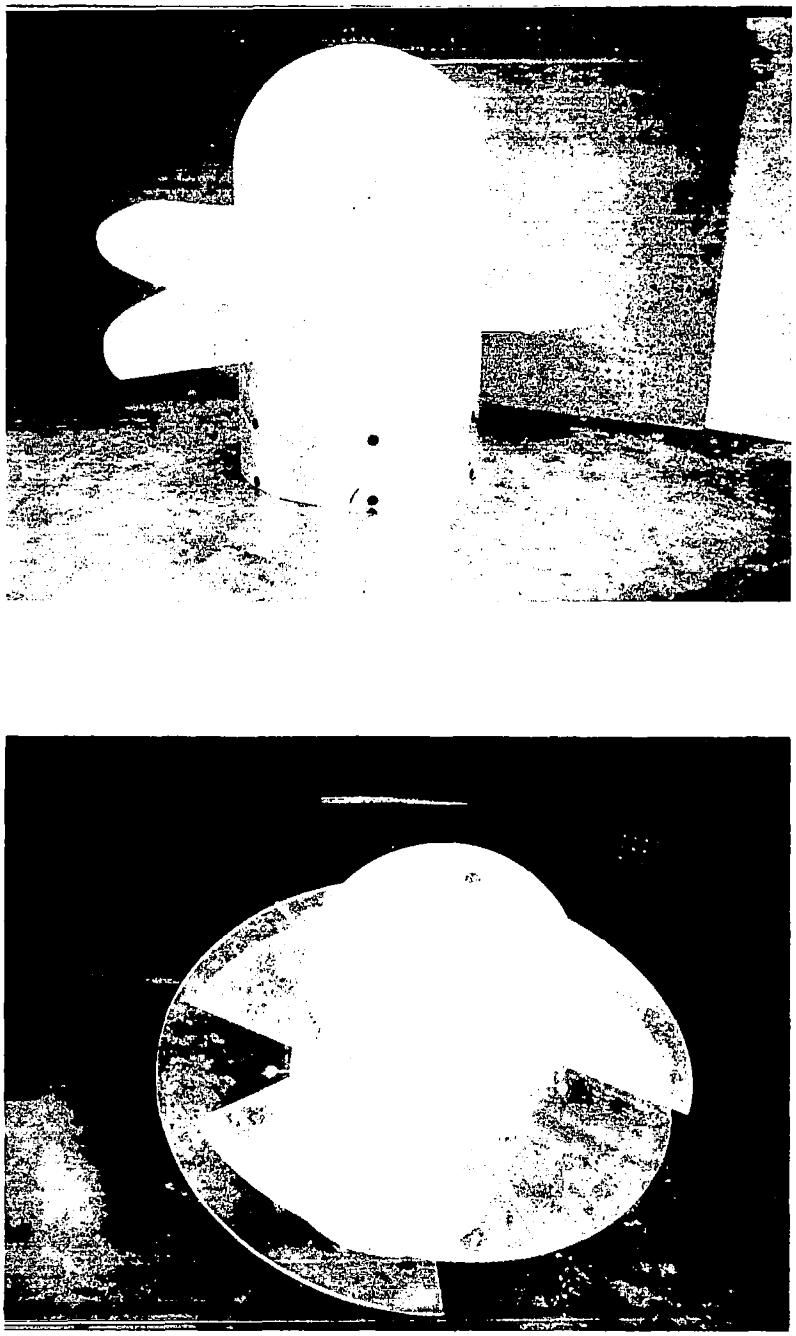

Figure 3b. Photograph of the Flatplate Inducer.

The mass flow through these facilities or the flow coefficient was varied by means of a throttle at the exit. A summary of the various inducer configurations employed, their operating conditions, type of measurement, and analyses carried out is given in Table 1. References where details of the results are published are also listed in this table.

Blade Static Pressure and Limiting Streamline Angle

An extensive experimental investigation of the blade static-pressure distribution was undertaken to help provide a check on the theoretical analyses and the information useful in understanding the nature of flow and the blade boundary layer.

A schematic diagram of the blade static-pressure test setup is shown in Figure 7 of reference [18]. The scanivalve, a scanning type pressure-sampling valve for measuring multiple pressures, was mounted in the rotating hub section of the inducer. It incorporated a fluid wafer switch for time-sharing one pressure lead with up to 24 unknown pressures and was stepped by a rachet-geared solenoid. A three-channel pressure transfer device (shown in Figure 3a) constructed by the Penn State Aerospace Engineering Department, was used to transfer the static-pressure measurements from the rotating reference frame of the three-bladed inducer as well as the flat plate inducer to the stationary reference frame. Each channel was made airtight by the use of double-sealed ball bearings, and pressure leakage was prevented by the use of O-rings and plastic sealers. The pressure-transfer device was mounted on a stand outside the rotor assembly and was housed in a streamlined cowling to reduce any interference on the incoming flow, as shown in Figure 3a.

Flow Visualization

The flow was visualized by means of very thin nylon tufts, smoke, ammonia streak, and lampblack techniques.

Smoke, generated by kerosene, was used for making the flow visible. This method is suitable for the study of both the absolute flow and the relative flow. For flow visualization of the relative flow near the blade surfaces, the smoke produced by a solution of titanium tetrachloride and carbon tetrachloride was found to be superior to kerosene smoke. Titanium tetrachloride is a liquid which, in the presence of moist air, produces dense white smoke fumes consisting of titanium oxide and hydrochloric acid.

The limiting streamline angle (ε_ω), which is the limiting position of the streamline as the blade surface is approached, was derived from the ammonia streak filament method. This consisted of injecting ammonia gas at very low velocities through the static-pressure holes on the surface of the blade. A sheet of ozalid paper sensitive to ammonia was pasted along the edges of the static pressure hole, and thus the traces of ammonia are recorded on ozalid paper while the blade was in motion. The amount of deflection of the streamline from the tangential direction is a measure of the limiting streamline angle. Typical traces of limiting streamlines and the method of injecting ammonia from a stationary source to a rotating blade is given in reference [8]. An ammonia transfer device was used to transfer ammonia gas from the stationary system to the rotating system.

To evaluate the qualitative nature of back-flows and radial flows at inlet and exit (in absolute flow), very thin nylon tufts mounted on a perfectly flexible universal hinge was used.

Pressure Probes for Exit and Passage Measurements

Conventional as well as specialized probes were employed in the measurement of the flow field at the exit and inside the passages of all the inducers, including the flat-plate inducer. The locations of flow-measuring stations are shown in Figure 4 for the aerodynamically designed inducer.

The exit flows were measured at stations 3, 4, 5, 6, and 7 using a stagnation-pressure probe and a tuft probe. Hot-wire measurements were taken very close to the trailing edge (station 3A) to derive the passage averaged values of the radial, axial, and tangential velocity components. The outlet air angles (of the absolute flow) were measured by means of a very thin tuft probe and a sighting scope. Fluctuations in absolute air angles were found to be considerable, especially near the hub locations. The algebraic mean of the maximum and minimum air angles, measured by the tuft probe, was used for calculating the axial and tangential velocity components. In spite of slight inaccuracies which are discussed by McCafferty [6], much information can be gained from these stationary-probe measurements. Since the flow at the exit was highly three-dimensional, the static pressures were measured at the hub and annulus walls and the radial distribution of the static-pressure coefficient was derived by computing the pressure gradient near the wall locations from the simplified radial equilibrium equation.

The measuring stations inside the inducer passage are shown in Figure 4. The stagnation pressure and static pressure of the relative flow were measured at several circumferential and radial locations at station 1, which was about 1/3 chord from the leading edge, and at station 2, which was near the trailing edge.

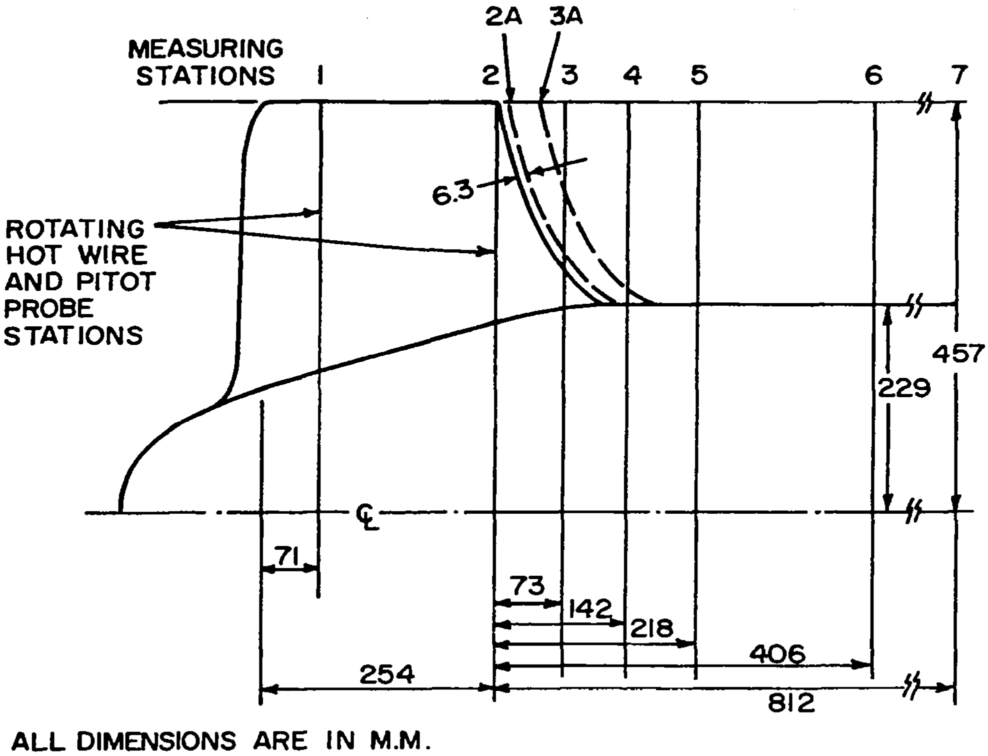

Figure 4. Location of Flow Measuring Stations for Axial Flow Inducers.

The blade static pressures were obtained by means of ports of 0.04 in. dia. drilled in hypodermic tubes embedded on the blade surface. The blade-to-blade static-pressure distributions were derived from a four-hole precalibrated probe. The static pressures so derived were found to vary almost linearly from pressure to suction surface. Hence, a linear variation in ψ_s was assumed between the measured suction and pressure blade static pressures in deriving the relative velocity profiles.

The stagnation pressure of the relative flow was measured by aligning a total-pressure probe parallel to the blade surface. The total-pressure probe was of Gracey's [27] design, giving a sensitivity range of ±18 deg. Since the relative flow deviation from the blade angles and in the radial direction was within this range, the relative stagnation pressures were measured to within 1 percent accuracy. The pressures were transferred to a stationary precision manometer through a pressure transfer device (PTD) described earlier.

Stationary and Rotating Hot-Wire Techniques

Two techniques were developed for the measurement of three-dimensional flow in inducers (see references [17], [19], [20], and [28]). The three components of velocity and turbulence at the exit were measured by means of a three-sensor stationary hot-wire. The hot-wire was traversed at station 2a, which was about 6.3 mm from the inducer trailing edge, as shown in Figure 4. The exit flow was three-dimensional and turbulent in nature, with periodic unsteady components (due to blade-to-blade periodicity) embedded in random motion, when viewed from the frame of reference of the stationary hot wire. The three instantaneous voltage signals picked up from these hot wires were stored on a magnetic tape, digitized in an analog-digital converter, and finally processed in a digital computer to derive the mean (time) velocities and turbulence intensities at various locations of the blade passage. The data were sampled at M number of points within the blade passages in N number of consecutive signals of periodicity $2\pi/\Omega$. M = 50 and N = 80 were chosen in this program. Thus, there were 50 data points in each passage. Methods of deriving the mean velocities as well as turbulence intensities from the hot-wire signals are described in references [17] and [19]. The hot-wire equations are the same as those employed for the rotating hot-wire technique described below.

Gorton and Lakshminarayana [20] employed a three-sensor hot-wire rotating inside an inducer passage. This technique has subsequently been improved and simplified for three-dimensional boundary layer measurement in a flat-plate inducer [22,23]. A summary of the technique developed at Penn State University is given below. It represents a description of the latest technique, rather than a historical evolution of the method. The sensor was located inside the passage such that the relative mean-velocity vector was inside the cone formed by the sensor. The hot wire was mounted on a rotating traverse mechanism, such as the one shown in Figure 3. Gorton and Lakshminarayana [20] did not have an automated tangential traverse. The hot-wire electrical signal was brought through a mercury-slip ring unit into a stationary anemometer system. A schematic of the instrumentation used for the rotating-probe system is shown in Figure 5. The three electrical signals from the hot-wire were brought into three anemometers. Final output from the instrumentation system consisted of three mean voltages ($\bar{E}_1$, $\bar{E}_2$, $\bar{E}_3$) and RMS values of six fluctuating voltages ($\overline{e_1^2}$, $\overline{e_2^2}$, $\overline{e_3^2}$, $\overline{e_1e_2}$, $\overline{e_2e_3}$, $\overline{e_1e_3}$), where 1, 2, 3 refers to the wire number. A spectrum analyzer was also used to determine the energy spectra of each of the six fluctuating voltages.

The equations relating the mean and fluctuating voltages to the three mean velocities and six stress components in any arbitrary coordinate system are given by Gorton and Lakshminarayana [20], and are valid for non-orthogonal hot-wire system.

In this analysis, the fluctuating and mean velocities are separated and the equations are simplified neglecting the second-order terms. The following equations (in matrix form) for the mean velocities and turbulence stresses relating them to the corresponding voltages were derived.

$$\{Q_{\ell n}\}_{(3,N)} = \{\alpha_{\ell i}\}_{(3,3)} \times \{W_{in}\}_{(3,N)} + \{\beta_{\ell ij}\}_{(3,3)} \times \left\{\frac{W_{in}W_{jn}}{U_{1n}}\right\}_{(3,N)} \qquad (1)$$

and the hot-wire equation for this system is

$$\{E^2_{\ell n}\}_{(3,N)} = \{E^2_{0\ell}\}_{(3,N)} + \{B_\ell(n)\}_{(1,3)} \times \{\sqrt{Q_{\ell n}}\}_{(3,N)} \qquad (2)$$

where subscripts ℓ, n, and i denote the wire, the observation point, and the velocity component, respectively, in the reference coordinate system. W_{1n} is the principal component of mean-flow velocity, which in the present coordinate system is in the streamwise direction. $\alpha_{\ell i}$ and $\beta_{\ell ij}$ are functions of direction cosines of the ℓth wire, which includes the correction factor for deviation from the Cosine Law. E_0 is the output d-c voltage at zero flow velocity. $E_{\ell n}$, $B_\ell(n)$, and $Q_{\ell n}$ are the measured values of voltage, slope of the hot-wire calibration curve, respectively, and the effective mean cooling velocity for the ℓ wire and at nth observation point. W_i is the mean velocity component (e.g., W_r, W_θ, and W_z). The numbers in parentheses outside of a matrix represent its dimensions; e.g., $(Q_{\ell n})_{(3,N)}$ is a matrix with three rows and N columns. N is the total number of observation points in a measuring set. Indices i, j, and ℓ can take values 1, 2, and 3, respectively. For $\ell = 1$, α_{11}, α_{12}, and α_{13} correspond to Gorton and Lakshminarayana's [20] terms a_5, a_6, and a_7, respectively. Similarly, for $\ell = 1$, $\beta_{122} = a_8$, $\beta_{133} = a_9$, and $\beta_{123} = a_{10}$, and all other values of β_{1ij} are zero.

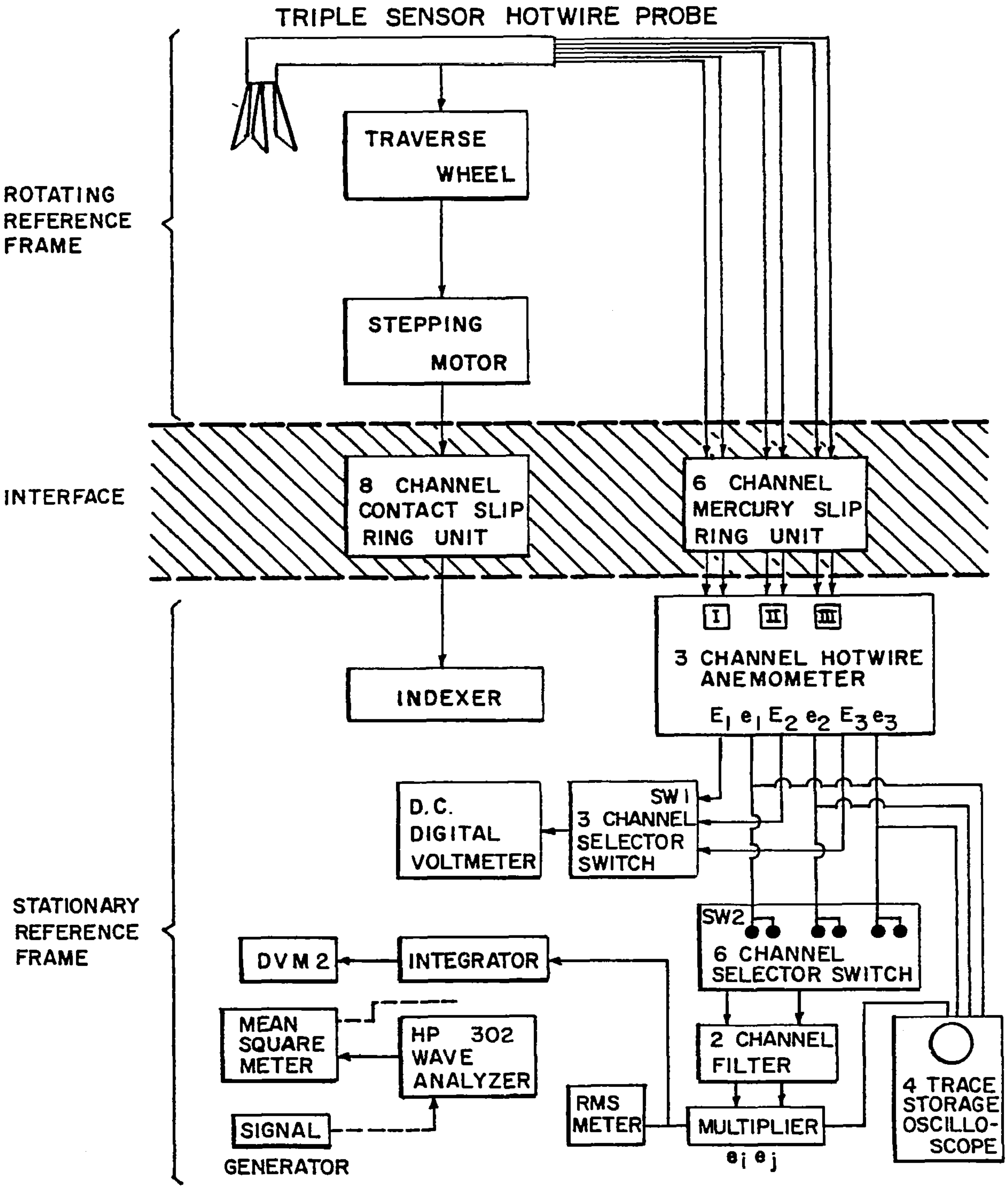

Figure 5. Schematic Diagram of Instrumentation for Rotating Hot Wire Setup.

The six components of Reynolds stress tensor $(\overline{w_i w_j})$ at any point in the rotor passage, in the rotating coordinate system, are obtained from the six measured values of the fluctuating voltage correlations $\overline{e_i e_j}$ and the three mean d-c voltages $\bar{E}_i (i,j = 1 \text{ to } 3)$. The velocity correlations are related to fluctuating cooling velocities as follows.

$$\{\overline{q_{\ell n} q_{mn}}\}_{(6,N)} = \{\gamma_{\ell i}\gamma_{mj}\}_{(6,6)} \times \{\overline{w_{in} w_{jn}}\}_{(6,N)}$$

$$\gamma_{\ell i} = \left(\alpha_{\ell i} + \Gamma_{\ell ij}\frac{W_{jn}}{W_{1n}}\right) \qquad (3)$$

where quantity $(\overline{q_{\ell n} q_{mn}})$ is the correlation between fluctuating cooling velocities of ℓth and mth wires at the nth observation point, and is related to output a-c and d-c voltages as follows:

$$(\overline{q_{\ell n} q_{mn}}) = \frac{16\bar{E}_{\ell n}\bar{E}_{mn}}{B_\ell(n)B_m(n)}\sqrt{Q_{\ell n} Q_{mn}}\;(\overline{e_{\ell n} e_{mn}}) \qquad (4)$$

The coefficients $\alpha_{\ell i}$ and $\beta_{\ell ij}$ are the same as those occurring in equation (1) for mean effective cooling velocity Q. w_i is the fluctuating velocity, and W_{1n} is the mean velocity in the principal direction at the measuring point n. The superscript $(\overline{\quad})$ denotes the time-averaged quantity. The coefficients $(\Gamma_{\ell ij})$, for $\ell = 1$ in Gorton and Lakshminarayana's [20] notation, are

$$\Gamma_{122} = a_{11},\ \Gamma_{133} = a_{12},\ \Gamma_{123} = \Gamma_{132} = a_{13}$$

$$\Gamma_{222} = b_{11},\ \Gamma_{233} = b_{12},\ \Gamma_{223} = \Gamma_{232} = b_{13}$$

$$\Gamma_{322} = c_{11},\ \Gamma_{333} = c_{12},\ \Gamma_{323} = \Gamma_{332} = c_{13}\ .$$

Expressions for a_{11}, a_{12}, a_{13}, etc., are given in reference [20]. All other Γ values are zero. The quantities $\overline{E_{\ell n}}$, $B_{\ell(n)}$, and $Q_{\ell n}$ are, respectively, mean d-c voltage, slope, and mean effective cooling velocity of the ℓth wire at the nth data point, and N is the total number of data points in a measuring set. The matrix equations (1) through (4) are solved successively using the known values of voltages, and calibration data, by using Newton-Raphson convergency scheme.

The velocity components and shear stresses can be derived in any arbitrary coordinate system. A cylindrical coordinate system was used in reference [20] and an intrinsic coordinate system was used in references [22] and [23]. The computer program is reproduced in reference [18]. A modified computer program, which includes all the errors discussed in reference [23], is incorporated in reference [29].

EXPERIMENTAL RESULTS ON INDUCER FLOW FIELD

Flow Visualization in Four-Bladed Inducer Passages

A visualization study of the flow through the four-bladed inducer configuration is reported in references [12] and [30]. The flow near the blade surfaces, inside the rotating passage, downstream and upstream of the inducer, was visualized by means of smoke, tufts, ammonia filament, and lampblack techniques. The flow was found to be highly three-dimensional, with appreciable radial velocity throughout the passage. Some of the major conclusions of this visualization study are:

1. At or near the design flow coefficient, no back-flow is observed upstream of the inducer. A separated region of the flow exists near the hub at the discharge of the inducer. Flow visualization on the hub surface indicates that this back-flow region originates near the blade trailing edge. It has been confirmed [15] that the causes of this flow separation are not due to sudden perturbation of the hub boundary layer between the rotating hub and the stationary hub, but are primarily caused by radial flows in the wake and the secondary flow inside the blade passages.

2. The extent of the back flow increases considerably, both at inlet and at exit, for flow coefficients lower than the design value.

3. The expected radial motions within the blade passage have been confirmed by flow visualization experiments and appear to be quite strong at all the radii. The radial velocity increases continuously from leading to trailing edge of the blade, the angle of the limiting streamline angle being of the order of 60 deg near the suction surface and 30 deg near the pressure surface near the trailing edge. The radial flows are generally higher near the suction surface than on the pressure surface.

4. The radial movement inside the blade boundary layer, when encountered by the annulus wall, tends to deflect towards the mid-passage and then radially inward. These radial flows exist near the outer radius (mid-radius to tip) and are found to be large.

5. The flow transition from laminar to turbulent flow occurs at slightly lower Reynolds number than a flat plate with equivalent mainstream velocity.

6. Flow visualization carried out near the leading edge at various Reynolds numbers, shown in Figure 6, indicates large radial velocities at low Reynolds numbers where the flow is laminar. Formation of tip vortices can also be seen in Figure 6.

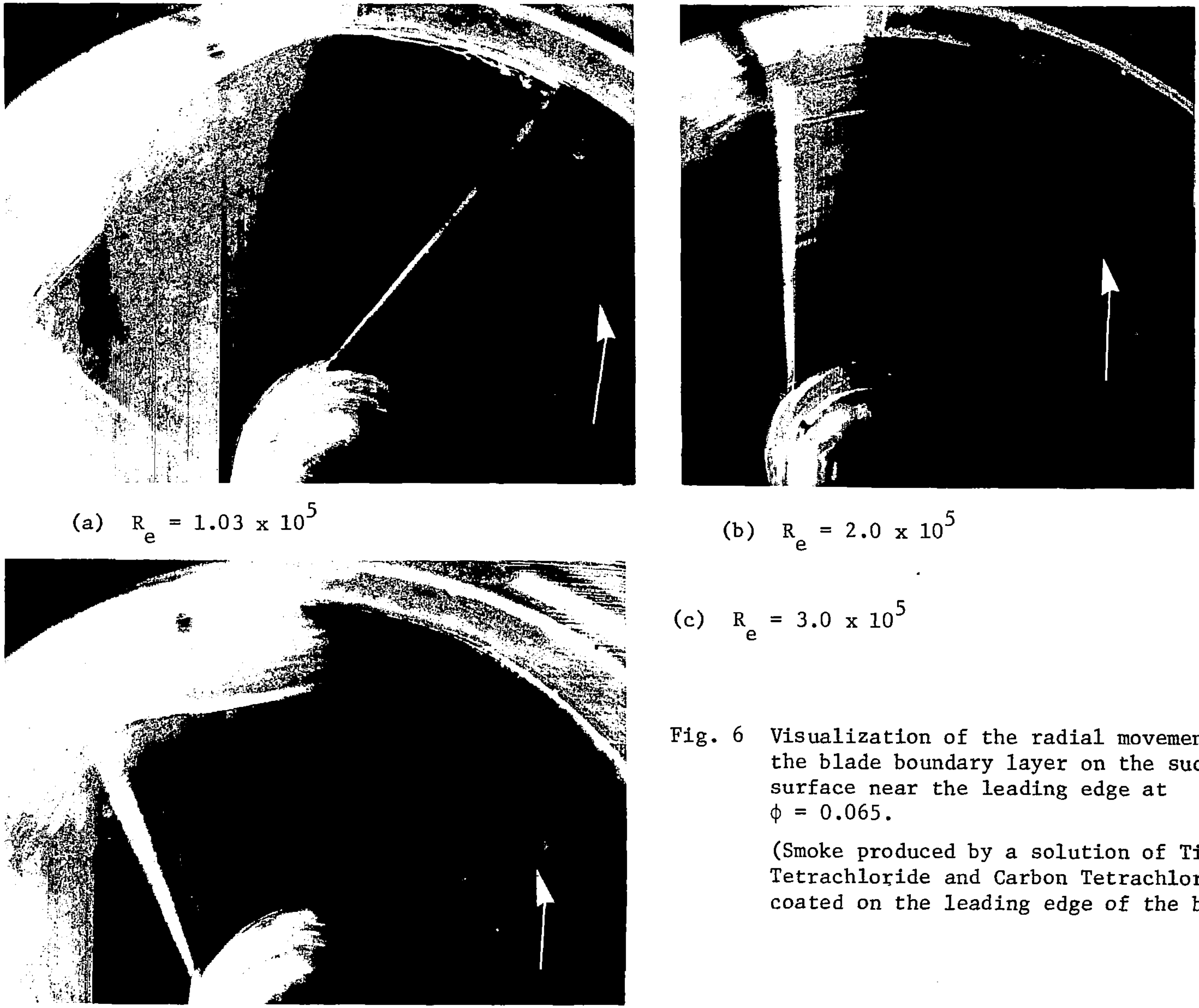

(a) $R_e = 1.03 \times 10^5$

(b) $R_e = 2.0 \times 10^5$

(c) $R_e = 3.0 \times 10^5$

Fig. 6 Visualization of the radial movement of the blade boundary layer on the suction surface near the leading edge at $\phi = 0.065$.

(Smoke produced by a solution of Titanium Tetrachloride and Carbon Tetrachloride coated on the leading edge of the blade.)

7. The secondary vortices, both calculated and observed, are found to be much larger near the hub than at the tip. The predicted secondary vortices are in qualitative agreement with the observations.

8. The investigations suggest that one possible way of preventing the back-flow region near the hub is to use either splitter vanes or hub-wall suction.

Qualitative nature-of-velocity profiles, derived from visualization experiments [12], indicate that the conventional practice of assuming the boundary layer is thin, two-dimensional, and is a small perturbation of the inviscid flow, is not valid in this case. The values of limiting streamline angles are found to be large. Hence, the approach used for predicting the flow through pump inducers should be entirely different from those used for other types of turbomachinery (viz., compressors and turbines). Meaningful prediction of the flow should take into account not only the secondary-flow phenomena, but also the three-dimensional nature of the boundary layer, which has both radial inward and outward flow, as shown in Figure 7.

Measurements Downstream of the Aerodynamically Designed and Flat-Plate Inducers

Four-Bladed Inducer. The flow measurement carried out at several stations downstream of the four-bladed inducer blade row are reported in references [7], [11], [15], and [16].

The radial distribution of stagnation and static pressure, axial and tangential velocity, and flow angles of the absolute flow were measured at several locations downstream (see figure 4 for station designations) using conventional and hot-wire probes. The major conclusions from the four-bladed inducer results are:

1. The test inducer, designed approximately for uniform head distribution over its discharge area, actually produces a very nonuniform head near the tip, as shown in Figure 8. The actual stagnation-pressure (or head) rise of the absolute flow is found to be two to three times that near the hub and mid-radius. This nonuniform head distribution can be qualitatively explained by real fluid effects [15]. The stagnation pressures are found to decrease continuously as the flow proceeds downstream, as can be seen by comparing ψ_t distribution at stations 4 and 6. The wake mixing losses combined with the large change in axial velocity distribution are the major causes of this.

2. The expected radial motions within the blade passages have been quantitatively observed by hot-wire measurements downstream of the inducer. The radial velocities (passage-averaged RMS values) are found to be of the same order of magnitude as axial velocities, its value increasing towards the tip.

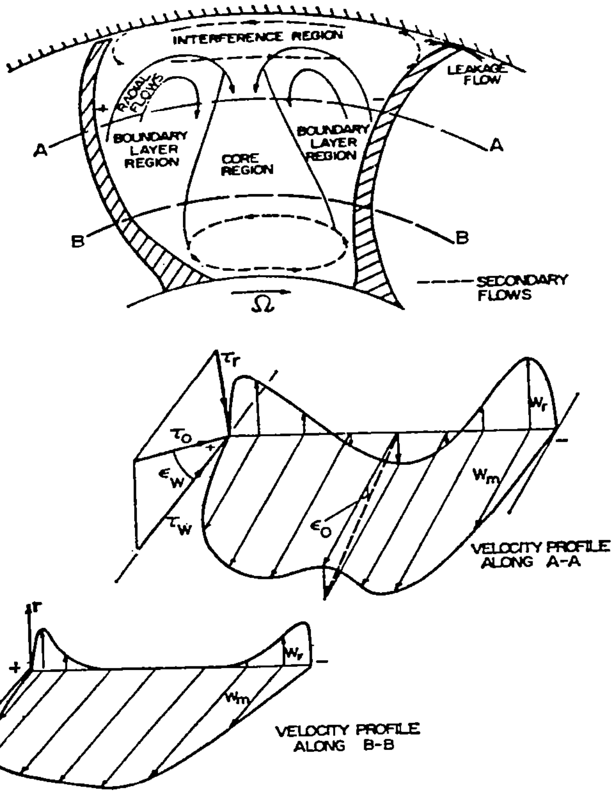

Figure 7. Qualitative Nature of the Velocity Profiles and Secondary Flow Inside the Inducer Passages.

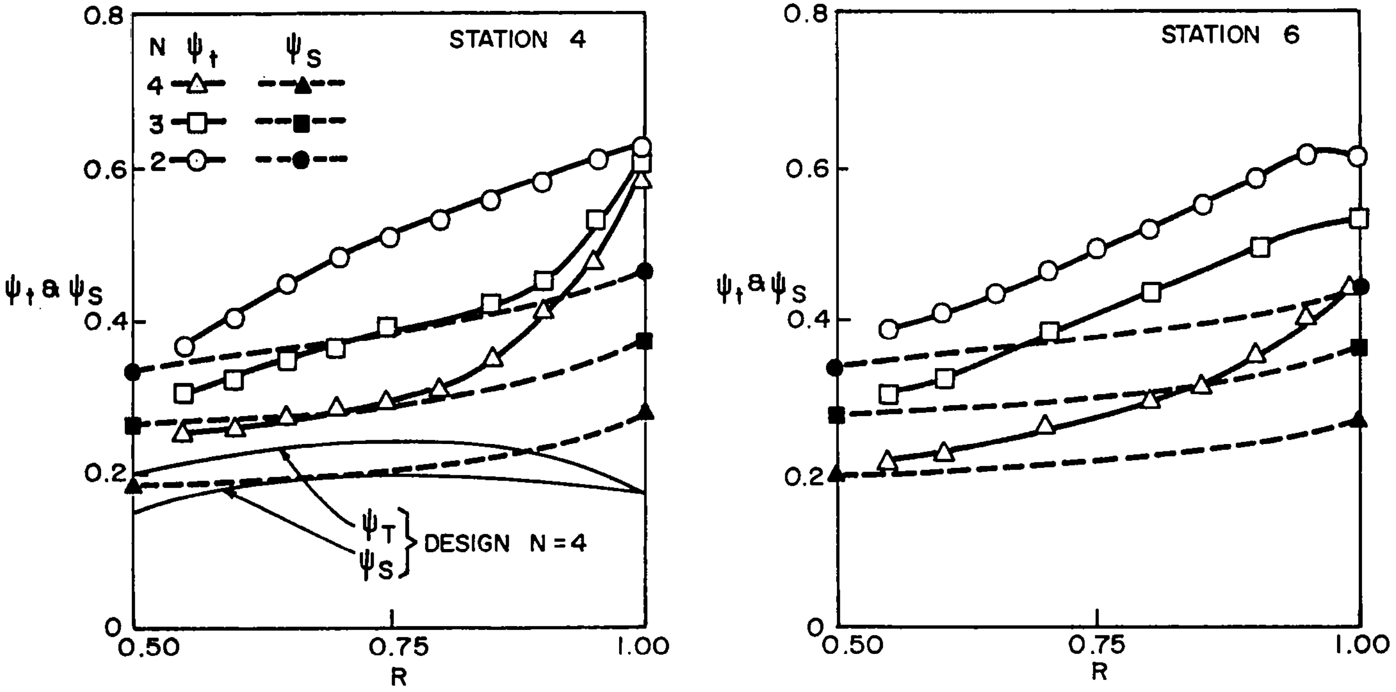

Figure 8. Radial Variation of ψ_t and ψ_s for Four, Three, and Two Bladed Inducers.

3. The axial velocity distribution shows maximum departure from design, as shown in Figure 9. The velocity near the hub shows a tendency to separate, with maximum values occurring near the tip. Measurements very close to the trailing edge (Figure 9, station 3) reveal a different trend, with minimum velocity occurring at mid-radius. The analysis carried out in reference [17] indicates that blade blockage may be partially responsible for this effect. The axial velocity undergoes considerable redistribution as the flow proceeds downstream from station 3 to station 4 (Figure 9). Lampblack traces on the hub surface indicate that the back-flow originates near the trailing edge irrespective of whether the rotating hub is terminated at the trailing edge or continued downstream for one-half chord length [15]. It was anticipated earlier that the flow separation near the hub may have been caused by the sudden perturbation of the hub-wall boundary layer between the rotating and the stationary hub. To check this hypothesis, the measurement of stagnation and static pressure, velocity, and angles was repeated with the rotating hub extending about one-half chord downstream. The measurements revealed no noticeable change in the performance or the location of the separation point [15].

4. The measured tangential velocity (absolute) is substantially higher than the design, especially from the mid-radius to the tip. The real fluid effects combined with large radial flows that exist inside the blade passages are responsible for such large increases in the tangential velocity and the head rise. Furthermore, appreciable change in tangential velocity is observed as the flow proceeds downstream. Changes in mass-averaged momentum are found to be small compared to the local (fixed radii) changes in momentum observed at various downstream stations. This confirms that the changes in tangential velocity downstream of the inducer are mainly brought about by the flow redistribution caused by the radial flows inside the wake (see discussion in reference [15]).

5. The measured static-pressure gradients are found to be large compared to the design values from mid-radius to tip. There is appreciable loss in static pressure near the tip as the flow proceeds downstream (Figure 8).

6. The loss coefficient (ζ) calculated from the measured Euler head coefficient ($\psi_E = 2U\,V_\theta/U_t^2$) and measured pressure coefficient (ψ_t) given by

$$\zeta = \psi_E - \psi_t$$

is plotted in Figure 10. The losses are much higher than for any other conventional turbomachinery, especially in the outer radii. The flow losses near the tip are several magnitudes higher than those at other radii.

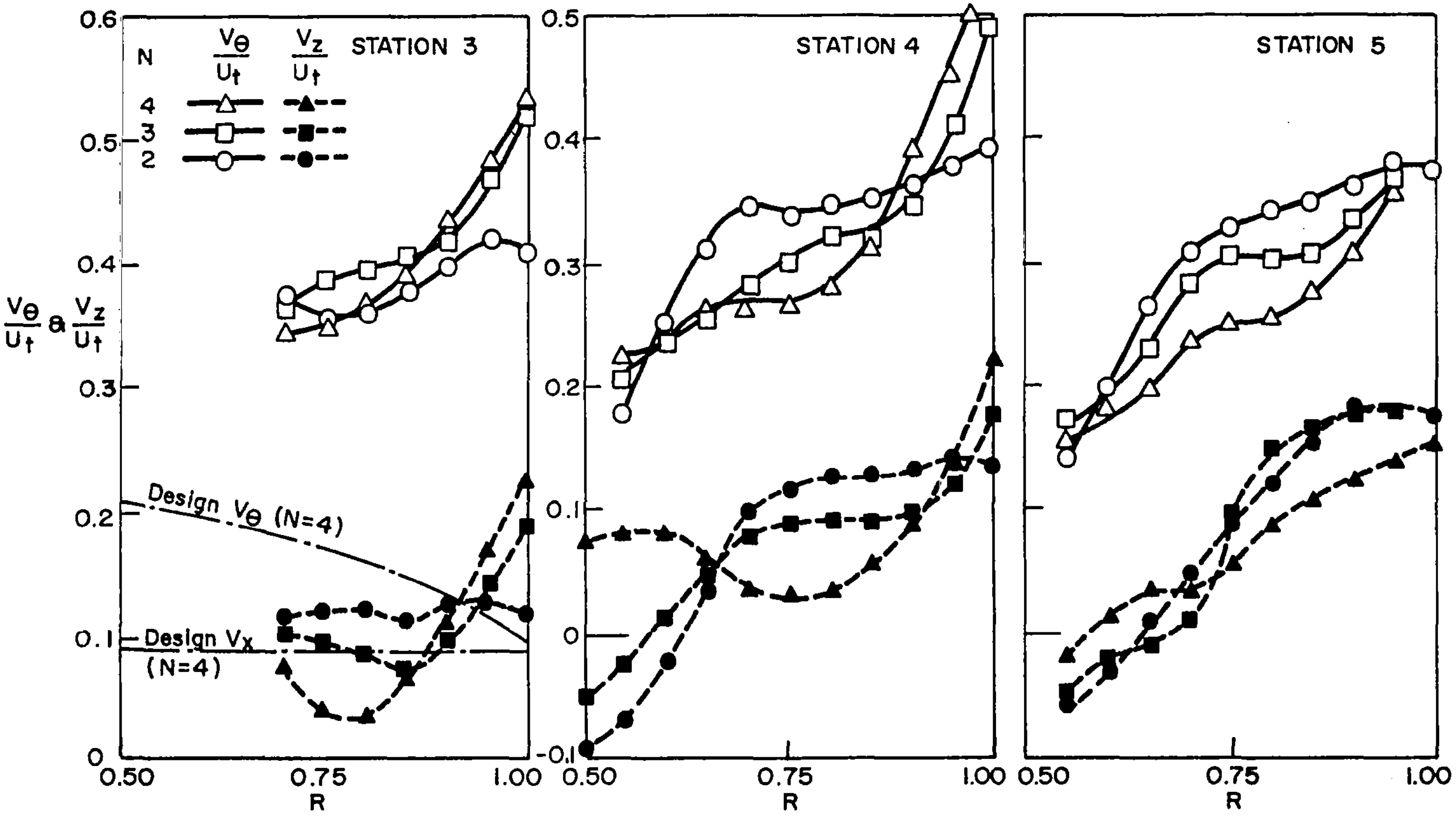

Figure 9. Radial Distribution of Tangential and Axial Velocities for the Four, Three, and Two Bladed Inducers.

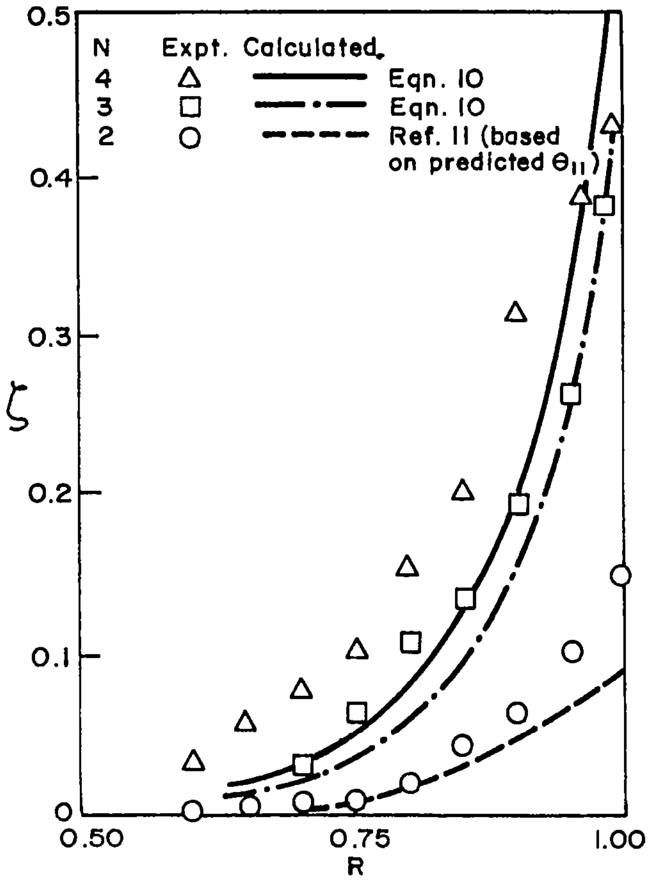

Figure 10. Calculated and Measured Loss Coefficient ζ (Station 4)

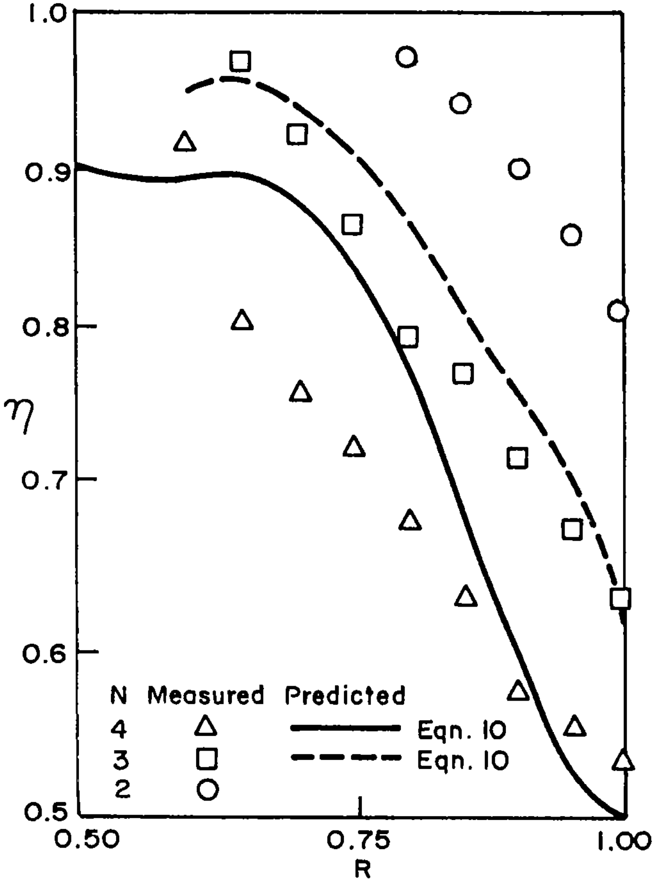

Figure 11. Radial Distribution of Local Efficiency η at Station 4

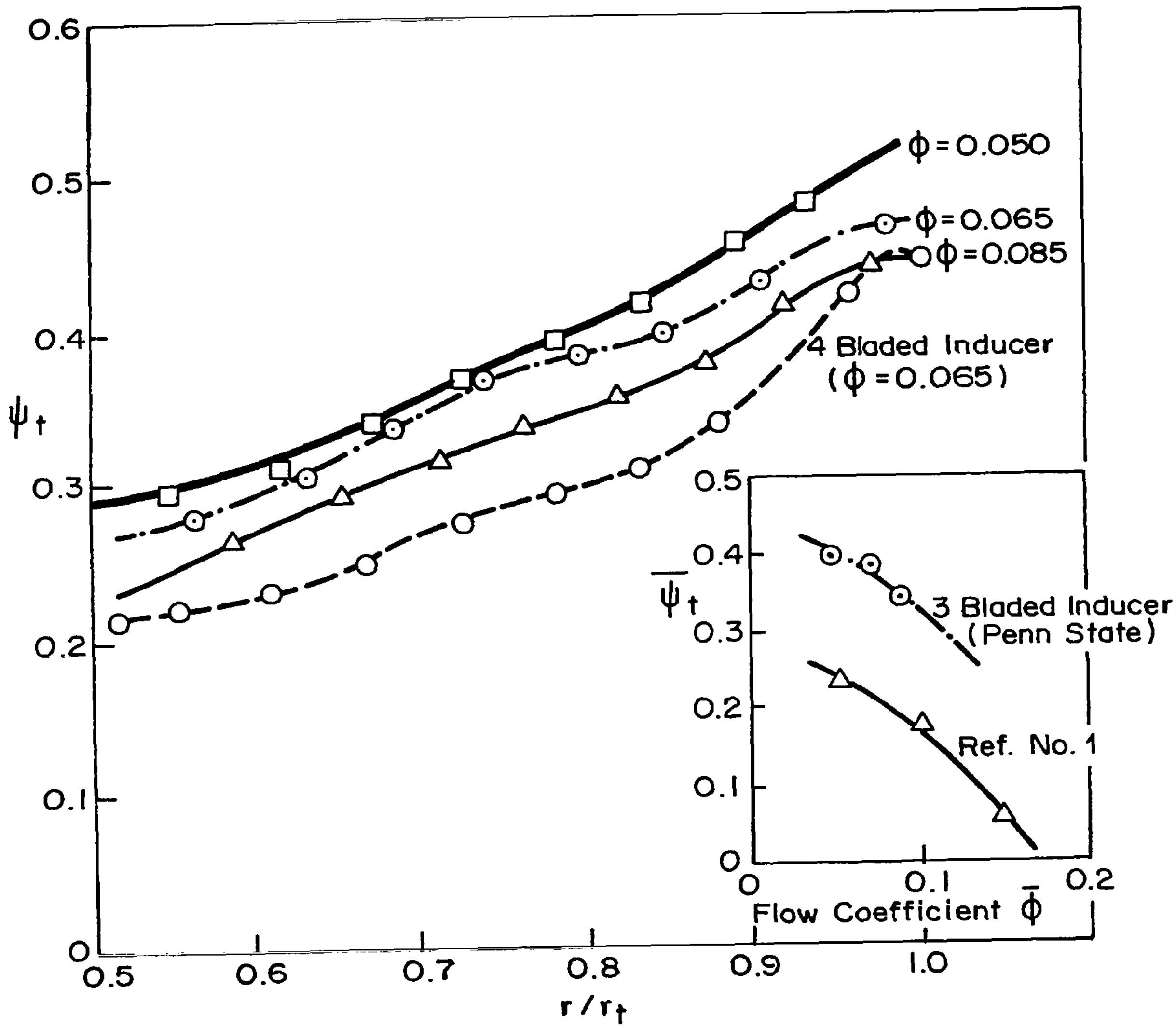

Figure 12. Radial Distribution of Absolute Total Head Coefficient (ψ_t) at Station 6 at Different Flow Coefficients for Three Bladed Inducer

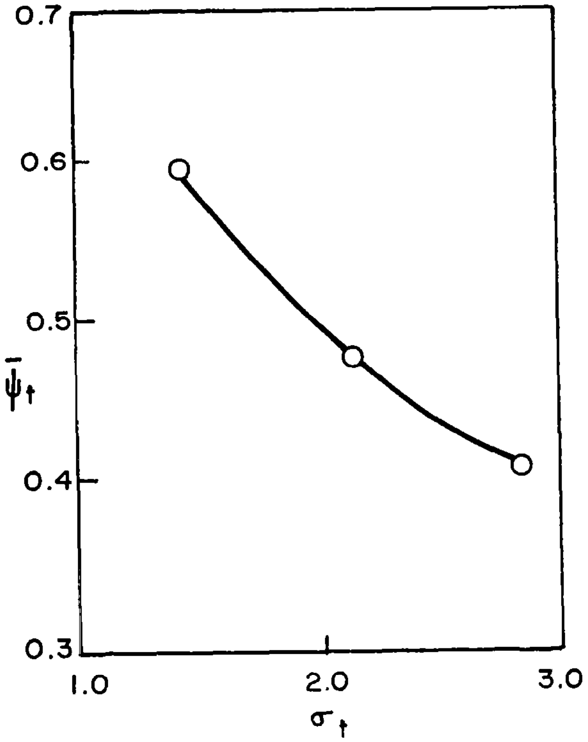

Figure 13. Variation of Mass Averaged Stagnation Pressure Rise ($\bar{\psi}_t$) with Solidity (Station 4).

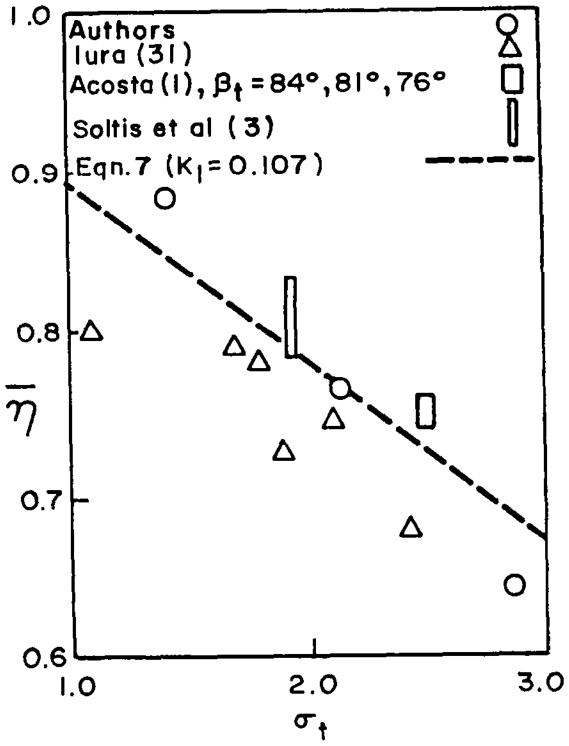

Figure 14. Variation of Mass Averaged Efficiency ($\bar{\eta}$) with Solidity (Station 4).

7. The hydraulic efficiency, $\eta = \psi_t/\psi_E$, plotted in Figure 11, shows near-normal efficiencies (90 percent) near the root and 50 percent efficiency near the tip for the four-bladed inducer. The mass-averaged efficiency given by

$$\bar{\eta} = \int_{r_h}^{r_t} \eta V_z r dr \Big/ \int_{r_h}^{r_t} V_z r dr \qquad (5)$$

is found to be 63 percent for the four-bladed inducer.

Effect of Solidity (or Number of Blades) on Overall Performance. The absolute flow measurements carried out at the exit of the three-bladed and two-bladed inducers are reported in references [9], [11], [16], [17], and [21], respectively. All of the inducers were tested at the same flow coefficient and Reynolds number. Major conclusions derived by comparison of these measurements, shown plotted in Figures 8 through 14, with those of the four-bladed inducer are:

1. The results indicate that the performance, both pressure rise and efficiency, improves continuously with a decrease in solidity (at the same flow coefficient ϕ). The two-bladed inducer shows the best performance, even though the back-flow region near the hub at the exit is increased with a decrease in solidity.

2. The static-pressure (or head) rise increases continuously, at all radii, with the decrease in solidity (Figure 8). The average static head coefficients are found to be 0.21, 0.31, and 0.375, respectively, for four-, three-, and two-bladed inducer.

3. The stagnation-pressure rise coefficient at stations 3 and 4 for four-, three-, and two-bladed inducers is shown in Figure 8. Strong real fluid effects are evident at all solidities. The performance of an inducer has some characteristic features similar to a shear or drag pump, where the shear forces are utilized to exchange kinetic energy between the fluid and solid bodies. Large radial velocities that exist in these inducers (inside the blade boundary layers) provide the shear pumping effect. The measured value of ψ_t near the tip is about two to three times the design value. Furthermore, ψ_t increases continuously with the decrease in solidity. The frictional effects play a dual role here. The energy exchange or head rise is the desirable part. Associated with friction is the energy dissipation of the fluid flowing through the pump. These losses arise from (in addition to secondary and leakage flow near the annulus and hub walls): (a) skin friction near the blade surface, and (b) interaction between pressure surface and suction surface boundary layers, especially near the outer wall. The radial movement inside the blade boundary layer, when encountered by the annulus wall, tends to deflect towards mid-passage and then radially inward.

Intense turbulence and mixing in this region give rise to considerable flow loss. Both of these losses are reduced when the spacing is increased, even though the effect of spacing on energy transfer is not appreciable. The net effect is a larger pressure rise, at all the radii, as the blade spacing is increased. It can also be seen in Figure 8 that a steep rise in ψ_t (towards the tip), observed in the case of three- and four-bladed inducers, is substantially reduced for N = 2, thus indicating minimization of the interaction effects near the tip as the solidity is decreased. Radial variation of the stagnation-pressure rise at various flow coefficients for the three-bladed inducer is shown in Figure 12. Even at $\phi = 0.085$, the three-bladed inducer has a higher pressure rise than the four-bladed inducer operating at the design conditions ($\phi = 0.065$). The insert in Figure 12 is the overall pressure rise versus flow coefficient for the three-bladed inducer as compared with Acosta's inducer [1]. It should be noted that ψ_t for N = 2 remains almost constant downstream of the inducer, while it decreases continuously for N = 4 and 3 as the flow proceeds downstream. Large radial velocity, wake width, and the mixing losses associated with them are the major cause of this change in ψ_t downstream. Ψ_t measured at station 4, at the exit of the two-bladed inducer, is almost twice as much as that of the four-bladed inducer near the mid-radius.

4. Observed increase in ψ_t, with the decrease in solidity, is a result of major significance, indicating that the frictional losses are reduced substantially with the increased spacing, even though energy transfer due to inviscid and shear pumping effects show no appreciable change with the spacing.

5. The mass-averaged stagnation-pressure (or head) rise coefficient, defined by,

$$\overline{\psi_t} = \int_{r_h}^{r_t} \psi_t V_z r dr \Big/ \int_{r_h}^{r_t} V_z r dr \qquad (6)$$

and shown in Figure 13, indicates that ψ_t increases continuously with a decrease in blade number at all the radii. The mass-averaged values for four-, three-, and two-bladed inducers are found to be 0.4, 0.476, and 0.58, respectively. The radial gradient of the head rise coefficient, $\partial\psi_t/\partial r$, is found to be almost constant from hub to tip for the two-bladed inducer, unlike that at other solidities, where a steep rise is observed near the tip.

6. Absolute tangential velocities derived from measurements at stations 3, 4, and 6 (Figure 4) are plotted in Figure 9. Immediately downstream of the trailing edge, four- and three-bladed inducers have a similar distribution with a steep rise in $\partial V_\theta/\partial r$ towards the tip, whereas the distribution for two-bladed inducers is rather gradual. Even though the two-bladed inducer has the lowest V_θ at this station,

the stagnation pressure rise is higher than those at other solidities (Figure 9), thus confirming the earlier conclusion that higher-solidity inducers have larger flow losses. There is considerable change in V_θ for N = 4 and 3 as the flow proceeds downstream, while V_θ for N = 2 remains nearly constant. These changes are largely due to the mass-flow redistribution and flow losses (reference [15]). Far downstream (Figure 9), the two-bladed inducer has the highest V_θ at all radial locations.

7. The axial-velocity profiles are found to be similar, qualitatively, downstream of all the inducers tested, as shown in Figure 9. The steep rise in axial velocity towards the tip observed in the case of three- and four-bladed inducers is absent in the case of the two-bladed configuration, but the extent of the separated zone (or back-flow region) near the hub increases continuously with the decrease in solidity. Very near the trailing edge (at station 3 in Figure 9), the axial velocity is found to be radially uniform for the two-bladed inducer, unlike three- and four-bladed inducers, where the minimum velocity is found to occur at the mid-radius. This indicates the dominant influence of the blade blockage, which is large for the four-bladed inducer. Furthermore, the hub flow separates much earlier as the solidity is decreased. Thus, the axial-velocity profile deteriorates with the decrease in the solidity.

8. The radial distribution of loss coefficient (ζ) calculated from the measured Euler head coefficient (ψ_E) and the stagnation-pressure coefficient (ψ_t), at station 4, are plotted in Figure 10. The steep gradient in ζ that exists near the tip for N = 4 and 3 is reduced drastically for the two-bladed case. As explained earlier, large flow losses (near the tip) for the high-solidity inducer are due to complex interaction between pressure and suction surface boundary layers and the associated turbulence and mixing losses. As the solidity is decreased, these effects are reduced; hence, the decreased losses. There is a drastic reduction in loss between a three- and two-bladed inducer, thus indicating that the boundary layers in a two-bladed inducer do not cover the entire passage.

9. The hydraulic efficiency for the inducer can be derived from $\eta = \psi_t/\psi_E$, where ψ_E is the ideal or Euler head rise coefficient. The efficiencies calculated from the measurements at station 4 are plotted in Figure 11. This clearly indicates that the efficiency improves, at all the radii, as the solidity is decreased. It is surprising that the local efficiencies improve as much as 30 to 50 percent when the solidity is halved. Even though efficiency is not a major consideration in the selection of inducers for the present-day spacecraft, it would assume added importance when space travel becomes a commercial venture.

10. The mass-averaged efficiency derived from equation (5) are shown plotted in Figure 14 and compared with those of Acosta [1], Iura [31] and Soltis et al. [3]; the latter measurements correspond to non-cavitating conditions. Appreciable decrease in $\bar{\eta}$ is observed with the increase in solidity, the trend being the same for all of the inducers shown. A physical reasoning of the observed trend in the variation of overall efficiency ($\bar{\eta}$) with σ is as follows: consider inducers operating at the same flow and blade parameters, except for the change in blade spacing S. Since the average loss coefficient ($\bar{\zeta}$) is proportional to C/d_h or C/S, the solidity, the overall efficiency is

$$\eta = 1 - \frac{k\sigma}{\bar{\psi}_E}$$

where k is a constant. Since $\bar{\psi}_E$, the average Euler head rise coefficient, is nearly the same for all the inducers tested in this program (see Figure 8), overall efficiency ($\bar{\eta}$) can be expressed as

$$\bar{\eta} = 1 - k_1\sigma \ . \qquad (7)$$

The values of $\bar{\eta}$ derived from equation (7) with $k_1 = 0.107$ agree reasonably well with the measured efficiencies (Figure 14). This adequately explains the decrease in efficiency for increased solidity. This reasoning also provides some confidence in the loss correlation developed in reference [15].

Flat Plate Inducer with Open Throttle. The flat-plate inducer shown in Fgiure 3, was initially tested with an open throttle. The exit flow was measured utilizing the probes described earlier. The axial stations employed for the exit-flow measurement are shown in Figure 15, and for the passage-flow measurement, in Figure 3a. The measurements were taken at stations 1, 2, 3, and 4, shown in Figure 15, downstream of the inducer. These are at distances of 8.4, 76, 228, and 355 mm, respectively, from the trailing edge.

The stagnation-pressure rise coefficient (ψ_t) at various distances downstream of the trailing edge are shown plotted in Figure 16. Measurement station 3 for the flat-plate inducer corresponds, approximately, to measurement station 3A or 3 for the inducer (Figure 4). It is evident that the stagnation-pressure rise for the flat-plate inducer exhibits characteristics which are very similar to an aerodynamically designed inducer. Steep rise in stagnation pressure was observed near the tip even in the case of the flat-plate inducer with an open throttle (no inviscid effects). This provides a convincing argument that the tip of the inducer blade behaves as a shear pump, where the pressure or head rise is brought

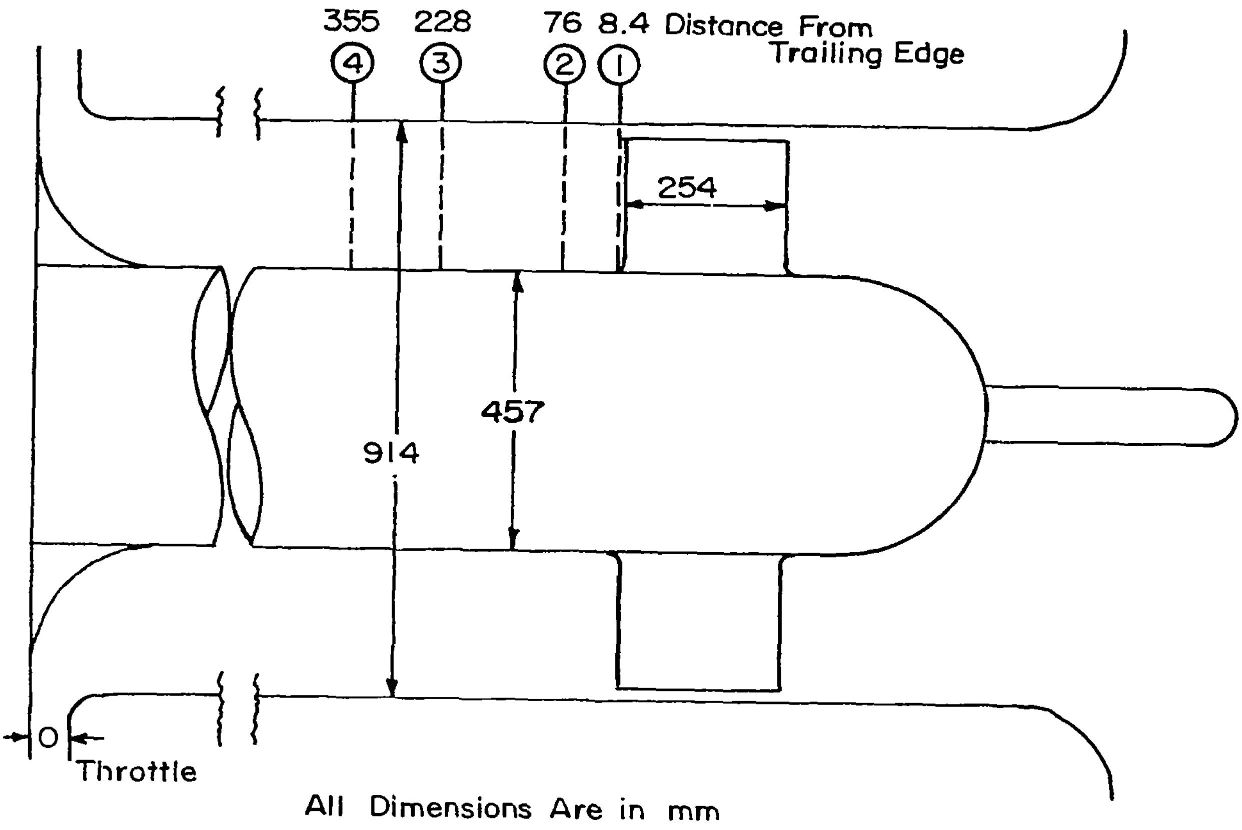

Figure 15. Exit Measurement Stations for the Flat Plate Inducer (Figure 3)

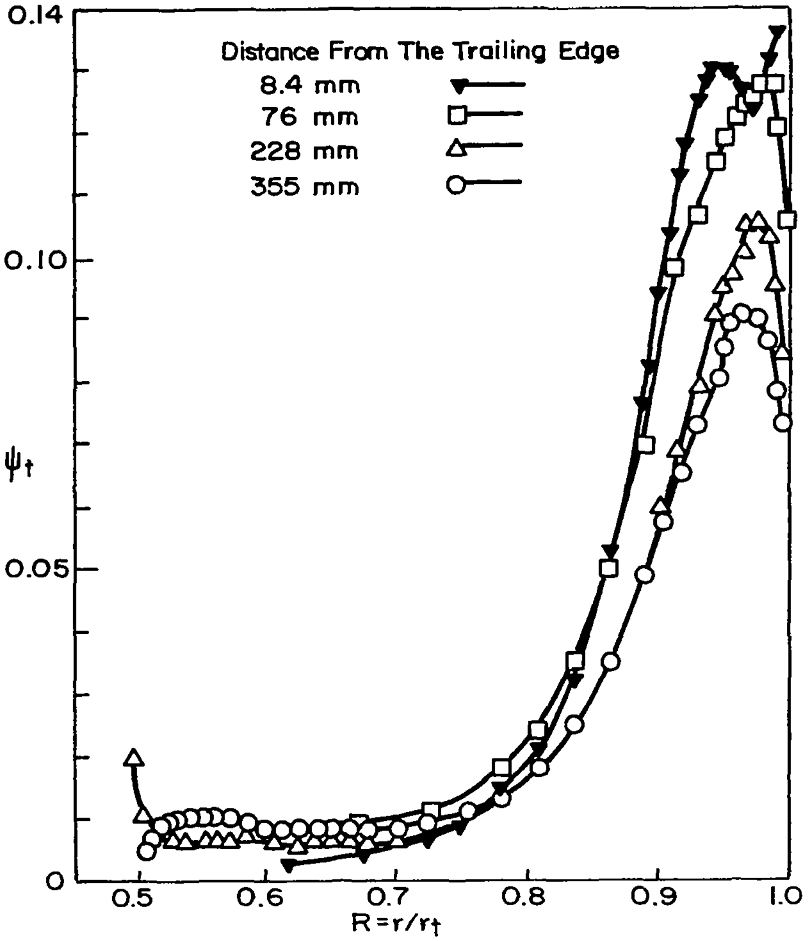

Figure 16. Radial Variation of the Stagnation Pressure Coefficient at Various Axial Locations for the Flat Plate Inducer (Open Throttle)

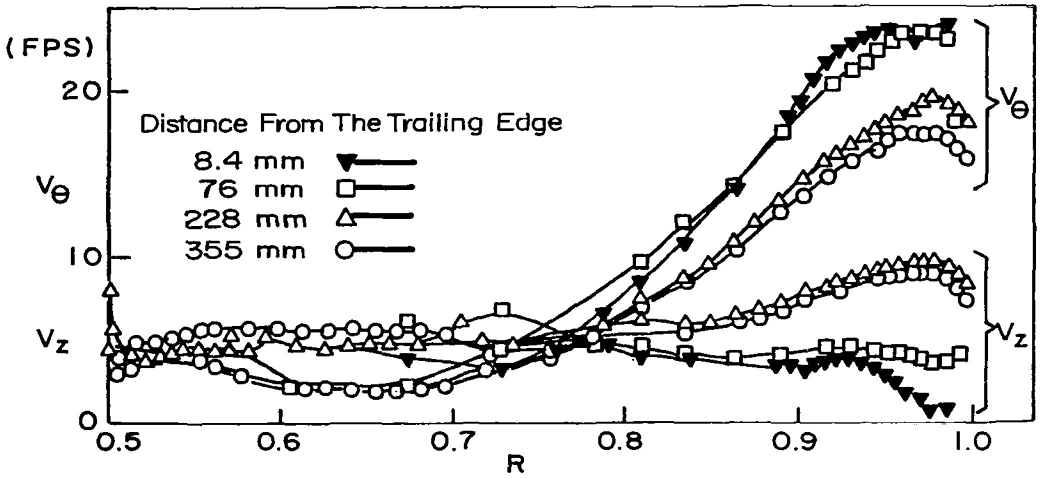

Figure 17. Radial Variation of Absolute Axial and Tangential Velocity at the Exit of the Flat Plate Inducer (Open Throttle)

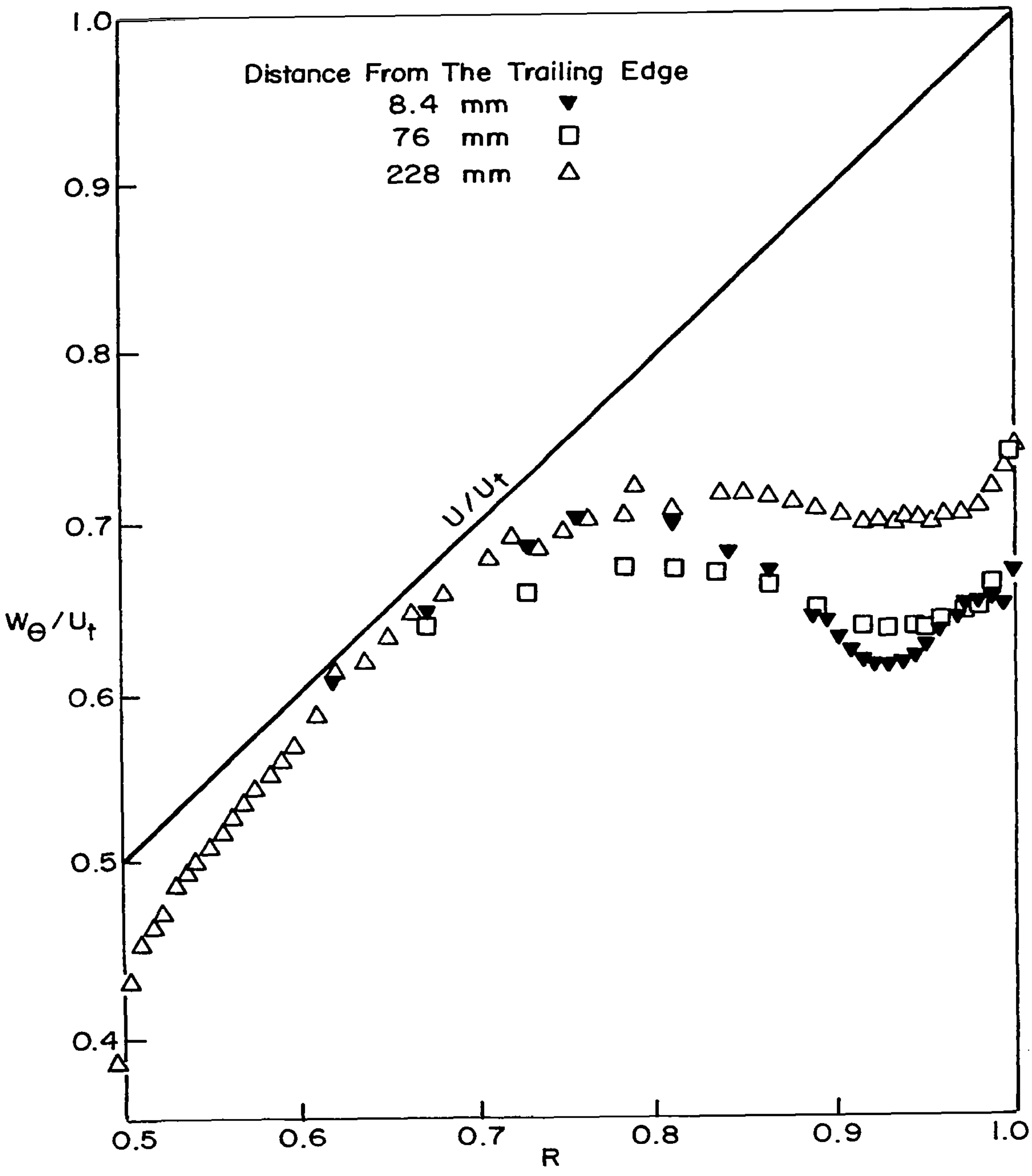

Figure 18. Relative Tangential Velocity Distribution at the Exit of the Flat Plate Inducer (Open Throttle)

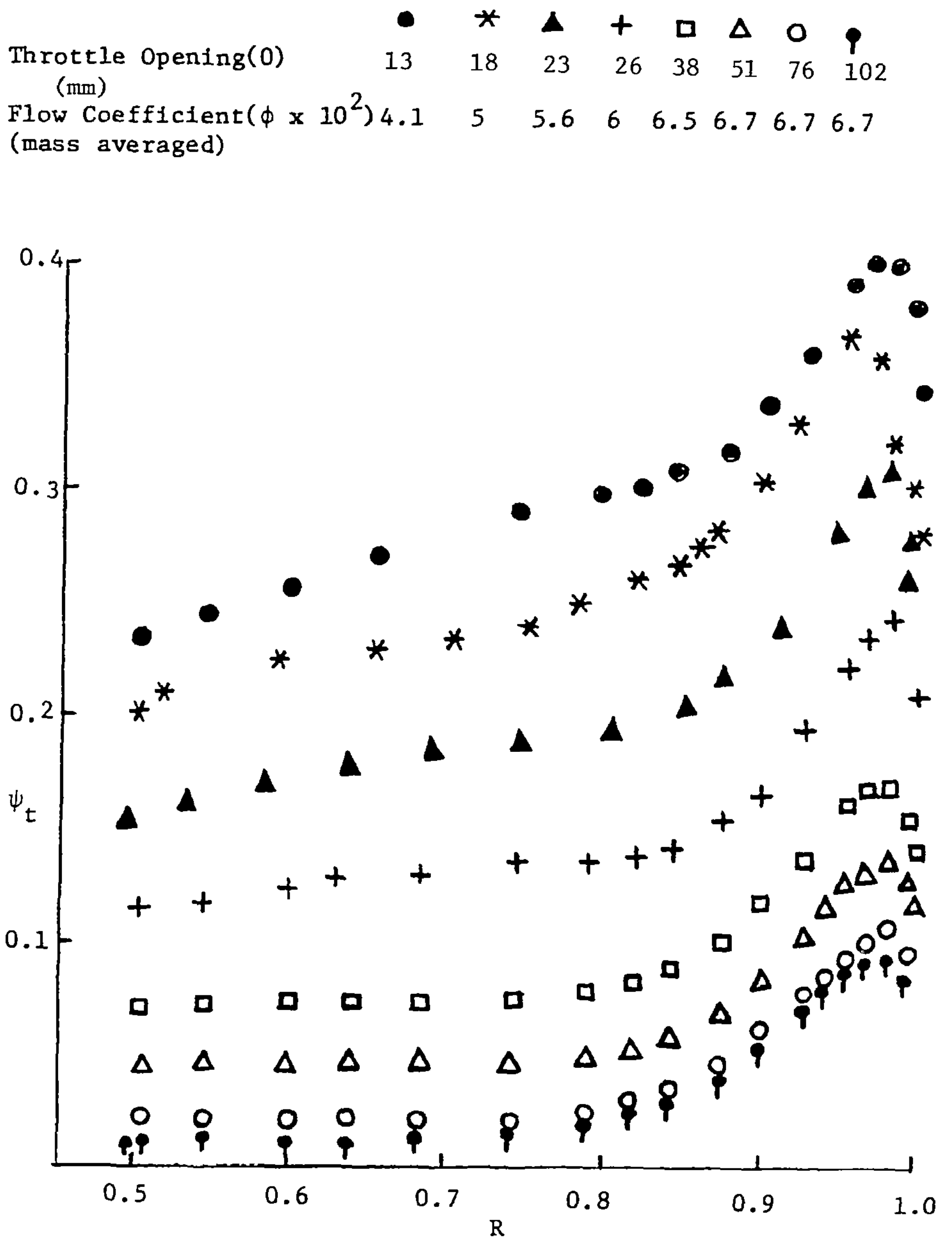

Figure 19. Distribution of Stagnation Pressure Coefficient (ψ_t) at the Inducer Exit.

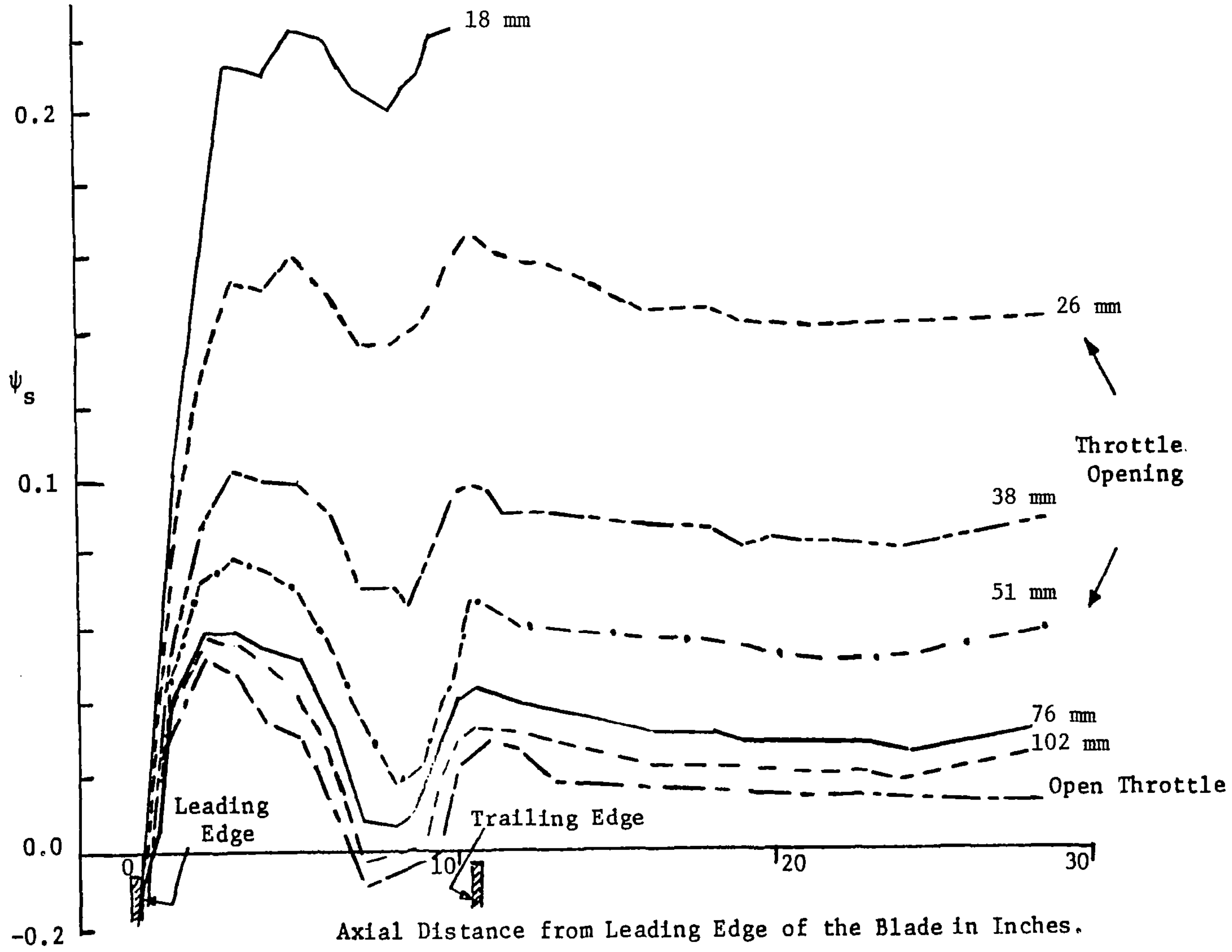

Figure 20. Annulus Wall Static Pressure Distribution.

about entirely by the viscous effects. The stagnation-pressure rise coefficient (ψ_t) near the hub is negligibly small, while its value is nearly 0.15 close to the trailing edge near the blade tip. This value continuously decreases as the flow proceeds downstream, and is caused by losses in the flow.

Radial variation of the axial and tangential (absolute) velocities is shown in Figure 17. The absolute tangential-velocity distribution, even in the absence of inviscid turning effects, is very similar to the distribution observed for the aerodynamically designed inducer. Existence of a steep gradient in the absolute tangential-velocity near the tip is evident from this figure. The tangential velocity decreases appreciably as the flow proceeds downstream. The axial-velocity distribution, shown in Figure 17, reveals a tendency towards separation at the trailing edge. This trend reverses itself further downstream to provide higher axial velocity near the tip of the blade and lower velocity at the root, a trend similar to that observed for the aerodynamically designed inducer (compare Figures 17 and 9).

The passage-averaged relative tangential velocity at the exit of the flat-plate inducer is shown plotted in Figure 18. It is evident that the relative tangential velocity is nearly constant from mid-radius to tip, with a value of nearly 0.7. This trend is very similar to that observed for an aerodynamically designed inducer discussed later in this report.

It is evident from these measurements that the behavior of the flat-plate inducer with an open throttle is similar to those of an inducer, especially near the tip, confirming the conclusion that the viscous effects (as opposed to inviscid effects) play a major role in the pressure rise characteristics of the inducer, especially by the blade element near the outer radius.

Comparison Between Flat-Plate and Aerodynamically Designed Inducer. The flat-plate inducer shown in Fgiure 3 was tested with an open throttle and at various flow coefficients. The stagnation-pressure rise characteristics at various flow coefficients are shown in Figure 19, and the corresponding annulus wall static pressures are presented in Figure 20. The stagnation-pressure rise is appreciable near the tip even for large flow coefficients or throttle openings. This is caused by considerable boundary layer growth on the blades, and the shear pumping effect. It is evident, by comparison between Figures 19 and 8, that the stagnation-pressure rise across a flat-plate inducer is much smaller than that across an inducer with cambered blades operating at the same flow coefficient.

Figure 20 shows the static pressure distribution measured on the annulus wall with differing values of throttle clearance. The negative pressure at the leading edge of the blade, shown in Figure 20, is considered to be caused by the blade blockage effect. Increase of the blade static pressure at the trailing edge is considered to be caused by the increase of flow area due to the absence of the blade thickness. It is seen that the static pressure is constant downstream.

A comparison of annulus wall static-pressure distribution for aerodynamically designed inducers as well as the flat-plate inducer at two flow coefficients is shown in Figure 21. It is evident that most of the static-pressure rise across the flat-plate inducer occurs in the first 1/3 chord length, while for the inducer with cambered blades, designed for trailing-edge loading, most of the pressure rise occurs during the latter half of the chord length. The static-pressure rise across the inducer with cambered blades is much higher.

For the purpose of comparison, the flat-plate inducer data at $\phi = 0.05$ and the data from the aerodynamically designed inducer ($\phi = 0.065$) are chosen. This choice is based on nearly identical pressure rise across the inducers from hub to tip, shown in Figure 22a. The static-pressure and stagnation-pressure rise coefficients, plotted in Figure 22a, indicate nearly similar characteristics, even though the stagnation-pressure rise near the tip is about 50 percent lower for the flat-plate inducer near the trailing edge. From mid-radius to the tip, the aerodynamically designed inducer shows a much steeper gradient in the head rise coefficient. One probable cause is the fact that the stagger angle of the flat-plate inducer near the tip is slightly lower (1 to 2 deg) than that of the aerodynamically designed inducer. The major cause of this, however, is probably due to the "shear pumping effect." At this operating condition, the measured limiting streamline angle near the trailing edge varies from 50 deg at the hub to 15 deg at the tip for the aerodynamically designed inducer, and from 35 deg to 15 deg, respectively, for the flat-plate inducer [23]. Increased values of ε near the hub of the aerodynamically designed inducer may be due to large camber angle (30 deg) and the resulting pressure gradients arising therefrom.

The static-pressure coefficient, presented in Figure 22a, shows a trend similar to the stagnation pressure near the tip. The flat-plate inducer has slightly higher static pressure near the hub in the trailing-edge region. This is attributed to the large blockage effects that exist for the aerodynamically designed inducer.

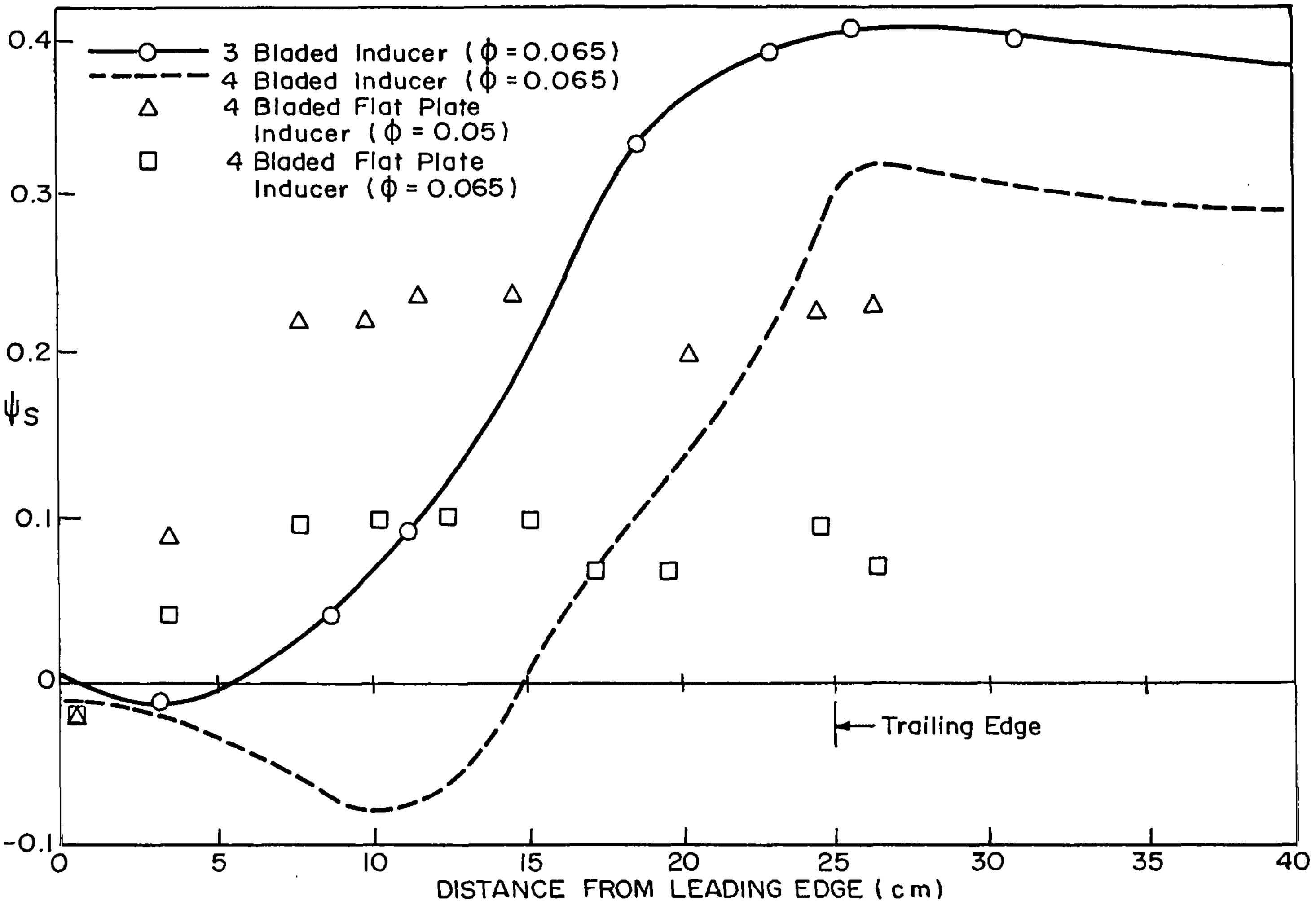

Figure 21. Annulus Wall Static Pressure Distribution for Inducers

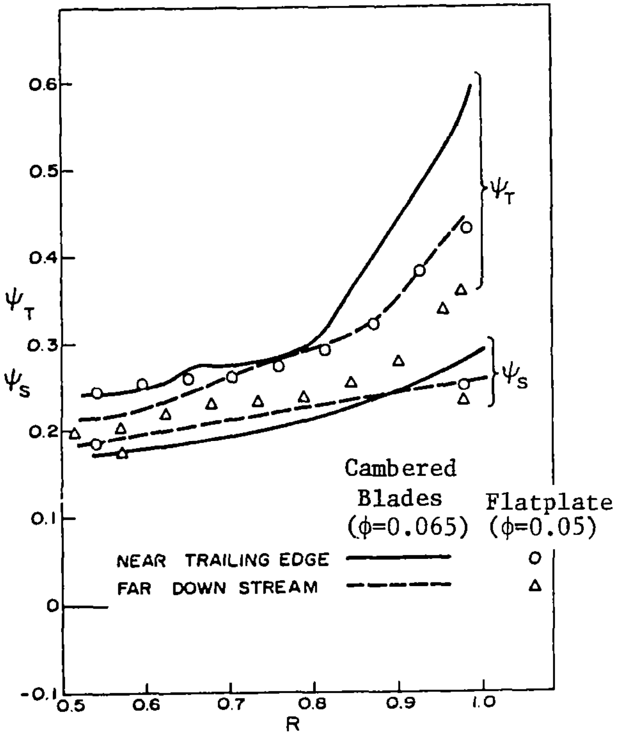

Figure 22a. Comparison of Radial Distribution of Stagnation Pressure Coefficient (ψ_t) and Static Pressure Coefficient (ψ_s) for Flatplate and Cambered Bladed Inducers.

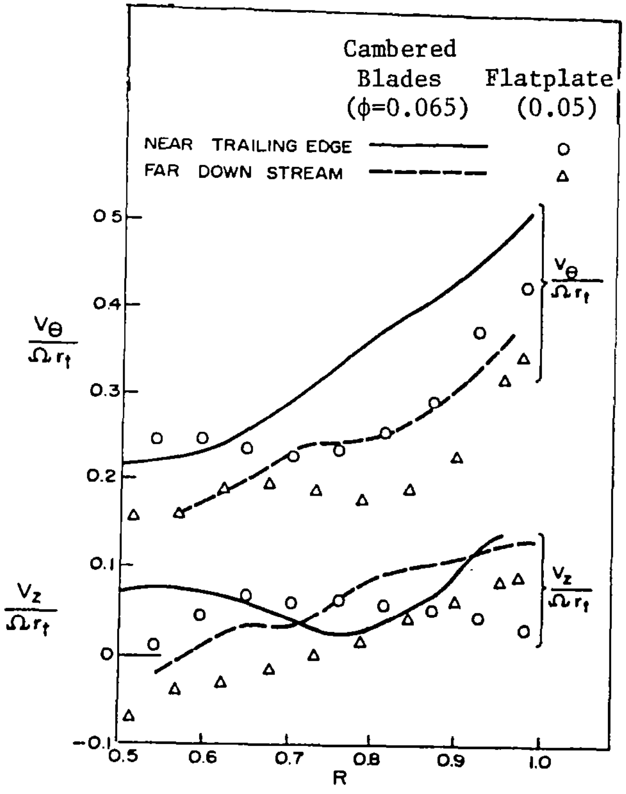

Figure 22b. Comparison of Radial Distribution of the Axial and Tangential Velocity Profiles for Flatplate Inducer and Cambered Bladed Inducer.

The radial distribution of the absolute tangential velocity and the axial velocity are compared in Figure 22b. The tangential velocity follows the same trend as the stagnation-head rise coefficient (Figure 22a), but the major discrepancy occurs in the axial velocity distribution. Near the trailing edge location, the flow in the flat plate inducer shows a tendency to separate near the hub, while the flow in the aerodynamically designed inducer does not. The axial velocity near the tip for the aerodynamically designed inducer is higher, a consequence of higher racial velocity as explained earlier. Both inducers show the same trend at far downstream, with a larger back-flow region observed for the flat-plate inducer. Since the flow near the trailing edge is of major interest, due to the fact that the inducer immediately precedes the main pump, there seems to be some advantage (at least aerodynamically) to design the profiles in the root section with suitable camber and thickness.

Blade-to-Blade Distribution of Flow Properties at the Exit of the Four-Bladed Inducer

Pitot probes, wedge probes, and hot-wire probes were utilized at the exit of the four-bladed inducer to derive flow properties at the exit. A pre-calibrated wedge probe and a stagnation-pressure probe were rotated with the rotor and traversed at station 4 (Figure 4). A disk attached to the hub of the inducer at the exit, described in reference [6], enabled blade-to-blade pressure, angle, and velocity measurements. Details of these measurements and error estimates are given in reference [6]. The results at three radii, R = 0.975, R = 0.77, and R = 0.55, are plotted in Figures 23, 24, and 25, respectively.

Static and Stagnation Pressures. It is clear from the static-pressure distribution shown in Figures 23a, 24a, and 25a that the static pressures are fairly uniform in circumferential direction near the trailing edge and that values agree fairly well with the wall static pressure at station 4, plotted in Figure 8.

The relative stagnation-pressure coefficient (ψ_R) is nearly uniform across the passage near the hub and mid-radius (Figures 24a and 25a). Relative stagnation-pressure deficiencies near the blade surfaces appear to be very small. The measurements near the tip (Figure 23a) indicate considerable boundary layer thickening. This confirms the presence of severe radial flows and, hence, the blade boundary layer transport towards the tip.

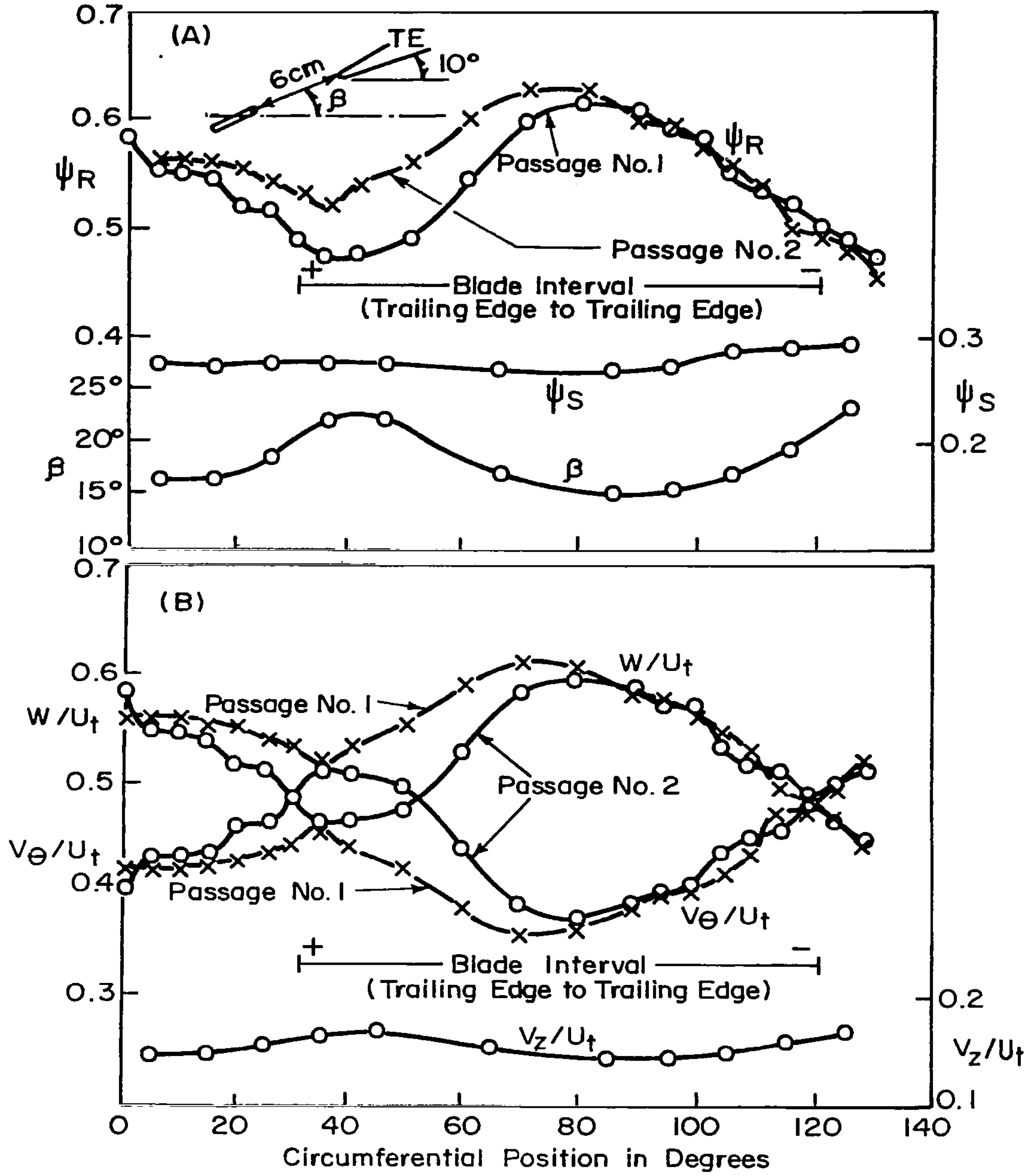

Figure 23. Distribution of Stagnation Head (ψ_R), Static Head (ψ_S), Air Outlet Angle (β), Relative Velocity (W), Absolute Tangential Velocity (V_θ), and Axial Velocity of the Flow Across the Passage at 8 1/2 in. From the Hub ($r/r_t = 0.975$) for the Four Bladed Inducer (Station 4)

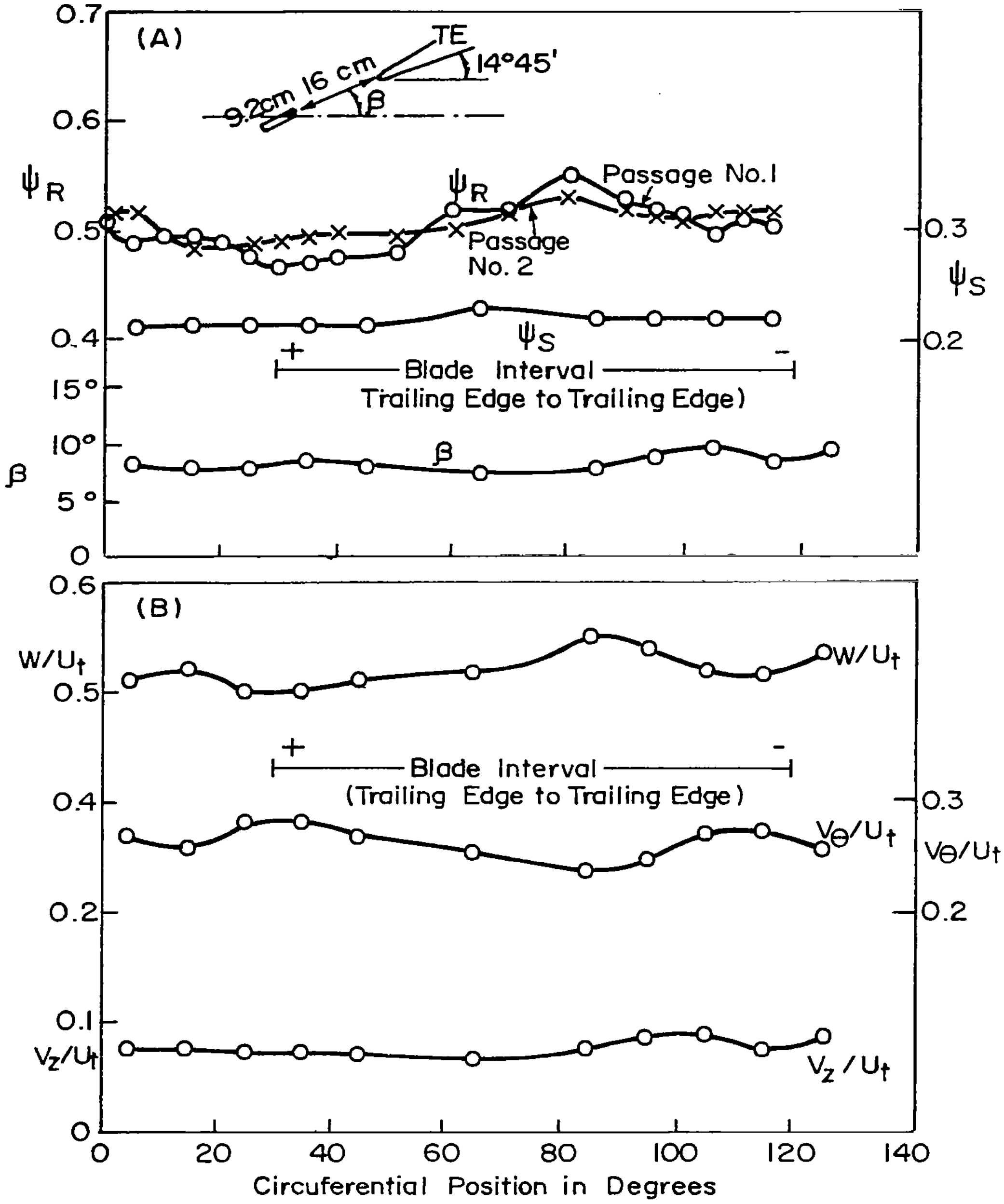

Figure 24. Distribution of Stagnation Head (ψ_R), Static Head (ψ_S), Air Outlet Angle (β), Absolute Tangential Velocity (V_θ), Axial Velocity (V_z), and Total Relative Velocity of the Flow Across the Passage at 5 in. From the hub at (r/r_t = 0.777).

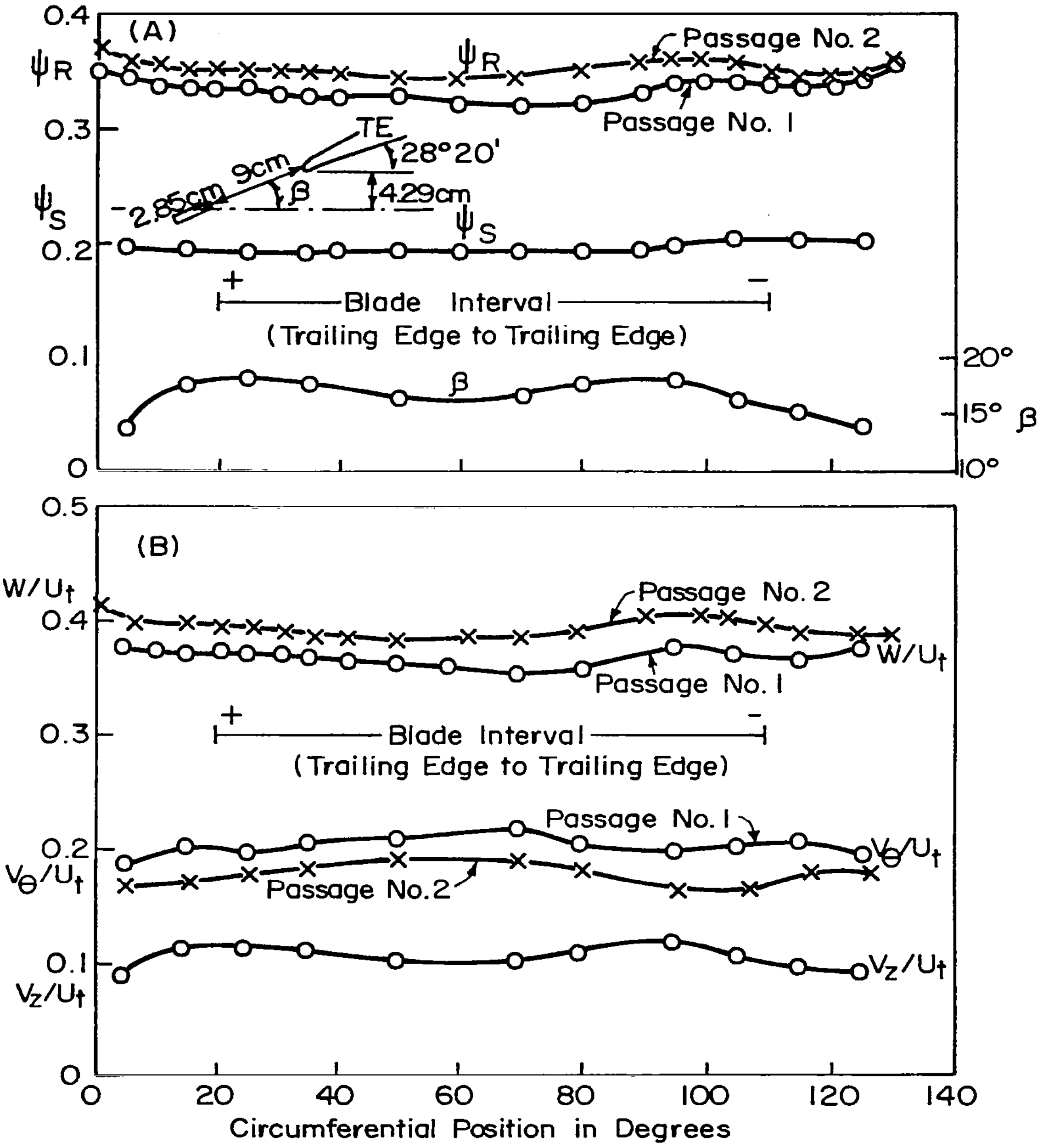

Figure 25. Distribution of Stagnation (ψ_R), Static Head (ψ_S), Air Outlet Angle (β), Absolute Tangential Velocity (V_θ), Axial Velocity (V_z), and Relative Velocity (W), of the Flow Across the Passage at 7/8 in. From the Hub (r/r_t = 0.55).

Outline Angle of the Relative Flow.

Outlet Angle of the Relative Flow. The circumferential variation of outlet relative air angle (β) is plotted in Figures 23a, 24a, and 25a, respectively, for R = 0.975, 0.77, and 0.55. Appreciable variation of relative air angle occurs only near the tip. At the blade tip, the flow is overturned both at the pressure and suction side of the blade passage. The mid-passage has nearly design flow. This suggests that the radial movement of the blade boundary layers has a predominant effect in deviating the relative flow from the design values. The leakage flow tends to underturn the fluid all along the passage. It was anticipated that the radial movement of the blade boundary layer, when encountered by the annulus wall, tends to deflect towards mid-passage and then radially inward (Figure 7). If this is the case, the flow should be overturned near the pressure surface, and underturned near the suction surface, of the passage. However, contrary to these expectations, there is overturning even near the suction surface.

Velocity Profiles. Some qualitative conclusions about the boundary layer characteristics on the blade at the trailing edge can be drawn from the total relative-velocity (W) plots (Figures 23b, 24b, and 25b). The boundary layer thickness near the trailing edge of the blade tip (Figure 23b) seems to be of the same order of magnitude on both the pressure and suction surfaces, even though the profiles are different. This part of the passage probably has "fully developed" flow, even though the measured velocity deficiency at the center of the wake is small. Since the distance from the trailing edge to the measuring station along the flow path is large (even though the measurements were carried out at an axial distance of 1.73 cm from the trailing edge, the flow path in the direction of the relative velocity is nearly 6 cm), there are reasons to believe that the blade wake has diffused considerably between the trailing edge and the measuring station. Measurements carried out inside the blade passage provide more information on the nature of the profile and the diffusion characteristics of the wake. At the mid-radius (Figure 24b), the growth of the boundary layer is confined to the suction surface of the passage. Near the hub, the relative velocity is fairly uniform across the passage and the boundary-layer growth seems to be negligibly small.

Circumferential variation in absolute tangential velocity (Figures 23b, 24b, and 25b) is large near the tip, and the variation decreases towards the hub.

Circumferential variation of the axial velocity at various radii are plotted in Figures 23b, 24b, and 25b. The axial velocities are fairly uniform across the passage. The rotating pitot tube and wedge-probe measurements revealed no back-flow at any of the radii. The measurements are obtained only at three radial positions, and re consistent with the axial-velocity distribution shown in Figure 9. The axial velocity distributions derived from the rotating pitot tube measurements are far more reliable than those obtained from the stationary pitot and tuft probe.

Measurements carried out at two consecutive passages indicate that the variation in flow properties is as much as 10 percent in some locations (Figures 23 to 25).

Attempts were made to study the periodic part of the tangential-velocity profile using a stationary hot-wire probe aligned in the axial direction at station 3a (Figure 4). The hot wire aligned in the axial direction would pick up the resultant tangential and radial velocities. Since interest lies in the periodic part of the velocity profile, a signal-averaging technique is employed to eliminate the non-periodic part of the wake profile (viz., turbulence, noise, etc.). This is achieved by serially adding together the signals obtained from the hot-wire anemometer. The electronic circuit used for this purpose is shown in Figure 26. The C.A.T. (Computer of Averaged Transients), upon a command from the synchronizing signal, samples the data signal at regular intervals and converts each sample into a discrete number of counts proportional to the amplitude of the signal. These counts are then stored at a particular address in the magnetic core memory after being added to the number previously stored.

The results obtained from such an averaging technique carried out at various radii are plotted in Figure 27. One thousand signals were used for the averaging process, and the sampling cycle includes all of the four-blade passages. The circumferential variation in velocity $\sqrt{V_\theta^2 + V_r^2}$ is larger near the tip and decreases towards the hub. It can also be observed from this data that there is appreciable variation of velocity from passage to passage. This may introduce unsteadiness in subsequent passages.

The three components of blade-to-blade absolute flow were measured using a combination of "X" wire and a single-sensor hot wire at station 3a (Figure 4). Details are given in reference [7]. The data was obtained at $R = 0.55$, 0.77, and 0.935. The distribution of three components of velocities, shown in Figure 28, indicates that the radial velocities at most locations are higher than the axial velocities, with maximum values occurring near the blade surfaces. The tangential velocities measured at station 4 using pitot and wedge probes (Figure 23) are in good agreement with those derived from the hot wire (Figure 28). Appreciable discrepancy occurs in axial-velocity distribution. Measurements at other radial locations (reference [7]) indicate a similar trend, with radial velocities larger than the axial velocities at most locations.

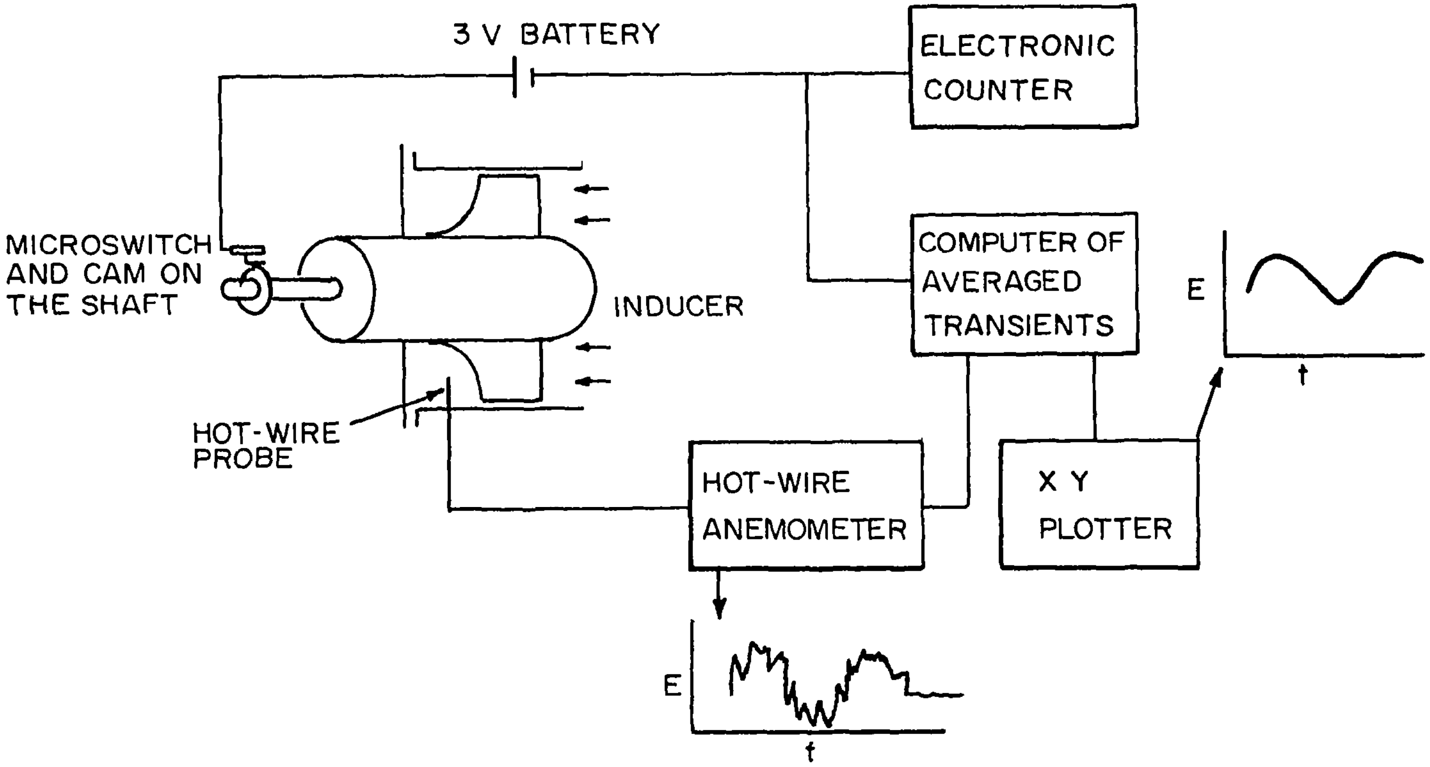

Figure 26. Electronic Circuit Used for Measuring Periodic Wake Profile.

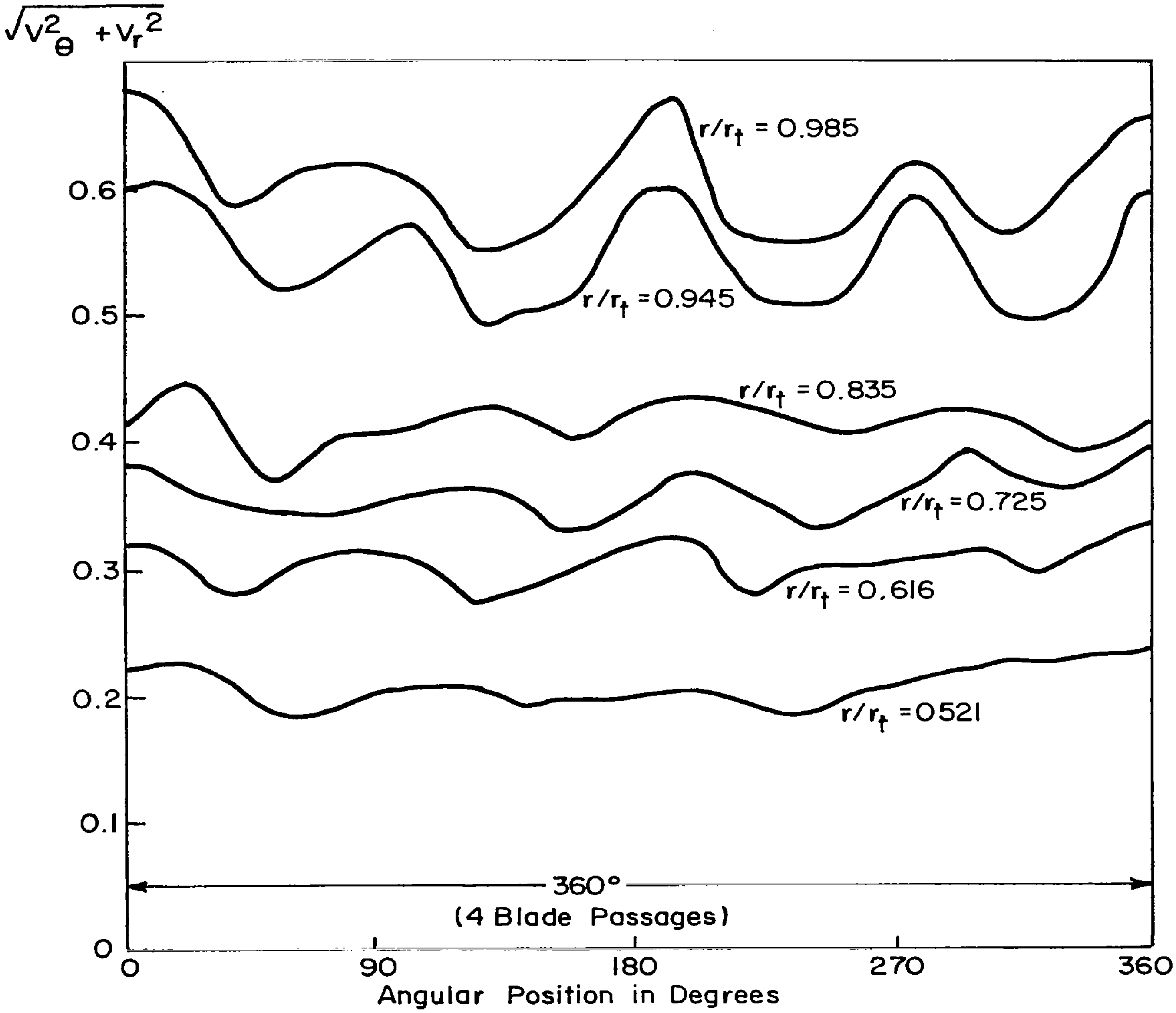

Figure 27. Variation of Absolute Tangential Velocity in the Circumferential Direction Obtained from Hot Wire and C.A.T.

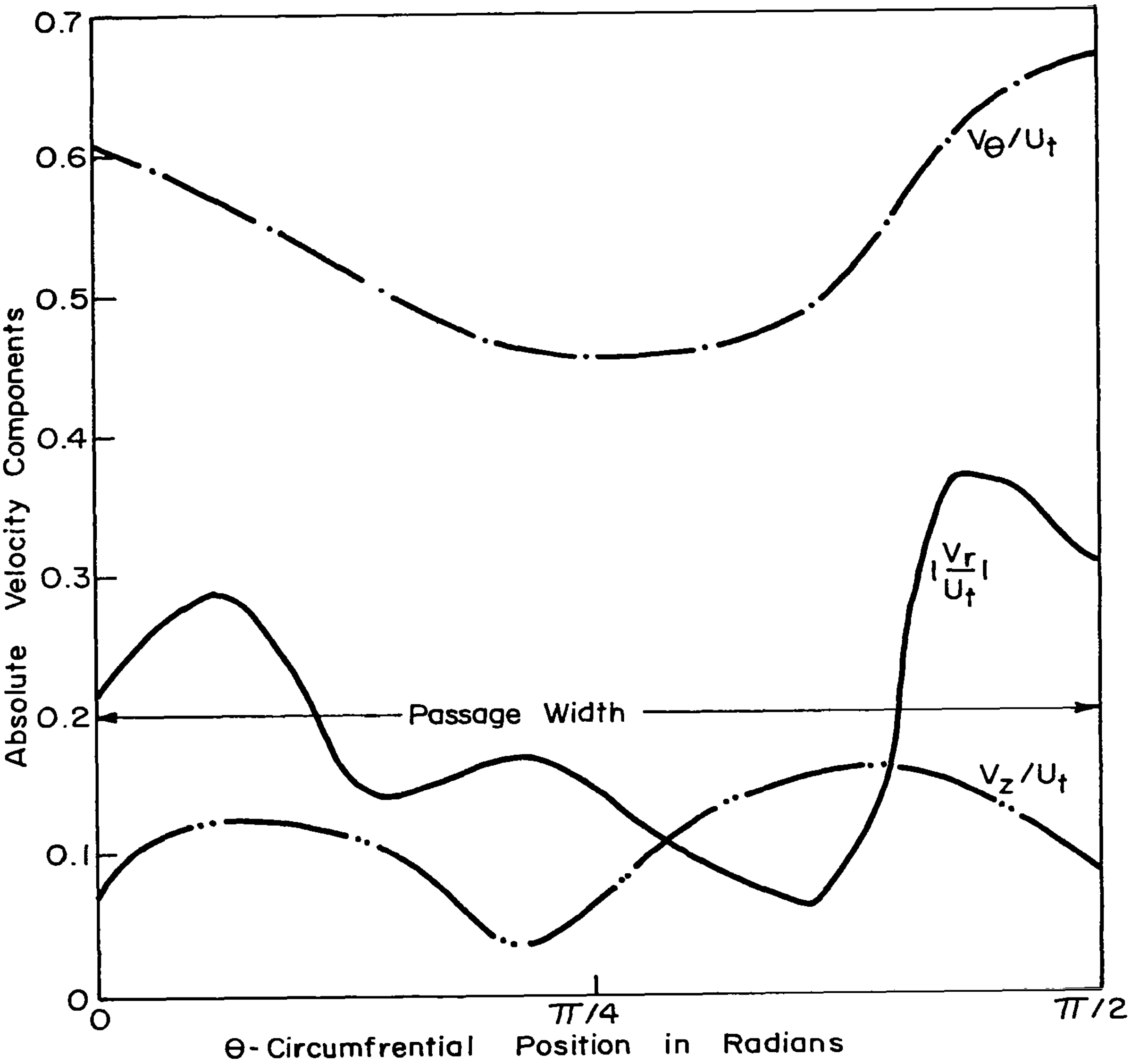

Figure 28. Blade to Blade Variation of the Absolute Flow Velocities Derived from the Hot Wire Measurements at Station 3a (R = 0.935).

Blade-to-Blade Distribution of Flow Properties at the Exit of the Three-Bladed Inducer

A new method of measuring the three velocity components and the corresponding turbulent intensities was developed. This procedure utilizes three stationary hot wires located in the coordinate directions (very near the trailing edge of inducer exit) and has led to valuable information on the blade-to-blade variation of all the velocity and turbulence intensity components [17, 19]. Some typical results and major conclusions derived from these measurements at the exit of the <u>three-bladed inducer</u> at station 2a (Figure 4) are as follows:

1. The radial velocities obtained from the hot-wire measurements are found to be of the same order of magnitude as the axial velocities throughout the flow passage, as shown in Figures 29 and 30. Near the hub, the radial velocities are found to be nearly uniform across the passage [17]; this is presumably caused by the blade blackage. At other radial locations, the radial-velocity distribution across the passage is of the type normally encountered in rotating boundary layers (Figure 30).

2. As shown in Figure 29, almost identical axial-velocity profiles at the exit are derived by both hot-wire and stationary probe measurements. The blade-to-blade variation of axial velocities measured at the exit by means of hot-wire probes is found to be nearly uniform (Figure 31).

3. The blade-to-blade variation of tangential velocities measured by hot-wire probes, shown in Figure 31, indicate peaks near the blade locations. From mid-radius to tip [17], the peaks occur near the mid-passage. The blade-to-blade variation of tangential velocity is found to be generally uniform across the passage.

4. There is a slight discrepancy in the blade-to-blade variation of relative velocities measured by the hot-wire probe and the rotating pitot tube. However, the trend in their distribution is the same. The passage-averaged relative velocities measured by both methods show a considerable departure from the design values from mid-radius to tip. These averaged relative velocities are somewhat lower than those of the four-bladed inducer at these radii. The blade-to-blade variation of the relative velocities derived from the hot-wire data is found to be nearly uniform. This is probably due to considerable wake diffusion that takes place between the trailing edge and the hot-wire measuring station.

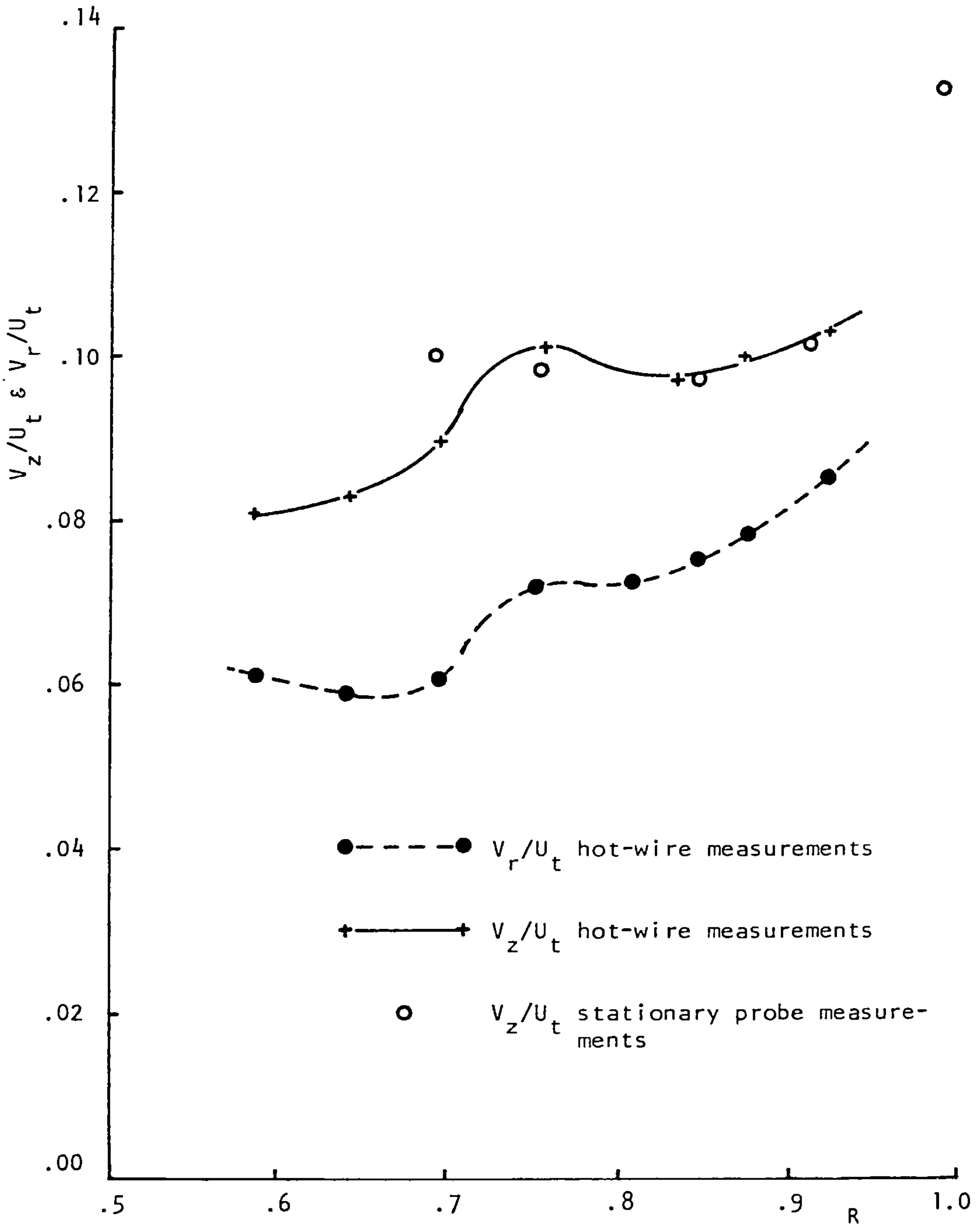

Figure 29. Axial and Radial Velocity at Station 2a for the Three Bladed Inducer.

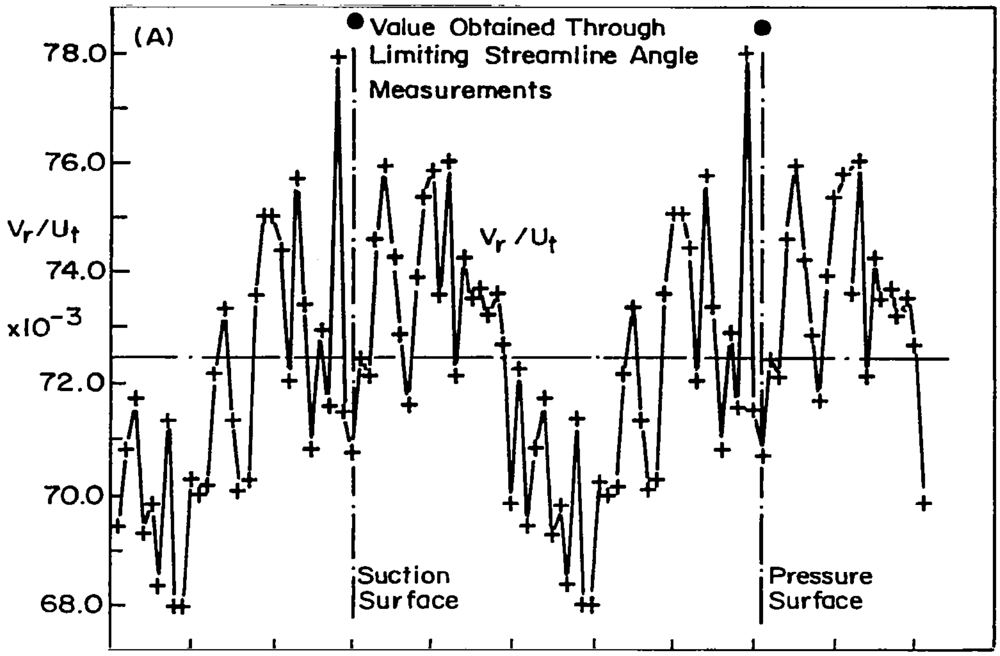

Figure 30. Blade to Blade Distribution of Radial Velocity at R = 0.752, Station 2a (Figure 4) for the Three Bladed Inducer

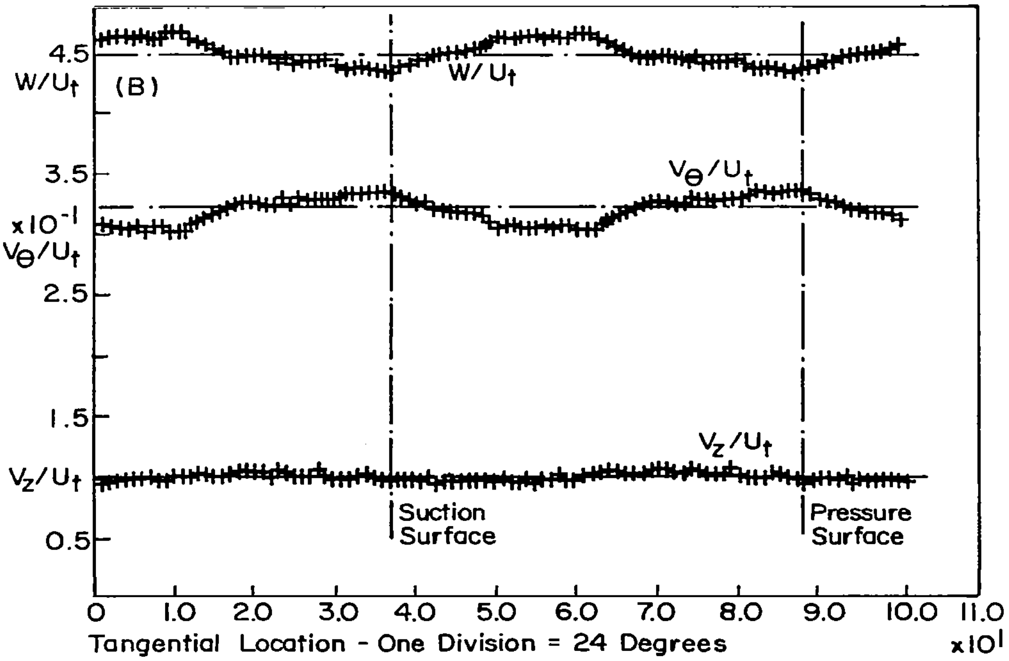

Figure 31. Blade to Blade Distribution of Absolute Tangential and Axial Velocities, Relative Total Velocity at R = 0.752, Station 2a (Figure 4) for the Three Bladed Inducer

5. The turbulence-intensity components (Figure 32) in the radial, axial, tangential, and relative directions (based on local mean-velocity component as defined in Figure 32) are found to be about 75 percent, 45 percent, 20 percent, and 15 percent, respectively. Although maximum values in radial and axial turbulence intensities are observed in the boundary layer interaction region at $r/r_t = 0.860$, the turbulence intensities are found to be rather uniform in the entire flow passage. These measurements reveal the highly turbulent nature of the flow in inducers.

6. It is also evident from these measurements that the wakes from inducer rotor blades decay rapidly. The defect in total velocity (Figure 31) is found to be less than 10 percent even at 6.3 mm from the trailing edge. This represents approximately 18.5 mm in the streamwise distance or about 1.5 percent of the chord length. Recent investigations have revealed that the rotor blade wake decays more rapidly than the wake of a corresponding stationary blade. The decay of the inducer blade wake seems to be more rapid than the compressor rotor blade wake reported in reference [29].

7. It is evident from these measurements that distribution of axial, tangential, and relative velocities are similar for both the four- and the three-bladed inducers (compare Figures 24b and 31), even though the tangential velocities are higher for the three-bladed inducer.

Blade Static Pressure and the Limiting Streamline Angle

Some of the blade static pressures and the limiting streamline angles for the four-bladed inducer are reported in references [16] and [12], respectively. The blade static pressures (ψ_s) reported in Figures 3 and 4 of reference [16] are the only ones that were measured for the four-bladed inducer. Most extensive blade-pressure distribution was carried out for the three-bladed inducer and is reported in references [18], [20], and [21].

The ammonia trace technique provides a satisfactory method for determining blade limiting streamline angles within the rotating inducer blade passages. The blade limiting streamline angle measurements provide several observations which have either been noted in previous investigations or have been found from other experimental results quoted in references [6] through [24]. These include: an increase in ε from the leading edge to the trailing edge, indicating the existence of higher radial velocities as the flow proceeds downstream within the inducer channel; higher values of ε near the hub indicating higher radial velocities in this region; negative values of ε at the pressure surface tip (up to 45 percent chord) indicating radially inward flow due to the presence of the annulus-wall boundary layer scraping effect; and values of α greater than 90 deg near the hub trailing edge indicating the existence of a back-flow region in this area.

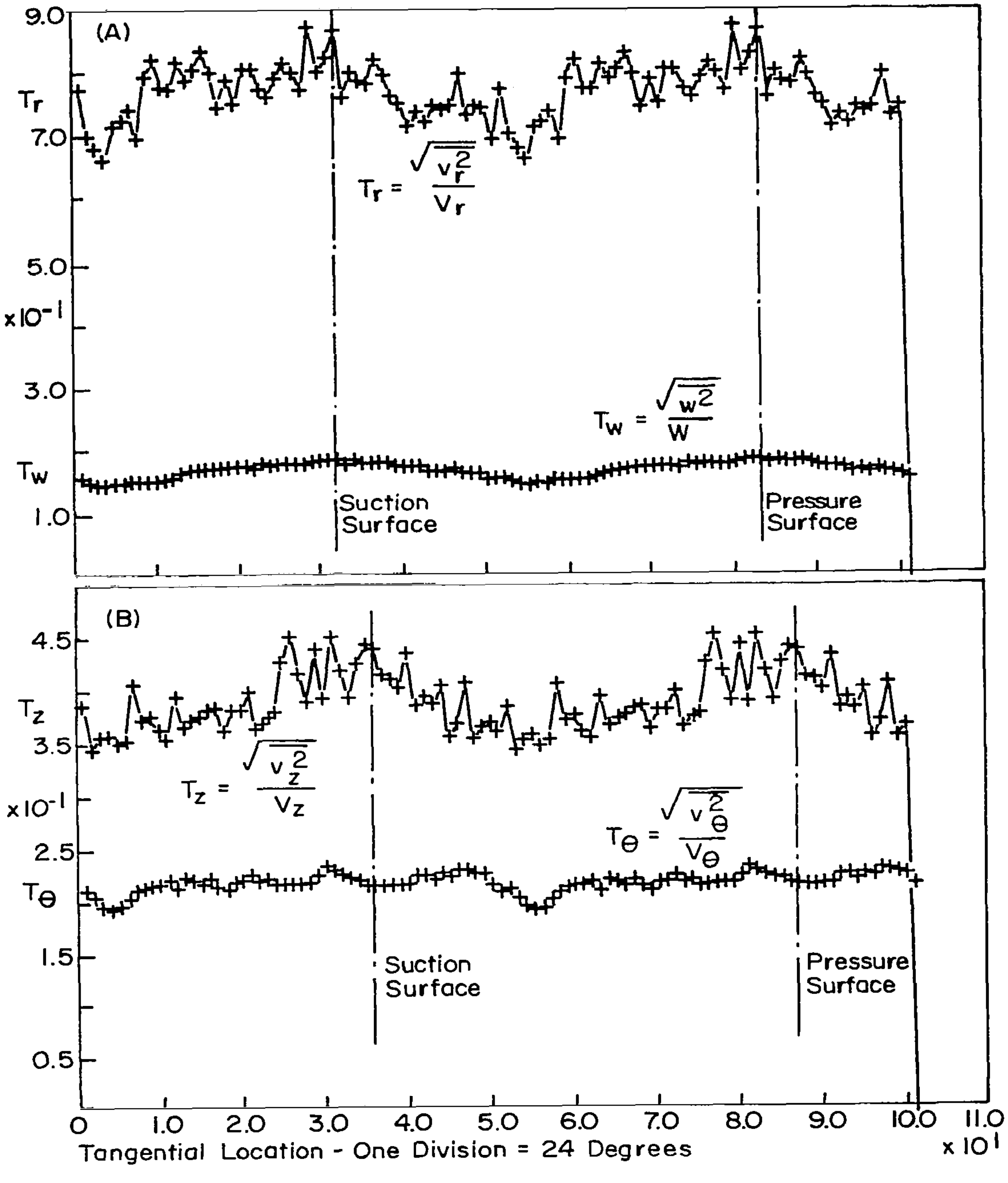

Figure 32. Blade to Blade Distribution of Turbulence Intensities, T_r, T_w, T_z, T_θ, at R = 0.752, Station 2A (Figure 4) for Three Bladed Inducer

The limiting streamline angles for both three-bladed and four-bladed inducers at the leading edge, station 1 (1/3 chord), and station 2 (trailing edge) inside the passage (Figure 4) are compared in Figure 33. It is evident from this figure that the limiting streamline angles near the leading edge, including station 1, are generally higher for the four-bladed inducer, even though the trend is reversed near the trailing edge. The radial inward velocity, near the mid-passage of the tip section, seems to be higher for the four-bladed inducer.

The experimental blade static-pressure distributions, shown in Figure 34 for the three-bladed inducer, confirm the trailing-edge loading characteristic inherent in the inducer blade design. The magnitudes of ψ_s are considerably higher than the design values, indicating the significant effect of three-dimensionality in the inducer flow. The static-pressure distributions display small negative ψ_s values near the leading edge of the suction surface. It is evident that the discrepancy between the design and measured values is large.

Measurements Inside the Blade Row (Pressure Probes)

In order to understand the flow behavior inside the inducer passages, experimental investigation of the relative flow (blade-to-blade) inside the inducer passages was undertaken using rotating probes and the pressure-transfer device. Pressure-probe measurements inside the four-bladed inducer are reported in references [6], [7], and [16] and for the three-bladed inducer in references [9], [10], [14], [16], [17], and [21]. The flow is surveyed in one passage (at two axial locations, one at about 1/3 chord length from the leading edge and the other near the trailing edge, designated as stations 1 and 2 in Figure 4, and at several radial locations. Some of the major conclusions derived from measurements in four-bladed inducers are presented in references [6], [7], and [16], as follows:

1. The measurement of relative flow near the trailing edge reveals the presence of a loss core located slightly inward from the tip. The mid-passage at this radius is found to have minimum relative stagnation pressure and, hence, maximum loss. The radial velocity inside the blade boundary layer, when encountered by the annulus wall, tends to deflect towards the mid-passage and then move radially inward. These interaction effects are responsible for large losses observed experimentally. These loss regions extend from mid-radius to tip.

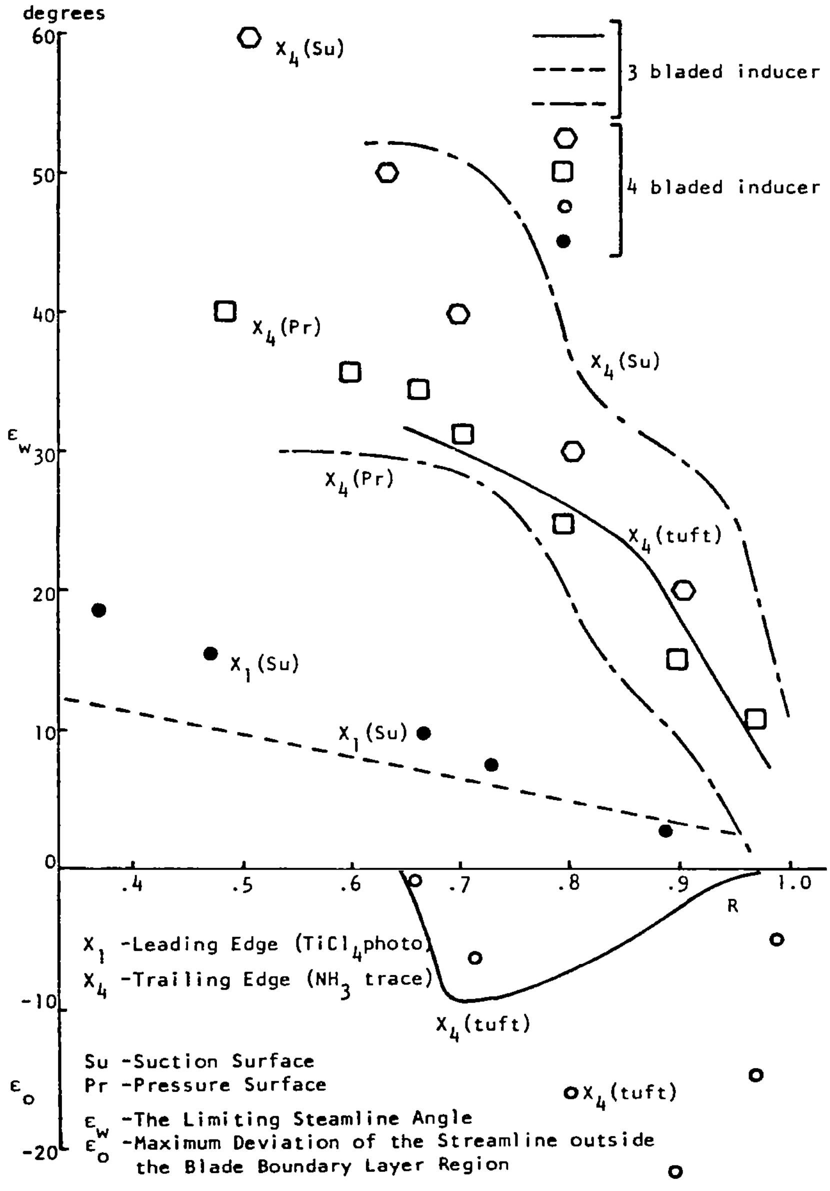

Figure 33. Radial Variation of ε_o and ε_w at Various Chordwise Locations

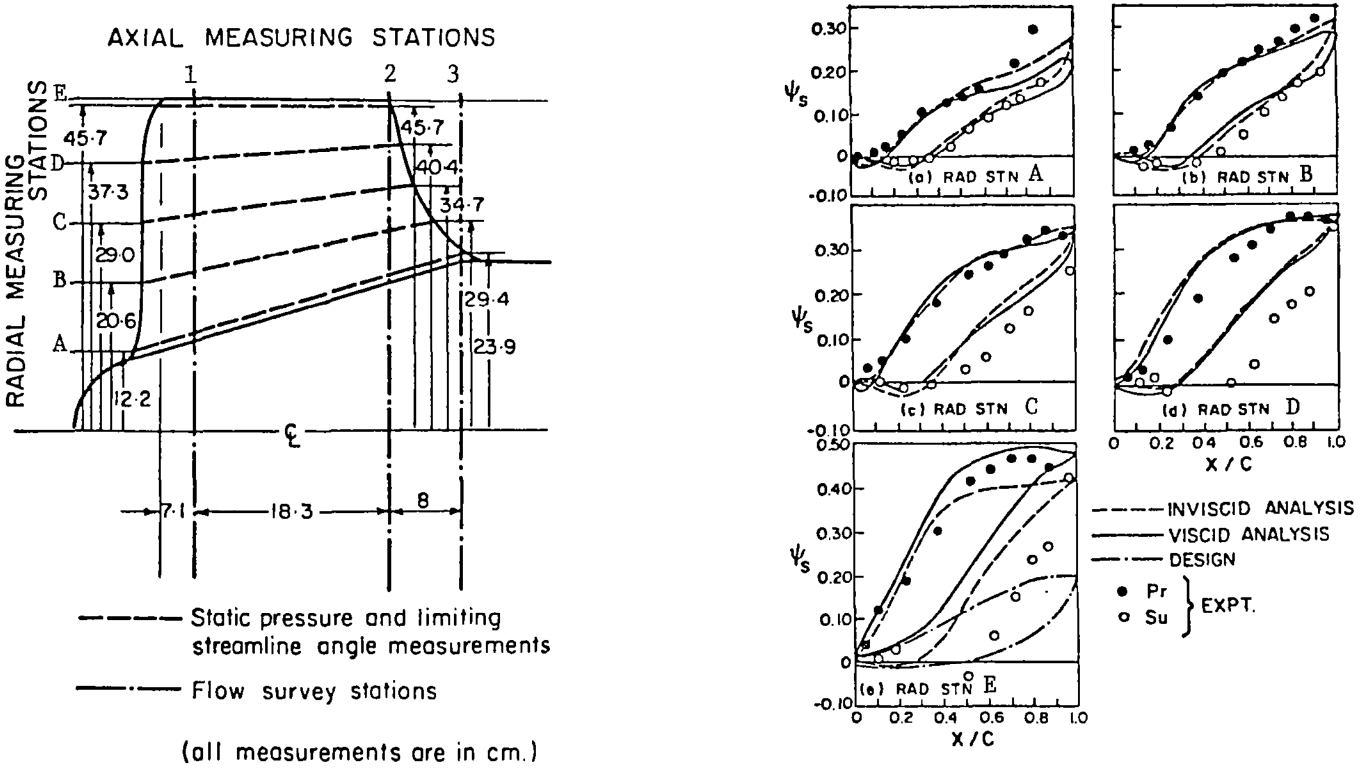

(a) Location of Flow Measuring Stations

(b) Blade Static Pressure Distribution

Figure 34. Location of Flow Measuring Stations and Blade Static Pressure Distribution at Radial Stations A, B, C, D, and E.

2. A substantial portion of total flow losses occurs near the leading edge. This is probably due to the presence of the laminar region, the consequent large radial flows, and the associated mixing near the tip. The losses near the tip are found to be about five times those at other radii (see Figure 11 in reference [16]).

3. The blade boundary layers are found to be quite thin near the hub. The boundary layer thickness near the mid-radius is about 25 percent of the blade passage, being thicker on the suction surface than on the blade pressure surface. The relative-velocity profile from mid-radius to tip shows appreciable defect outside the blade regions, as shown in Figure 35.

4. A conventional boundary layer type of profile exists from hub to mid-radius (Figure 35); whereas, the velocity profile near the tip (mid-radius to tip) is of conventional type near the blade surfaces and "wake" type near the mid-passage. Qualitative reasons for the existence of this type of profile are discussed in reference [16].

5. Near the trailing-edge station, the passage-averaged values of relative velocity have a maximum value at mid-radius, being considerably lower than the design values from mid-radius to tip, as shown in Figure 35. The diffusion of relative flow is caused mainly by the inviscid turning effects from hub to mid-radius; whereas, the diffusion from mid-radius to tip is dominantly influenced by the viscid and "shear pumping" effect.

6. The wall shear stresses estimated from the blade boundary-layer profiles appear to be much higher than those of an equivalent stationary channel, especially from the mid-radius to the tip.

7. The contour plot of the absolute stagnation-pressure rise coefficient derived from rotating probe measurements indicated that the large head rise from hub to mid-radius is confined to the blade boundary layer region; but at other radial locations the head rise is much larger than the design values at all of the passage locations, as shown in Figure 36.

Solidity Effect. The following conclusions are derived by comparing the relative-flow measurements taken in the three-bladed inducer with those of the four-bladed configuration [16,17].

8. Measurements taken near the leading edge show marked reduction in boundary layer growth, flow losses, and radial inward velocity in the case of the three-bladed inducer. The losses near the tip are nearly halved from those of the four-bladed inducer, and the "wake" type of profile observed near the mid-passage of the tip disappears in the case of the four-bladed inducer, as shown in Figure 37.

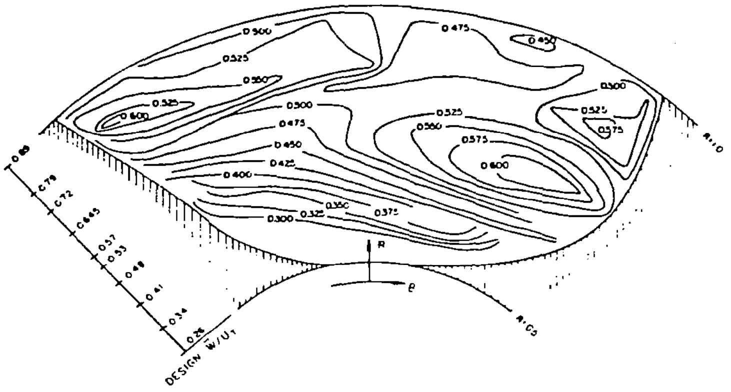

Figure 35. Contours of Iso-Relative Velocity (W/U_t) at Station 2 for Four Bladed Inducer.

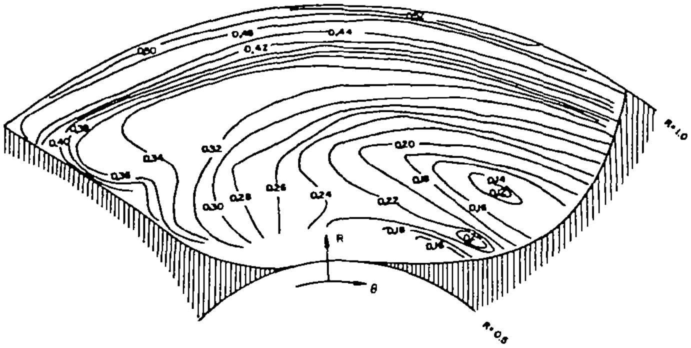

(a) STATION 2

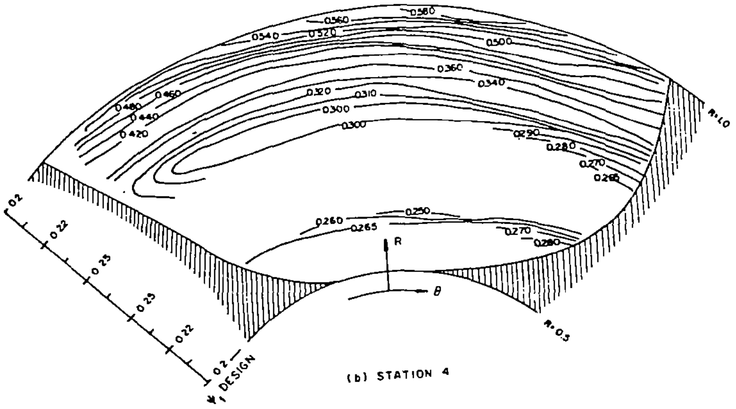

(b) STATION 4

Figure 36. Contours of Constant Stagnation (Absolute) Pressure Rise (ψ_t) for Four Bladed Inducer.

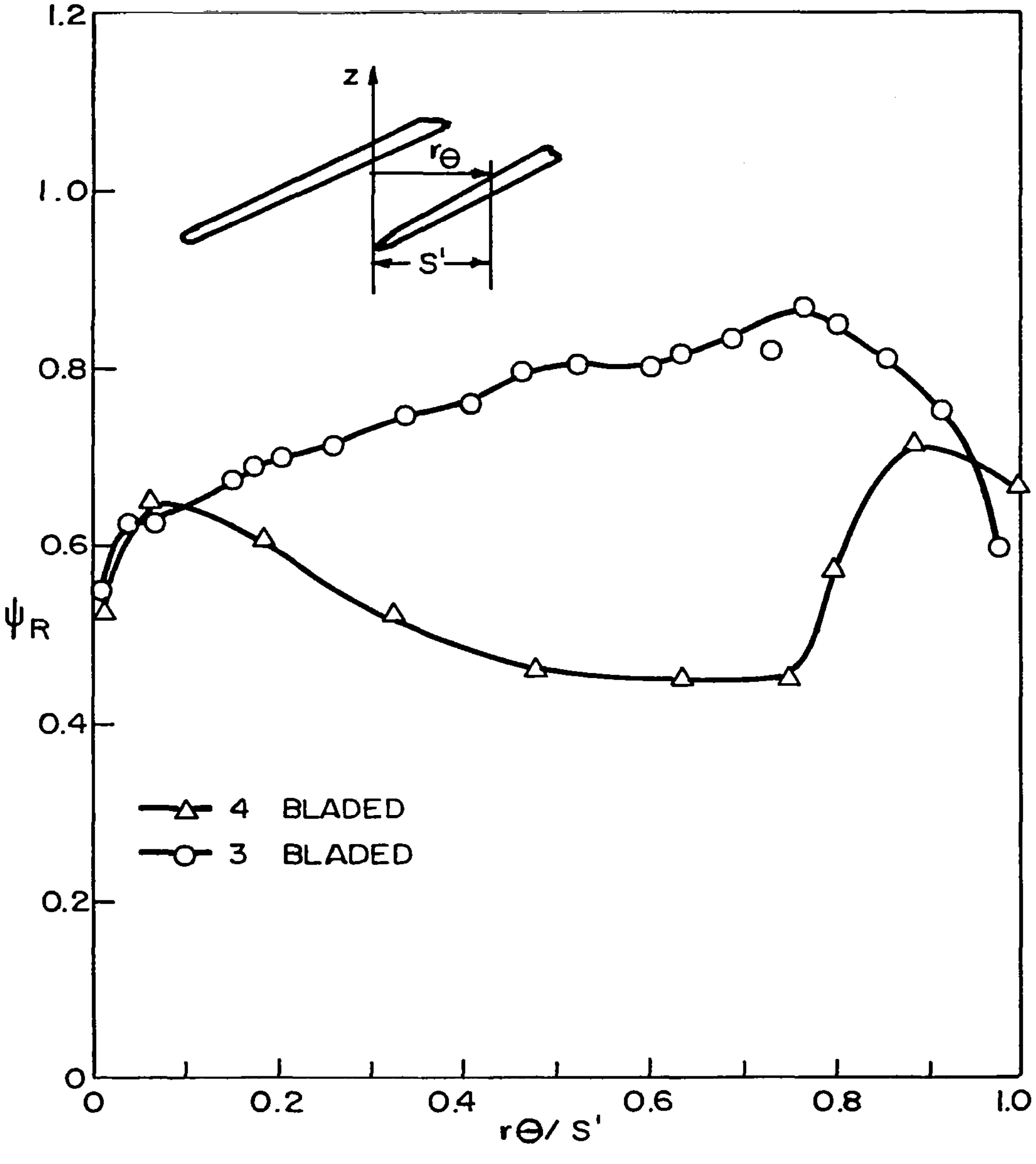

Figure 37. Stagnation Pressure Coefficient of the Relative Flow at Station 2 (Figure 4) for R = 0.975 for Four and Three Bladed Inducers.

9. Measurements taken near the trailing edge indicate that the relative velocity and pressure distribution (blade-to-blade) is similar for both of the inducers, even though there is appreciable reduction in losses, as well as relative flow diffusion, in the case of three-bladed configuration (reference [16], Figure 13).

10. There is appreciable improvement in hub and wall static-pressure distributions in the case of the three-bladed inducer. The negative pressures observed near the leading edge of the four-bladed inducer is substantially reduced in the three-bladed inducer (reference [16], Figure 9).

Measurements Inside the Blade Passage of a Three-Bladed Inducer Using Hot-Wire Probes

Detailed measurements of mean velocity and turbulent flow field inside the three-bladed inducer were carried out using the rotating hot-wire technique described earlier. The details are given in references [14], [18], [20], and [21]. The flow was measured at various radii and across the blade at stations 1 and 2 (Figures 4 and 34).

Total relative-velocity profiles, derived from the rotating tri-axial hot-wire measurements, indicate a substantial velocity deficiency near the tip at mid-passage which expands significantly as the flow proceeds downstream toward the inducer trailing edge (Figure 38). This indicates the considerable extent of flow mixing due to boundary layer interaction, radially inward and outward flow, annulus wall effect, etc. which is prevalent at this location inside the long narrow passages of the inducer. The position of this "loss core" appears to drift closer to the blade suction surface as the flow proceeds toward the inducer exit.

The high values of absolute tangential velocity which are found to exist near the inducer tip indicate a region of large absolute stagnation-pressure rise caused by the effects of complex viscous interactions. The size and severity of this region increases significantly as the flow proceeds downstream inside the inducer blade channel. This observation is also predicted from the three-dimensional theoretical analysis reported later in the report.

The higher values of axial velocity near the hub, shown in Figure 38, indicate the significant effect of blade blockage within the inducer flow passage. A slight back-flow was found to exist at the extreme tip location of flow at station 1 and can be attributed to the annulus wall boundary-layer scraping effect identified in the limiting streamline angle (ε) measurements.

The measured magnitudes of radial velocity are found to be on the same order as those of axial velocity within the inducer passage. This is similar to the results of reference [17] which were made slightly downstream of the inducer trailing edge. The large values of radial velocity confirm the highly three-dimensional

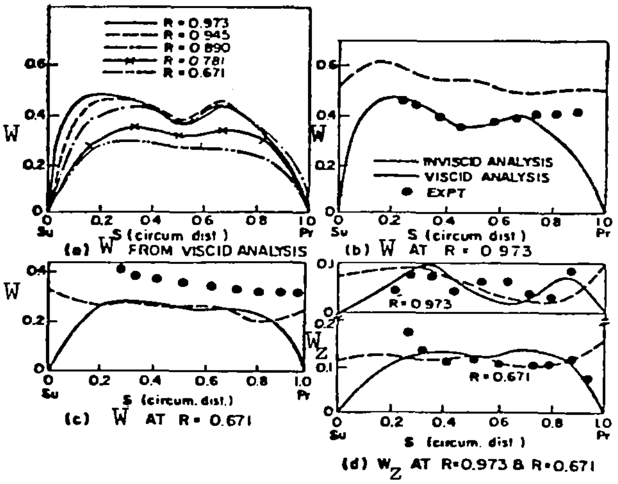

Figure 38. Comparison Between Theory and Experiment of the Blade-to-Blade Distribution of Total Relative Velocity (W) and Axial Velocity (W_z) at Station 2 for the Three Bladed Inducer.

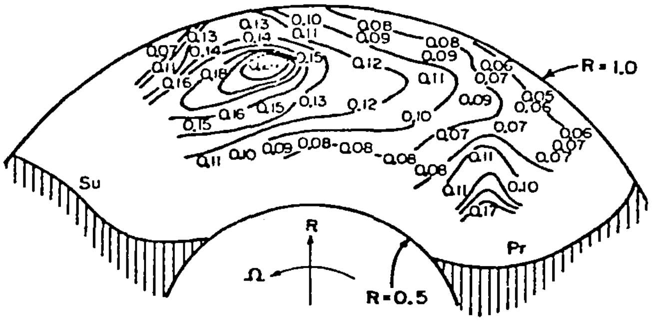

(a) RADIAL TURBULENCE INTENSITY ($\sqrt{w_r^2}/W$)

Figure 39. Radial Component of Turbulence Intensity at Station 2 for the Three Bladed Inducer

characteristics of the inducer flow and emphasize the necessity for a three-dimensional theory for accurate flow analysis. The radial velocities are generally found to decrease in magnitude from hub to tip and increase from leading edge to trailing edge. These observations are consistent with the measurements mentioned previously. A region of radially inward flow is found to exist near the mid-passages of the tip region and correspond to the locations of the velocity deficiencies noted in the W distributions. These measurements support the explanation for the existence of the large flow losses in this region due to extensive flow mixing and complex viscous interactions. The magnitudes of radial velocity predicted from the theoretical analysis are significantly lower than the experimental results. The radially inward flow found experimentally near the tip mid-passage has been predicted with the three-dimensional theoretical analysis described later.

Turbulence levels within the blade passage, indicated from the experimental results, are generally high near the tip regions. A growing core of high turbulence is evident near the tip mid-passage, corresponding to the region of velocity deficiency mentioned in the above paragraph. High turbulence levels are also recorded near the hub pressure surface and indicate the influence of the pressure-surface boundary layer. The radial component of turbulence intensities appears to have the largest magnitudes (shown in Figure 39) reaching values of up to 24 percent in the mixing region. The total turbulence energy contours are similar to those of the turbulence intensities.

The locations of high turbulence stresses are concentrated in the high turbulence intensity areas of the mixing region and near the hub pressure surface. Values of the streamwise Reynolds stress appear to be higher in the mixing region than the corresponding values of the radial components of Reynolds stress. The high-stress regions are indications of areas subjected to complex viscous interactions.

Experimental velocity and turbulence results of reference [20] show nearly uniform distributions slightly downstream of the inducer trailing edge. Thus, it appears that considerable wake diffusion occurs immediately after the trailing edge to decay the turbulence core and blade blockage effects measured.

BOUNDARY LAYER AND RELATED PHENOMENA ON INDUCER BLADES AND PASSAGES

The boundary layers that develop on the blades of rotating machinery such as compressors, pumps, inducers, propellers, and turbines are not two-dimensional. The rotation of the blade produces spanwise flow, resulting in a skewed or three-dimensional boundary layer. The extent of three-dimensionality depends on the angular velocity, the flow coefficient, space/chord ratio, aspect ratio, stagger angle of the blade, etc. A basic understanding of the effects of centrifugal and Coriolis forces on the boundary layer behavior is essential for the improved analysis and performance of such rotating fluid machinery. While a considerable amount of information on the viscous flow in a non-rotating flow passage was available, there was no information for the rotating case. A systematic study of the boundary layer on a rotating blade and inside a rotating channel was undertaken.

In the first phase of the program, the boundary layer on a simpler configuration, namely, a rotating helical blade of large chord length enclosed in an annulus, was studied [8,10,13]. The configuration used in this study is shown in Figure 2. In the absence of chordwise pressure gradients, the effect of rotation on the boundary layer can be discerned.

The interference due to adjoining blades ("channel effect") that exists in turbomachinery passages is not simulated in the above model. The radial flow inside the boundary layer, when encountered by the annulus wall, produces a complex flow near the tip, resulting in a radially inward flow. These and other interaction effects result in extremely complex boundary layer characteristics. With this as an objective, studies of the influence of the rotation and "channel effects" as well as pressure-gradient effects were carried out in a rotating channel, with the geometry of a four-bladed flat-plate inducer [14,22,23,24]. The geometry used for these studies is shown in Figure 3, and the derived conclusions are described below.

Boundary Layer on a Single Rotating Helical Blade

The configuration used for the analytical and experimental investigation of the boundary layer on a single rotating helical blade is shown in Figure 2. The analysis [13] was based on the momentum integral technique. The measurement of the radial and chordwise velocity profiles, skin-friction coefficient, and the limiting streamline angles was carried out at various chordwise and radial locations [13,8]. The limiting streamline angles were visualized by means of the ammonia streak filament method. Typical traces are shown in Figure 40.

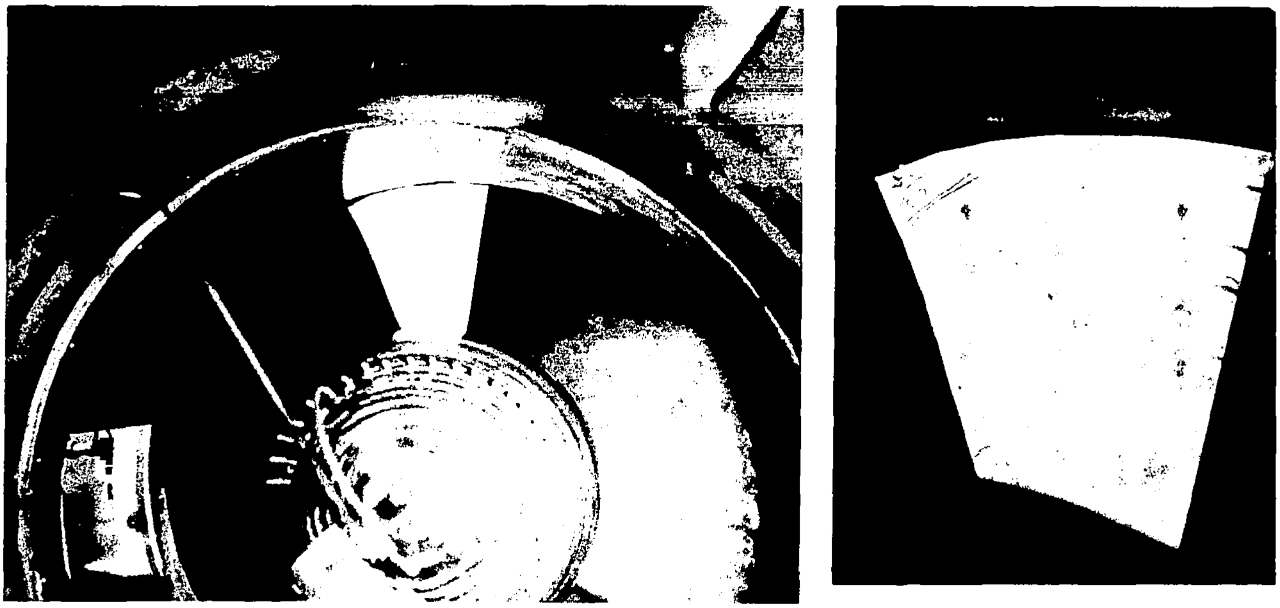

Ammonia Streak Technique of Visualizing the Limiting Streamline - Insert on the right corner shows the photograph of the streamlines

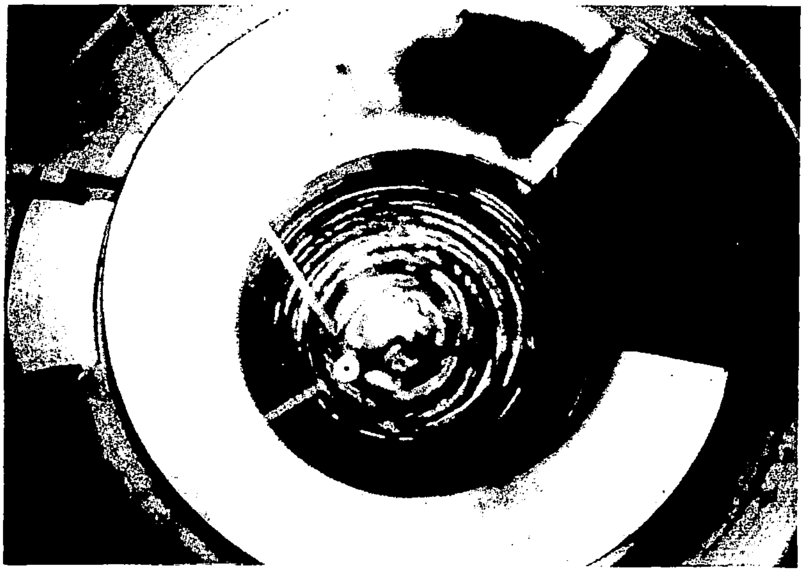

Visualization of the Location of Flow Transition Zone

Figure 40. Visualization of Flow on a Rotating Helical Blade

The following conclusions may be drawn from the theoretical and analytical investigations carried out on a single rotating helical blade [8,13]:

1. The solution of the momentum integral equations predict, accurately, the boundary-layer growth and the limiting streamline angle ε at various locations on the rotating-blade surface. Although the effects of physical constraints due to annulus and hub walls are neglected, these predictions seem to agree closely with the experimental observations at all radii except very near the tip. Large departure from the asymptotic disk values of the boundary-layer thickness at the tip may be due to substantial turbulence mixing and interaction between the annulus and the blade boundary layers.

2. The agreement between the assumed tangential-velocity profile and the measured values is good, except near the tip. The tangential velocity can be represented by Cole's law of the wall and wake.

3. The radial velocities measured show a substantial departure from the assumed profile (Mager's profile [32]). It is concluded that neither Mager's nor Johnston's triangular model give a fair representation of the radial-velocity profile for a rotation-induced radial flow. An analysis of the outer layer, which is assumed to be essentially inviscid, gives a radial velocity represented by

$$\frac{W_r}{\Omega r} = c_1 \sqrt{W_s/\Omega r(1 - W_s/\Omega r)}$$

where W_r = radial velocity, W_s = chordwise component (in the cylindrical-plane) of velocity, and c_1 is a constant. The latter is found to be about 0.3 from extensive measurements. The measured radial velocities show good agreement with the above equation in the outer layer. In reference [10], it has been proven that the inner layer is collateral and can be represented by

$$W_r = W_s \tan \varepsilon$$

where ε = limiting streamline angle.

4. About 100 skin-friction measurements carried out at various radial and tangential locations of the blade and at several rotational speeds indicate that the skin-friction coefficient on a rotating blade can be represented by

$$\frac{c_f}{c_{fo}} = 1 + 0.85\, R_o^{1/2}$$

where $R_o = \varepsilon\theta$, the theoretically derived rotation number (ratio of the Coriolis force to the inertial force inside the boundary layer), and c_{fo} = skin-friction coefficient for a flat plate at zero pressure gradient. A similar expression is given for the developed region of the flow.

5. The flow at the tip shows a behavior very different from those at other radii. It is seen that as the distance from the blade surface increases, the tangential velocity component increases, and reaches a value lower than the free stream velocity Ωr. This region is followed by one where the tangential velocity changes very little, and may be considered constant; hence, the terminology "core." Then the tangential velocity increases, approaching the free stream value asymptotically. A heuristic argument for this type of flow behavior is given in reference [13].

6. The turbulence intensities (chordwise component) measured on the rotating blade are found to be higher than the flat-plate values [33] in the entire boundary layer region.

7. The blade static-pressure measurements indicate that appreciable pressure gradients exist only near the tip, the gradient being negligible at all other radii.

8. The flow transition is found to occur earlier than that of a flat plate, and the wake is found to decay faster than the wake of a stationary body. These effects indicate the influence of rotation and radial velocity. A photograph of the transition region obtained by flow visualization (sublimation technique [8]) is shown in Figure 40.

Boundary Layer Development in a Flat-Plate Inducer Channel

In an axial-flow inducer, the interaction between the pressure surface and suction surface boundary layers would result in an extremely complex flow, especially near the outer half of the blade span. Since these interaction effects are very complex, experimental investigation assumes a very important role in this program. These effects were studied in a helical channel specifically designed and fully instrumented for this purpose. This facility is shown in Figure 3. The channel consists of constant-thickness blades of zero camber. The experiment is carried out at zero and other incidences. Details of the program and the Reynolds equation valid for this flow are given in reference [9], and velocity-profile analysis and details of instrumentation in reference [10]. Details on the velocity profiles carried out with mild and strong pressure gradients, as well as detailed analyses, are described in references [22-24].

The model used for this study is essentially a flat-plate inducer with four blades, operated at open throttle and other operating conditions. This should provide information on the effect of centrifugal and coriolis forces in a flow through a long channel, with and without pressure gradients. The rotor had high solidity and a large stagger angle, as is the case of the aerodynamically designed inducer described earlier. The chord length, blade spacing, diameter, and rotational speed are exactly the same as those of the aerodynamically designed inducer. The operating conditions were similar in both cases, while the incidence, blade thickness, and camber differed.

A boundary layer flow analysis was carried out using the momentum integral technique, which employs three-dimensional equations of motion in the rotating coordinate system. The analysis is described in detail in references [22] and [23]. The measurements of the boundary layer characteristics (three components of velocity, turbulence intensities, Reynolds stresses, skin-friction coefficient, limiting streamline angle) were carried out utilizing the conventional and tri-axial hot-wire probes rotating with the rotor inside the passages. Details of the technique are given in references [23] and [24].

Since the results of the investigation on boundary-layer characteristics in inducer channels are well documented in references [22-24], only a brief summary of the program and conclusions are given below.

The theoretical and experimental investigation of the three-dimensional rotating turbulent boundary layer in a helical passage of a turbomachinery rotor shows substantial differences from its stationary counterpart as well as from a single rotating blade. The rotation-induced Coriolis force markedly changes the boundary layer growth, the skin friction, the extent of three-dimensionality, and the turbulence flow characteristics in a rotating channel.

1. The stagnation pressure at the exit of the rotor at zero incidence shows a steep rise in values towards the tip; the increase in stagnation-pressure rise is confined to 20 percent of the blade span near the tip. The absolute tangential-velocity distribution shows a similar trend. Similarity in flow properties in this channel and the inducer at the tip indicate the dominant influence of viscosity and the behavior of the outer half of the inducer as a "drag or shear pump."

2. A collateral region exists very near the wall, even for highly three-dimensional rotating turbulent boundary layers with radial and streamwise pressure gradients.

3. A Power Law representation of the chordwise velocity components fits the data well, provided the radial and streamwise variation of the exponent [(H - 1)/2] in the chordwise velocity profile is taken into account. Cole's representation is possible, but the wake function is different from the sinusoidal form used for the stationary turbulent boundary layers, indicating that the entrainment process in rotating boundary layers is affected by Coriolis and centrifugal forces.

4. Mager's [32] representation of the outward radial velocity (with measured limiting streamline angle) fits the data reasonably well for boundary layers near the mid-radius, but departs considerably when the annulus-wall boundary layer or the boundary layer from an adjoining blade interferes.

5. The velocity profiles in the outer part of the boundary layer agree well with the expression

$$W_r/(W_s)_e = C_1 \sqrt{(2/k - \sin\beta)\,\sin\beta/RG - [W_s/(W_s)_e]^2}$$

where W_s is the chordwise (in the cylindrical plane) velocity, $(W_s)_e$ is the velocity at the edge of the boundary layer, $RG = R/(W_s)_e \;\; \partial(W_s)_e/\partial R$, $k = (W_s)_e/\Omega r$. In the developing region, for the open-throttle case, where the boundary-layer edge velocity is Ωr, $k = 1$ and $c_1 = 0.2$ gives the best fit. It is also clear that the Johnston straight-line fit,

$$W_r/(W_s)_e = C_2[1 - W_s/(W_s)_e] \; ,$$

is inadequate for rotating axial-flow fluid machinery, such as axial-flow compressors and turbines. The above equation clearly shows that the cross-flow is strongly dependent on the stagger angle, local chordwise velocity, and the radial-pressure gradient.

6. Velocity profiles in the interference region near the tip, where the blade and annulus-wall boundary layers produce an intense mixing region, cannot be represented by simple similarity equations. Radial inward flow and appreciable reduction in the streamwise component of velocity characterize this region.

7. There is a large reduction in the passage-averaged streamwise velocity $\bar{W}_s$ downstream of the channel due to the increased radial migration of the flow caused by the pressure gradients. The decrease in relative velocity is very large near the tip in the interference region and is accompanied by the radial inward flows and reversal of shear stresses. This phenomenon plays an important role in producing increased secondary flow losses in an actual rotor. Its existence and its quantitative measurements have not been reported before. The associated intense mixing and the corresponding increase in the end-wall losses must be accounted for in calculating the performance of turbomachinery rotors.

8. The observed values of momentum thickness (θ_{11}) are lower than those for a single rotating blade reported in reference [13], due to larger values of the limiting streamline angle (ε) and the resulting larger radial velocities. θ_{11} is higher on the trailing side compared to those on the leading side. The predictions based on the momentum integral solution agree reasonably well.

9. The observed and the predicted values of limiting streamline angle are much higher than the single blade values and agree well except near the transition region. This is partly due to errors in the location of the transition and partly due to numerical errors involved in assumed sudden transition from laminar to turbulent flow equations.

10. Variation of shape factor (H) is small in the open-throttle case (1.10-1.3 on the trailing side and 1.25-1.5 on the leading side) except near the hub and tip, where the end-wall boundary layers interfere. For a fully loaded rotor, H varies appreciably. Its variation can be incorporated in the prediction of boundary layer growth by using a modified form of Head's entrainment equation.

11. The skin friction coefficient for the rotating channel is found to vary with three important three-dimensional boundary-layer parameters θ_{11}, ε, and H. The proposed correlation for the skin-friction coefficient, based on the limited data in the rotating channel with mild pressure gradients, is

$$C_f = 0.172\, R_{\theta_{11}}^{-0.268}\, 10^{-0.678\, H}[1 + 0.52\sqrt{\varepsilon_w (x - x_t)/C}] \; .$$

The term in the bracket is due to three-dimensional effects. Variation with $R_{\theta_{11}}$ and H is found to be the same as that for a stationary channel.

12. Turbulence intensity measurements show that the radial component $\sqrt{\overline{w_r^2}}$ is larger than the streamwise component $\sqrt{\overline{w_s^2}}$ in a rotating turbulent boundary layer. This trend is opposite to that in a stationary channel and is caused by rotation.

13. Turbulent shear stress measurements show that in three-dimensional rotating turbulent boundary layers, all three of the velocity cross-correlations are of the same order of magnitude inside the boundary layer. They behave similarly if the pressure gradients are negligible, and can have opposite signs depending on the nature of the chordwise and radial pressure gradients.

14. Both the turbulence intensity and shear stress measurements in the interference region (near the tip) show a large increase in its magnitude. The turbulent stresses vary almost linearly in the direction normal to the boundary layer, and have opposite signs compared to the values near the blade surface. This large gradient in turbulence intensity and shear stress is due to an intense mixing zone caused by the interaction of the two boundary layers resulting in increased flow losses in this region.

ANALYSIS OF THE INDUCER FLOW FIELD

Five different types of analyses were carried out to predict the inducer flow field. These can be classified as follows:

1. An axial-velocity profile prediction at off-design conditions [30,34].

2. An approximate viscid analysis based on the empirical loss coefficient [15,17].

3. An approximate viscid analysis based on shear pumping effect [25].

4. A three-dimensional inviscid analysis [17,18,21] based on the computer program developed by Cooper and Bosch [35].

5. A three-dimensional viscid analysis (numerical) based on empirical wall shear stress [18,21].

These analyses are briefly described below. Details can be found in the references quoted.

Axial-Velocity Profile at Off-Design Conditions

The simplified radial equilibrium equation in combination with the integral form of the continuity equation is used to derive an expression for the radial distribution of the axial velocity at various off-design conditions for the <u>four-bladed inducer</u> used in this investigation. It is an extension of Huppert's [34] analysis for a flat-plate inducer, where r tan β = constant. This has been extended in reference [30] for any arbitrary inducer. The final expressions for the four-bladed inducer used in this investigation (for which r^2 tan β is nearly constant) are given by

$$\frac{V_{z_2}}{V_{z_m}} = \frac{1}{Y}\left[Y_m + \frac{\tan \beta_t}{\phi}\,\frac{\bar{V}_{z_1}}{V_{z_m}}\,(R^2 - R_m^2)\right] \tag{8}$$

$$\frac{\bar{V}_{z_1}}{V_{z_m}} = \frac{2K\,Y_m \int_{R_h}^{1.0} (R/Y)\,dR}{1 - 2\tan \beta_t/\phi \left[\int_{R_h}^{1.0} (R^3/Y)\,dR - R_m^2 \int_{R_h}^{1.0} (R/Y)\,dR\right]} \tag{9}$$

where $\phi = \bar{V}_{z_1}/\Omega r_t$, $Y = (\tan^2 \beta_t + R^4)^{3/4}$,

$Y_m = (\tan^2 \beta_t + R_m^4)^{3/4}$, $r_m = \sqrt{(r_t^2 + r_h^2)/2}$,

k is a blockage factor to allow for blade thickness and boundary-layer growth, and V_{z_m} is the axial velocity at the hydraulic mean radius r_m. This analysis neglects the viscous effects.

For any given flow coefficient, $\bar{V}_{z_1}/V_{z_m}$ is calculated using equation (9), which is then substituted in equation (8) to predict the axial velocity at various radii. The prediction for the four-blade inducer, shown in Figure 41, confirms the results from flow visualization and measurements reported earlier. It should be recognized that the above analysis does not take into account the viscous effects; hence, the tendency for the back-flow to occur near the hub at the design condition is not predicted. The tendency for flow reversal at the root at flow coefficients lower than the design value is, however, correctly predicted.

Viscid Analysis Based on the Empirical Loss Coefficient

An approximate analysis of the inducer flow, based on an empirically derived friction-loss coefficient, is reported in reference [15]. The salient points of this analysis are discussed below.

Inducer data collected from various sources (NASA, M.I.T., TRW, etc.) indicate that the measured friction losses are several times higher than those of an equivalent stationary inducer channel, especially near the tip. The friction losses in an inducer are strongly dependent on the rotation factor (inverse of flow coefficient). A new friction-loss coefficient applicable to inducers operating in the range of flow coefficients $\phi = 0.065$ to 0.2 is defined and derived. The frictional losses estimated from this newly defined friction-loss coefficient agrees well with the measured values for the Penn State inducer.

The loss coefficient is given by

$$\zeta = \psi_{loss} = \frac{2g\,H_{loss}}{U_t^2} = \lambda_R \frac{R_{ht}}{\phi} \frac{1}{R_N^{1/4}} \frac{c}{d_h} \left(\frac{\bar{W}}{U_t}\right)^2 \qquad (10)$$

where λ_R is a function of radius, as shown in Figure 42.

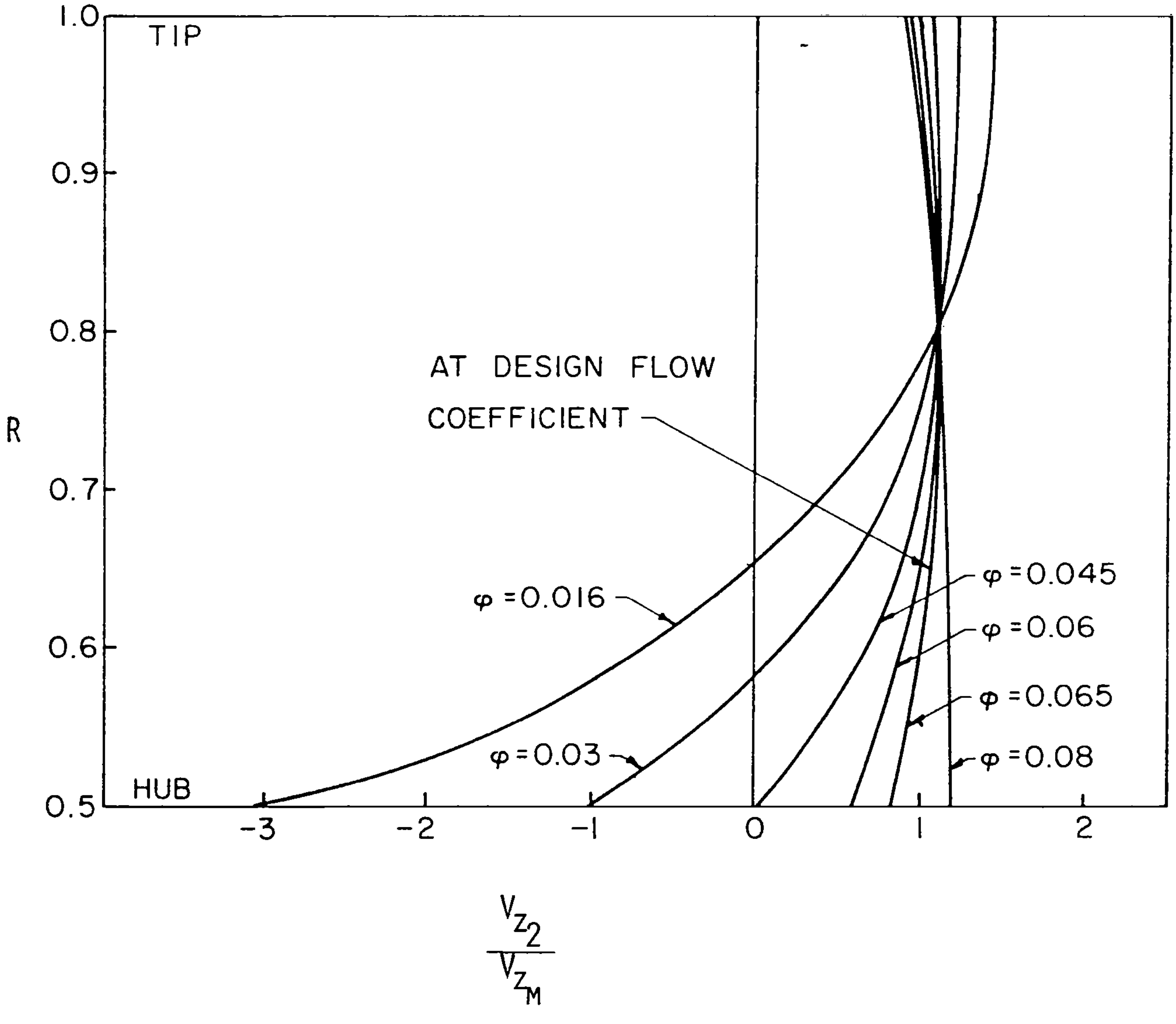

Figure 41. Variation of Outlet Axial Velocity with Radius for the Penn State Four Bladed Inducer.

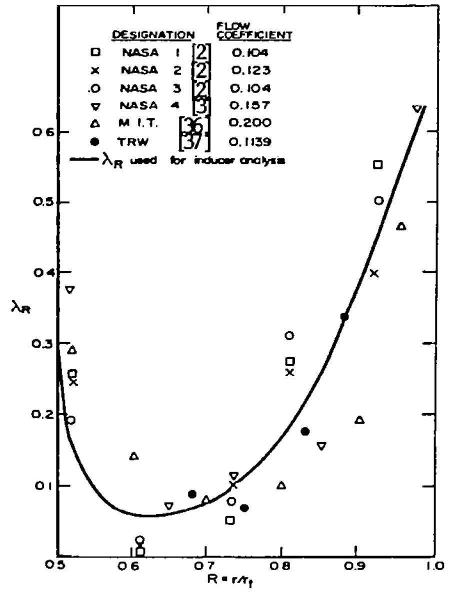

Figure 42. Radial Variation of the Modified Friction Loss Coefficients (λ_R) Calculated from Equation (10) for Various Inducer Configurations.

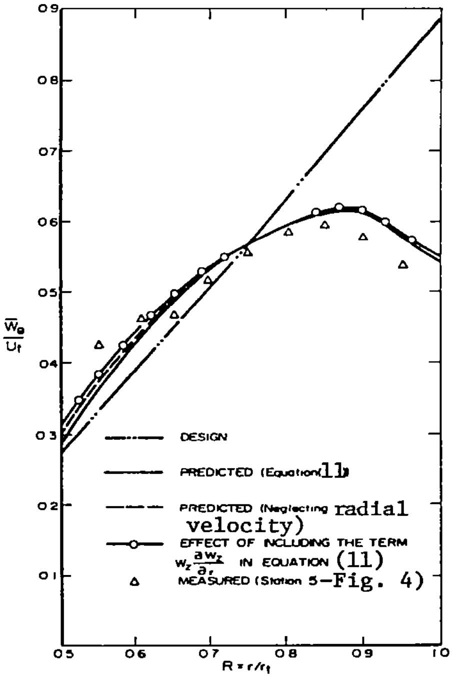

Figure 43. Predicted and Measured Relative Tangential Velocity for the Penn State's Four Bladed Inducer (Ref. 15).

A circumferentially averaged radial equilibrium equation is used to predict the relative and absolute tangential velocities. The analysis is based on suitable assumptions for the radial and main-flow velocity profiles (based on the existing three-dimensional turbulent boundary-layer data available) and loss coefficients discussed above. The circumferentially averaged radial equilibrium equation valid for inducers operating at low flow coefficients is

$$\frac{-0.275}{\sin^2 \beta} \bar{W}_\theta \left(\tan\varepsilon \frac{\partial \bar{W}_\theta}{\partial x} + \bar{W}_\theta \sec^2 \varepsilon \frac{\partial \varepsilon}{\partial x}\right) + 1.015\, \bar{W}_\theta \frac{\partial \bar{W}_\theta}{\partial r} + 1.015 \frac{\bar{W}_\theta^2}{r}$$

$$- 2\Omega \bar{W}_\theta + \frac{\partial}{\partial r} \left(\frac{\lambda_R}{R_N^{1/4}} \frac{R_{ht}}{\phi} \frac{c}{d_h} \frac{\bar{W}^2}{2}\right) = 0 \qquad (11)$$

This equation was solved with the assumption that $\bar{W}_\theta$ varies linearly with x, and by using experimental values for ε. The predictions for the Penn State inducer (four-bladed) is shown in Figure 43. Predicted values for three- and two-bladed inducers are shown in references [17] and [11], respectively. The losses and efficiencies predicted from the empirical loss correlation are shown in Figures 10 and 11, respectively.

The agreement between the theory and experiment is reasonably good. Hence, it is evident that if the frictional effects are known either empirically or analytically, the flow properties at the exit of the inducer can be predicted quite accurately. The very purpose of the boundary-layer investigation on the helical blade and a channel described earlier is to provide the most important missing link in the frictional effects, which are otherwise based on empiricism, and hence not universally valid.

The axial velocities predicted, using the continuity and axial momentum equations with assumed radial-velocity profiles and the derived tangential-velocity distribution (equation 11), agree qualitatively with the values measured from a stationary probe at the exit of a four-bladed inducer.

Approximate Viscid Analysis Based on Shear Pumping Effect

The investigations described earlier have revealed that the flow field inside these rotating passages is highly complex and three-dimensional in nature. The flow is highly turbulent and viscous both inside and outside of the rotor. Even though the inducers are designed as axial flow machinery, the radial velocities generated by viscous, coriolis, and centrifugal forces inside the blade boundary layers are found to be of the same order of magnitude as the axial velocity. The energy exchange process is complicated in terms of physical phenomena as well as mathematical description.

The conventional design and analysis procedure used in other types of pumps or compressors have to be supplemented by some innovative technique to include major viscous effects (both direct and indirect) responsible for the energy addition. The pump has to be treated as a mixed-flow pump. The axial velocity has the same effect (inviscid) as in the conventional pump. The pressure rise due to this effect is caused by incidence and camber and both static- and stagnation-head increases through the blade row.

The other contribution to the energy addition comes from the radial component of velocity arising from the coriolis and centrifugal forces in the boundary layers. These boundary layers are found to cover the entire passage, and hence the radial velocity occurs across the entire passage width. Therefore, the effect of radial velocity on head rise may be significant. The radial velocity provides a vehicle for momentum exchange between the fluid and the rotor via the shear stress. This phenomena will be referred to here as "shear pumping effect." Because of the shear stresses exerted on the flow, it is accelerated tangentially during the radial path, thus providing an additional head rise. It should be recognized here that this phenomena involves no potential flow effect or flow turning. Even though explored in connection with multiple disk shear pumps or compressors, it has never been recognized as a source of pressure rise in an axial-flow inducer which has very long and narrow passages. The major purpose of the analysis, carried out in reference [25] was to explore this effect analytically and provide for the first time an estimate of the "direct" effect of shear stresses in providing a head rise.

In this analysis, the flow is assumed to be an incompressible single phase. Blade camber and normal shear stresses as well as pressure gradient normal to the blade inside the blade boundary layer are neglected. The passage is assumed to have fully developed flow.

The equations of motion in a rotating coordinate system are integrated normal to the blade, with suitable assumptions for the velocity profiles and the skin-friction coefficient, to derive the following equation [25]:

$$\frac{d\bar{W}}{dr} - 2.2\ \Omega - 0.254\ \Omega \frac{\sin\beta}{(\tan\varepsilon)^2} + \frac{\bar{W}}{r}\left[0.127\ r \frac{\partial\beta}{\partial r} \tan\beta + \sin^2\beta \right.$$

$$\left. + 0.259 \frac{\sin\beta}{(\tan\varepsilon)^2} - 0.254 + \frac{0.075\ N}{\tan\varepsilon\cos\beta} \left(\frac{W_e r}{\nu}\right)^{-1/5}\right] = 0 \qquad (12)$$

where W is the passage-averaged velocity given by

$$\bar{W} = \frac{1}{\delta} \int_0^\delta u dy = \frac{7}{8} W_e \ .$$

Equation (3) is a first-order non-linear differential equation and can be solved from known values of $\varepsilon(r)$, Ω, $\beta(r)$ and ν.

The above expression provides an estimate for the reduction in relative velocity due to the shear pumping effect alone. It can be used to calculate the stagnation-pressure rise due to this shear pumping effect. An estimate of the total-pressure-rise coefficient can be made by the addition of the head rise due to inviscid and shear pumping effects. The predicted pressure-rise coefficient for the four-bladed inducer with aerodynamically designed blades operating at $\phi = 0.065$ is shown compared with the measured values in Figure 44. It is evident that the steep head rise characteristics observed here as well as by others [1-4] are partly due to the shear pumping effect. The agreement between the theory and the experiment, shown in Figure 44, is only reasonable. The discrepancy may well be due to the three-dimensional invicid effects, which are not accounted for in the "mean streamline method," as well as leakage and secondary flows that exist in this region.

Three-Dimensional Inviscid Analysis (Exact)

An analysis was carried out in reference [17] to predict the inviscid effects of blade blockage at the exit of a three-bladed inducer, an extension of the analogous source actuator theory for the effects of radially varying blade thickness developed by Lewis and Horlock [38]. It is concluded [17] that the perturbation of the meridional flow caused by the radially varying blade blockage is not negligible for the Penn State inducers. The analysis predicts perturbation of up to 10 percent in axial velocity at the exit. The axial velocity profile derived from this analysis agrees qualitatively with the experiment.

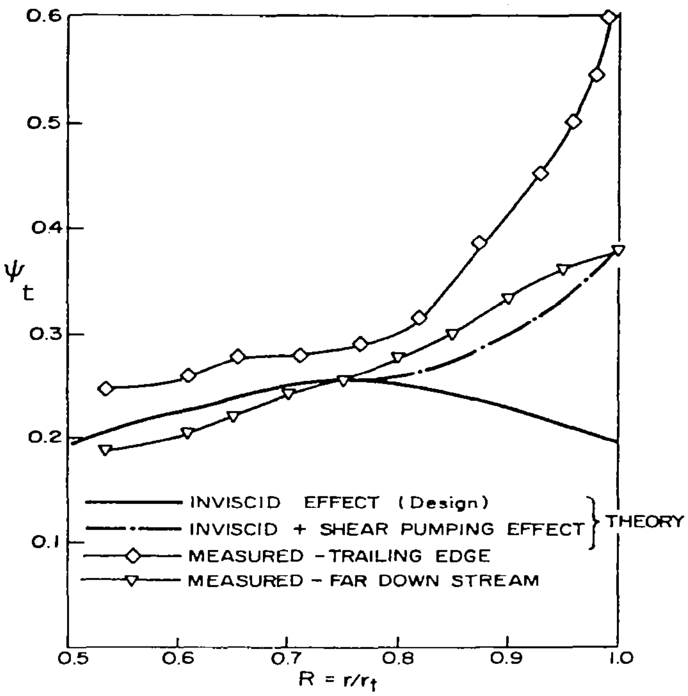

Figure 44. Radial Variation of Absolute Stagnation Pressure Coefficient (ψ_t) for Four Bladed Inducer with Cambered Blades (Ref. 25).

An estimate of the nature and magnitude of secondary flows caused by the turning of the hub and wall boundary layers is formulated in reference [12]. The analysis indicates that the strength of secondary vortices near the hub is higher than those near the annulus wall. This has been qualitatively confirmed by a visualization experiment [12]. The secondary flow near the hub wall has a tendency to overturn the absolute flow, thus increasing the tangential velocity and decreasing the axial velocity. This is probably one of the mechanisms responsible for low axial velocities near the hub.

A thorough knowledge of all significant inviscid effects (blade blockage, flow turning, finite hub/tip ratio, etc.) and viscid effects (boundary layer growth, energy dissipation, etc.) is essential in the accurate prediction of the flow in all turbomachinery. Relevant to this, the availability of modern computers with large storage capacities and fast computation times greatly enhance the possibility of numerically solving the complete equations of motion. One of the early investigations in this area was made by Cooper and Bosch [35] for three-dimensional inviscid flow through axial flow inducers. Application of this method of analysis to the Penn State inducer was carried out in references [14], [17], [18], and [21]. Modifications to the Cooper-Bosch method have been attempted to reduce convergence time of the solution and to provide a viscid solution capability based on the empirically determined blade skin friction coefficients. A method of initializing the blade flow parameters as input to the Cooper-Bosch method has also been attempted in a search for a faster convergence to the solution. A new technique for satisfying the Kutta condition at the trailing edge has been incorporated into the program.

This method developed by Cooper and Bosch [35] solves the momentum and continuity equations iteratively in three dimensions for a finite grid of points representing the channel between the blades. The non-linear partial differential equations governing the flow in a rotating polar coordinate system r, θ, z are:

r momentum

$$\frac{g_o}{\rho}\frac{\partial p}{\partial r} + W_r\frac{\partial W_r}{\partial r} + \frac{W_\theta}{r}\frac{\partial W_r}{\partial \theta} + W_z\frac{\partial W_r}{\partial z} - \frac{1}{r}(W_\theta + r\Omega)^2 + F_r = 0 \qquad (13)$$

θ momentum

$$\frac{g_o}{\rho}\frac{\partial p}{\partial \theta} + W_r\frac{\partial W_\theta}{\partial r} + \frac{W_\theta}{r}\frac{\partial W_\theta}{\partial \theta} + W_z\frac{\partial W_\theta}{\partial z} + \frac{W_r W_\theta}{r} + 2\,W_r\Omega + F_\theta = 0 \qquad (14)$$

z momentum

$$\frac{g_o}{\rho}\frac{\partial p}{\partial z} + W_r \frac{\partial W_z}{\partial r} + \frac{W_\theta}{r}\frac{\partial W_z}{\partial \theta} + W_z \frac{\partial W_z}{\partial z} + F_z = 0 \tag{15}$$

continuity

$$\frac{W_r}{r} + \frac{\partial W_r}{\partial \theta} + \frac{1}{r}\frac{\partial W_\theta}{\partial \theta} + \frac{\partial W_z}{\partial z} + \frac{1}{\rho}\left(W_r \frac{\partial \rho}{\partial r} + \frac{W_\theta}{r}\frac{\partial \rho}{\partial \theta} + W_z \frac{\partial \rho}{\partial z}\right) = 0 \tag{16}$$

where W_z, W_θ, and W_r are relative velocities in the axial, tangential, and radial directions, respectively. F_r, F_θ, and F_z are the components of the body forces, including viscous terms, and are zero for the inviscid case considered in this section. In the Cooper-Bosch method, the above equations are rearranged to give residuals which are reduced to zero by a relaxation procedure. The total residual (RT) of one relaxation cycle is calculated by

$$RT = \sum_{i=1}^{IMAX} \sum_{j=1}^{JMAX} \sum_{k=1}^{KMAX} \left[(R1)^2 + (R2)^2 + (R3)^2 + (R4)^2\right]_{i,j,k} \tag{17}$$

where R1, R2, R3, and R4 are the residuals calculated for the three momentum equations (13-15) and the continuity equation (16), and IMAX, JMAX, and KMAX are the number of grid stations in the radial, tangential, and axial directions, respectively, which are used in the numerical analysis.

From this, the total root mean square (RMS) residual is defined as

$$RMS = \sqrt{\frac{(RT)^2}{4\cdot(IMAX)\cdot(JMAX)\cdot(KMAX)}}$$

and is thus a measure of the degree of convergence between the iterated solution and the exact solution. In applying this method to the Penn State inducer, the flow is assumed to be incompressible, and a grid of 7 x 7 x 26 is chosen to represent the blade passage. The flow geometry is shown in Figure 45. The boundary condition to be satisfied on the hub, annulus walls, and blade surfaces is $\vec{W} \cdot \vec{n} = 0$, where $\vec{n}$ is the direction normal to the channel boundaries and $\vec{W}$ is the total relative velocity.

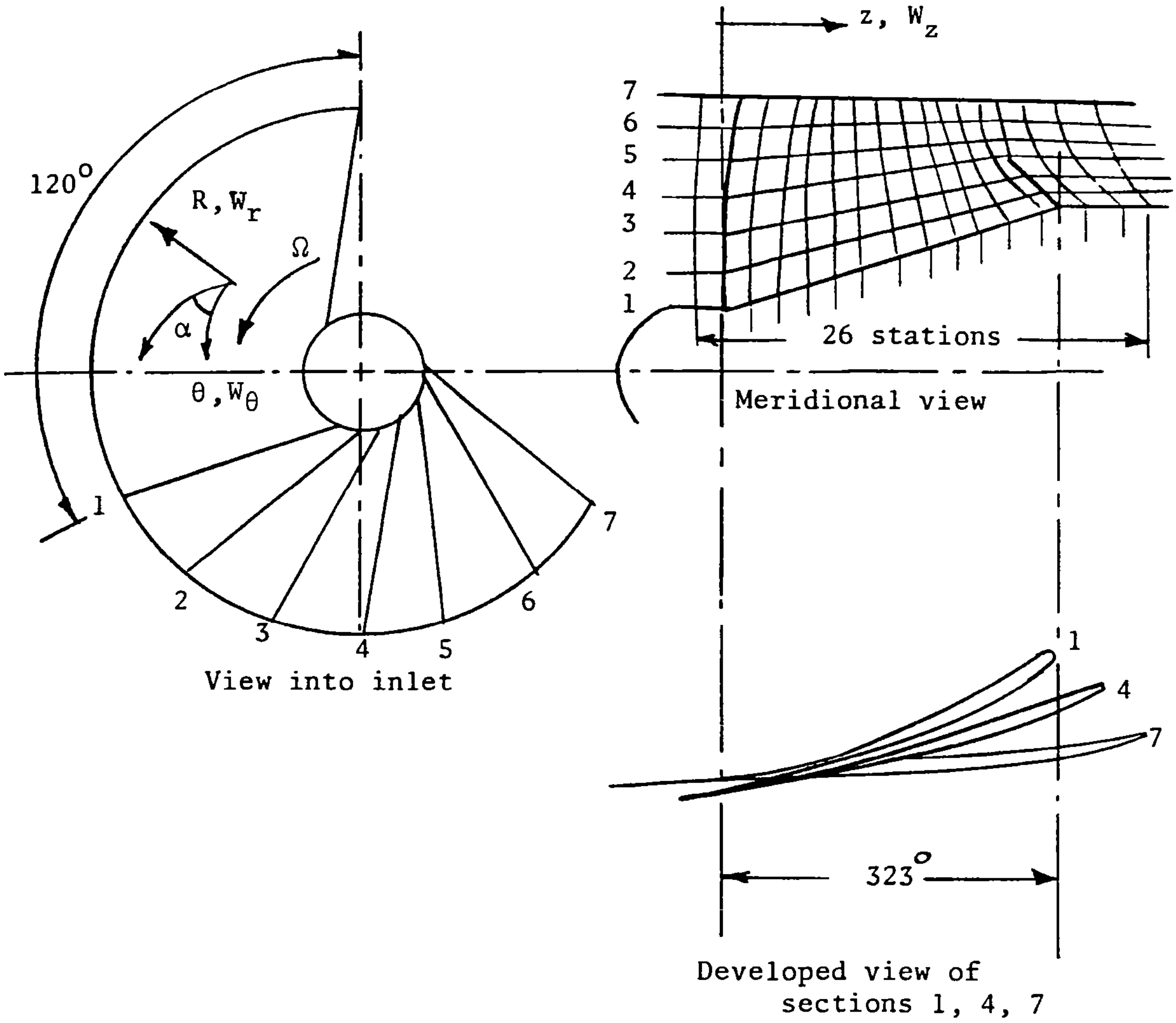

Figure 45. Inducer Geometry for Numerical Analysis

For increased efficiency, the program has been compiled under a Fortran IV H level optimization procedure, which reduces the time required for repetitive calculations, and production runs were submitted using the resulting object card deck. Output results from the computer program were placed onto 9-track, 1600 BPI (bits per inch) magnetic computer tape for future accessibility.

The initial estimation for the velocity and static pressure distribution throughout the inducer flow passage is calculated by the two-dimensional Douglas-Neumann program for a cascade, described in detail in reference [39]. The technique employed by the Neumann program to solve a particular fluid-flow problem is to use source distributions of appropriate strength on the surface of the blade profile in such a way that the flow normal to the surface of the body is either zero or prescribed. This solution was modified to include three-dimensional effects, approximately, using the solution of Lakshminarayana and White [40] for the effects of converging or diverging ducts on the airfoil performance.

Using the input parameters of velocity and pressure derived from the preceding analysis results in a lower total RMS residual than with the previous method of initializing the input variables. As an example, the final RMS residual for the inviscid results of reference [17] was 0.12450 after 68 relaxation cycles, whereas a similar value is obtained using the analysis in references [18, 21] in 10 relaxation cycles. This amounts to a considerable saving in computer time. Twenty-five iteration cycles have reduced the RMS residual to 0.10579, indicating that a faster convergence to the solution should be possible.

Since the extension of the stagnation stream surfaces downstream have been constructed to be uniformly periodic with a spacing of $2\pi/N$ (N being the number of blades), the values of velocity and pressure at the downstream tangential channel boundaries should be equal. This condition is applied at the blade trailing edge after each iteration cycle. If the pressure and suction surface parameters differ with each other at the trailing-edge grid point, the average value is used in the residual calculations. Changes made to the original Cooper-Bosch program are given in Appendix B of reference [18] and are concentrated in subroutine "MAIN." This program was run for the three-bladed configuration. Some of the results and their interpretation are discussed in the next section.

Three-Dimensional Viscid Analysis Based on Empirical Wall Shear Stress

A method incorporating some of the major effects of viscosity was presented in references [18] and [21]. In this formulation, the major viscous terms in equations (13)-(16) are retained and modelled. The expressions for F_r, F_θ, and F_z are given by

$$F_r = -\frac{1}{\rho}\left[\frac{\partial\tau_{r\theta}}{r\partial\theta} + \frac{\partial\tau_{rz}}{\partial z} + \frac{\partial\sigma_{rr}}{\partial r} + \frac{(\sigma_{rr} - \sigma_{\theta\theta})}{r}\right]$$

$$F_\theta = -\frac{1}{\rho}\left[\frac{\partial\sigma_{\theta\theta}}{r\partial\theta} + \frac{\partial\tau_{\theta z}}{\partial z} + \frac{\partial\tau_{\theta r}}{\partial r} + \frac{2}{r}\tau_{\theta r}\right]$$

$$F_z = -\frac{1}{\rho}\left[\frac{\partial\tau_{z\theta}}{r\partial\theta} + \frac{\partial\sigma_{zz}}{\partial z} + \frac{\partial\tau_{rz}}{\partial r} + \frac{\tau_{rz}}{r}\right]$$

where τ is the shear stress and σ is the normal stress. For example, $\tau_{r\theta}$ in the shear stress in r direction is a plane perpendicular to θ. σ_{rr} is the normal stress in a plane normal to r direction.

Since the stagger angle is very large, these viscous terms can be approximated by retaining the dominant terms as well as neglecting the normal shear stresses, resulting in:

$$F_r = -\frac{1}{\rho}\frac{\partial\tau_{rz}}{\partial z}$$

$$F_\theta = -\frac{1}{\rho}\frac{\partial\tau_{\theta z}}{\partial z}$$

$$F_z = -\frac{1}{\rho}\frac{\partial\tau_{z\theta}}{r\partial\theta} \quad .$$

The distribution of shear stress is assumed to be linear across the flow passage from the pressure surface to the suction surface. The values of wall shear stresses are assumed to be known empirically. Skin-friction coefficient (C_f) data for a four-blade flat-plate helical channel presented in reference [22] is used in this program. Details of incorporating this into the main program are discussed in references [18] and [21].

An additional requirement placed on the viscid analysis is to satisfy the viscid boundary condition, which requires that all components of velocity are zero at the blade surface.

The changes to the original Cooper-Bosch exact program necessitated by the inclusion of the viscous loss terms are made in subroutines "MAIN," DLOSS," and "RESID." Flow chart diagrams for the modified subroutines of the Cooper-Bosch program are given in Appendix A of reference [18], and a complete Fortran listing of the modified program is given in Appendix B of that study. The computer time required for one complete run is approximately two to three times more than for a corresponding inviscid program.

Comparison of the results of the Cooper-Bosch inviscid and viscid analyses and their relationship to experimental measurements for a three-bladed inducer are given in Figures 34 and 38. The inviscid program was run for approximately 75 relaxation cycles, resulting in a total RMS residual of 0.077. The viscid program was run for approximately 50 cycles and produced a total RMS residual of 0.200.

The inducer blade static-pressure distributions derived from the exact inviscid analysis are plotted in Figure 34 at the locations corresponding to the experimental ψ_s measuring stations. As can be seen, the results agree remarkably well at all radial stations, especially for those near the hub (radial stations A and B--Figure 4). Near the tip region, the experimental pressure surface ψ_s distributions agree closely with the numerical analysis while the suction surface ψ_s distributions show the most discrepancy. The ψ_s distributions obtained from the viscid analysis program are also plotted in Figure 34. The general shape of the viscid analysis ψ_s distribution closely resembles that of the inviscid analysis. Greatest variation between viscid and inviscid analyses are shown at the tip (radial station E), where the viscous effects are dominant.

Inviscid analysis results for the total relative velocity distribution at station 2 for three-bladed inducer are plotted in Figure 38. Magnitudes of W near the tip are comparable to those found experimentally, whereas near the hub the inviscid velocities are significantly lower than the predicted results. The viscid analysis prediction for the total relative velocity distribution is also shown in Figure 38. It is a striking departure from the inviscid analysis distribution, especially near the tip where the viscous effects are known to be appreciable. The viscid analysis also provides crude approximations for the suction and pressure surface boundary layers. A large velocity deficiency near the tip is predicted at approximately 50 percent passage width and agrees favorably with the experimental W profiles plotted in Figure 38. It is apparent [18] that the velocity deficiency noted near the tip at station 1 grows considerably as the flow proceeds downstream to station 2 (Figure 4), indicating an increase in size and intensity of the viscous loss region and substantiating the experimental results.

The suction surface boundary layer appears thicker than the pressure surface boundary layer at all radii, increasing in thickness from hub to tip. This observation is consistent with experimental results and conforms with previous discussions on boundary layer interaction and flow mixing near the tip. Figure 38 also shows the axial velocity distribution predicted from the inviscid analysis. There is a definite decrease in axial velocity from hub to tip, which appears to indicate the presence of the blade blockage effect within the flow passage. This observation is consistent with the experimental results plotted in Figure 38. The viscid analysis results for the axial velocity distributions indicate the approximate profiles for the pressure and suction surface boundary layers. The axial velocity profile decreases in magnitude from hub to tip and tends to confirm the presence of the blade blockage effect at this location. The axial velocity profiles predicted from the viscid analysis appear to more closely approximate the experimental distributions.

The prediction of radial velocity is at best qualitative. The reasons for this are discussed in references [18] and [21].

The viscid analysis is approximate due to the various assumptions and simplifications made. In particular, the viscid boundary conditions imposed on the solution are rather drastic, since the grid geometry spacing used in the exact analysis is relatively large. More tangential grid stations would be needed, especially close to the blade surface, to better define the shape of the blade boundary layer.

SIGNIFICANCE AND APPLICATION OF RESULTS

Generalization, Significance, and Application to Turbomachinery

The major significance of the research carried out hitherto is a good understanding of the flow in turbomachinery under conditions where the real fluid effects are at least equally important to the ideal fluid effects which form the basis of existing design methods of turbomachinery. It is hoped that the results obtained would help establish a theoretical model for the eventual analysis and design of turbomachinery dominated not only by viscous and turbulence effects inside the turbomachinery passages, but also by the secondary flow and other interaction effects near the end-wall regions. Among the results that are of general validity to turbomachinery design, analysis, and research techniques are:

1. The prediction of boundary layer growth on turbomachinery blades: The three-dimensional velocity profile analysis, skin friction correlation developed and the knowledge of turbulence quantities gained during the course of this program should significantly improve the existing methods of computing the boundary layer on all types of turbomachinery blades.

2. With the advent of large, high-speed digital computers, techniques have been developed for the solution of three-dimensional inviscid equations of turbomachinery. It is anticipated that the analytical and experimental investigations reported here would lead to an eventual development of a three-dimensional viscid program that includes all the dominant viscous and turbulence terms.

3. The end-wall flow in a compressor or turbine is very poorly understood. The existing knowledge and prediction is based on superposition of leakage and secondary flows, ignoring the interaction between annulus wall and blade boundary layer. Measurements at the tip of a single blade and those derived inside the helical channel have provided an understanding of the interaction effects, which would eventually lead to techniques of minimizing these effects. One of the major outcomes of the measurements in a single rotating blade is the observation of a core located away from the blade surface at the tip. This effect, which has been neither observed nor reported earlier, is of great significance in understanding and analyzing the end-wall flow in turbomachinery.

4. Measurement of the relative flow has very rarely been attempted earlier. Knowledge of this measurement, gained through this program, is essential in the design, analysis, and improvement of turbomachinery performance.

5. In the field of instrumentation, the techniques developed here for the measurement of three-dimensional instantaneous velocities as well as turbulence intensities with the use of rotating as well as stationary hot-wire probes are of major significance. The program includes not only the direct measurement of skin friction, but also the development of remotely controlled traversing mechanisms for velocity profile measurement inside the rotating passages.

6. The program has provided a large amount of accurate data for the boundary layer on rotating blades and in rotating channels. These could be utilized by investigators presently involved in the development of computer codes.

7. A thorough understanding of the interaction of the pressure surface and suction surface boundary layers with the end-wall boundary layer has been achieved through a detailed measurement of the velocity and turbulence quantities by means of a tri-axial hot wire.

8. The skin friction correlation developed during this program takes into account the effect of the rotation as well as the pressure gradient. This should be a useful correlation for the design and analysis of viscous effects on turbomachinery rotor blades.

9. New methods of approximate and exact analyses, which include the use of the empirical loss correlation and the empirical skin-friction coefficient, developed during this program should be useful in analyzing other types of turbomachinery.

Significance and Application to Inducer Analysis and Design

Major achievements that are applicable to design and analysis of inducers in addition to those listed in the foregoing section, are:

1. The major thrust of the initial phase of the program was directed towards the physical understanding of the flow, both qualitative and quantitative, with a view towards the development of design philosophy and the theoretical model of the flow. This has been accomplished by visual observation and quantitative measurement, both at the exit and inside the passages, using both conventional and hot-wire probes. The theoretical modelling of the flow, based on this physical understanding of it, was pursued. The radial velocities are of the same order of magnitude as the axial velocities, hence inclusion of these as well as the dominant turbulence terms is essential for the accurate prediction of the flow.

2. The rotation-induced radial flow substantially changes the boundary-layer growth characteristics, showing that two-dimensional calculations are inapplicable to cases of the sort under consideration. The boundary layer calculation method proposed here is quite satisfactory, except for the limitations mentioned. The radial velocity profile developed and the skin-friction correlation proposed have led to considerable improvement in prediction techniques.

3. The inner part of the rotor (hub to mid-radius) could be designed from inviscid considerations, but the design of the outer part (mid-radius to tip) should take into account the "drag or shear" pumping effect. Measurements taken in a helical channel at zero incidence substantiate this argument. These measurements show characteristics very similar to the inducer near the outer part of the blade (mid-radius to tip), showing the dominant influence of viscosity and turbulence on head rise characteristics.

4. The semi-empirical friction loss coefficient developed and used for the prediction of head rise characteristics, even though unsatisfactory in view of our better insight into the loss mechanism, could serve as a useful tool in the preliminary design or analysis of turbomachinery.

5. The physical reasons for the back-flow near the hub (at the exit) have been established. These are caused by large secondary flows that exist in this region and the radial migration inside the wakes. Based on these investigations, it should be possible to attempt minimization of the sources causing such backflow.

6. A two-bladed inducer has the best performance in terms of uniformity in head rise and the tangential velocity, even though there is a slight deterioration in axial velocity profile. The mass-averaged stagnation-pressure rise is also found to be highest for the two-bladed inducer. The performance deteriorates with an increase in the number of blades, which is especially true for the four-bladed inducer. These results provide a design criterion in the selection of solidity in inducers.

REFERENCES

1. Acosta, A. J.: An Experimental Study of Cavitating Inducers. Proceedings of Second Symposium on Naval Hydrodynamics, Washington, D.C., August 1958, pp. 533-557.

2. Sandercock, D. M.; Soltis, R. F.; and Anderson, D. A.: Cavitation and Non-Cavitation Performance of 80.6° Flat Plate Helical Inducer at Three Rotational Speeds. NASA Technical Note D-1439, November 1962.

3. Soltis, R. F.; Anderson, D. A.; and Sandercock, D. M.: Investigation of the Performance of a 78° Flat Plate Helical Inducer. NASA Technical Note D-1170, March 1962.

4. Anderson, D. A.; Soltis, R. F.; and Sandercock, D. M.: Performance of an 84° Flat Plate Helical Inducer and Comparison with Performance of a Similar 78° and 80.6° Inducers. NASA Technical Note D-2553, December 1964.

5. Wislicenus, G. F. and Lakshminarayana, B.: Design of a Test Inducer. NASA Contractor Report CR-67129, 1965.

6. McCafferty, H. G.: Errors in Measuring the Fluctuating Flow at the Discharge of an Inducer. M.S. Thesis, Department of Aerospace Engineering, The Pennsylvania State University, 1967.

7. Lakshminarayana, B.: Investigations and Analysis of Flow Phenomena of Secondary Motions in Axial Flow Inducers. NASA Contractor Report CR-103291, June 1969.

8. Jabbari, A.: Turbulent Boundary Layer Characteristics on a Rotating Helical Blade. M.S. Thesis, Department of Aerospace Engineering, The Pennsylvania State University, 1969 (also as NASA Contractor Report CR-105649, NASA STAR Index N69-36288, September 1969).

9. Poncet, A.; Yamaoka, H.; and Lakshminarayana, B.: Investigations and Analysis of Flow Phenomena of Secondary Motions in Axial Flow Inducers. NASA Contractor Report CR-107267, July 1970.

10. Yamaoka, H.; Lakshminarayana, B.; and Anand, A. K.: Investigations and Analysis of Flow Phenomena of Secondary Motions in Axial Flow Inducers. Report to NASA, July 1971.

11. Lakshminarayana, B. and Anand, A. K.: Solidity Effects in Axial Flow Inducers. Proceedings of Second International J.S.M.E. Conference on Fluid Machinery and Fluidics, Tokyo, September 1972, pp. 157-166.

12. Lakshminarayana, B.: Visualization Study of Flow in Axial Flow Inducers. Journal of Basic Engineering, December 1972, pp. 777-787.

13. Lakshminarayana, B.; Jabbari, A.; and Yamaoka, H.: Turbulent Boundary Layer on a Rotating Helical Blade. Journal of Fluid Mechanics, Vol. 51, Pt. 3, 1972, pp. 545-569.

14. Anand, A. K.; Gorton, C. A.; Lakshminarayana, B.; and Yamaoka, H.: Investigation of Boundary Layer and Turbulence Characteristics Inside the Passages of an Axial Flow Inducer. NASA Contractor Report CR-121248, July 1973.

15. Lakshminarayana, B.: Experimental and Analytical Investigation of Flow Through a Rocket Pump Inducer. Fluid Mechanics Design, and Acoustics of Turbomachinery, NASA SP 304, Part II, 1974, pp. 690-731.

16. Lakshminarayana, B.: Three Dimensional Flow in Rocket Pump Inducers, Part 1: Measured Flow Field Inside the Rotating Blade Passage and at the Exit. Journal of Fluids Engineering, December 1973, pp. 567-578.

17. Poncet, A. and Lakshminarayana, B.: Investigations of Three-Dimensional Flow Characteristics in a Three Bladed Rocket Pump Inducer. NASA Contractor Report CR-2290, 1973.

18. Gorton, C. A. and Lakshminarayana, B.: Analytical and Experimental Study of the Three-Dimensional Mean Flow and Turbulence Characteristics Inside the Passages of an Axial Flow Inducer. NASA Contractor Report CR-134682, 1974.

19. Lakshminarayana, B. and Poncet, A.: A Method of Measuring Three-Dimensional Wakes in Turbomachinery. Journal of Fluids Engineering, Transactions ASME, Vol. 96, No. 2, June 1974, pp. 87-91 (discussion in Journal of Fluids Engineering, Vol. 97, Ser. I, No. 4, December 1975, pp. 627-628).

20. Gorton, C. A. and Lakshminarayana, B.: A Method of Measuring the Three Dimensional Mean Flow and Turbulence Characteristics Inside a Rotating Turbomachinery Passage. Journal of Engineering for Power, Vol. 98, No. 2, April 1976, pp. 137-146.

21. Lakshminarayana, B. and Gorton, C. A.: Three Dimensional Flow Field in Rocket Pump Inducers, Part 2: Three Dimensional Viscid Flow Analysis and Hot Wire Data on Three Dimensional Mean Flow and Turbulence Inside the Rotor Passage. Journal of Fluids Engineering, Vol. 99, Ser. I, No. 1, March 1977, pp. 176-186.

22. Anand, A. K. and Lakshminarayana, B.: Three Dimensional Turbulent Boundary Layer in a Rotating Channel. Journal of Fluids Engineering, June 1975, pp. 197-210.

23. Anand, A. K. and Lakshminarayana, B.: An Experimental and Theoretical Investigation of Three Dimensional Turbulent Boundary Layer Inside the Passage of a Turbomachinery Rotor. NASA Contractor Report CR-2888, 1977.

24. Anand, A. K. and Lakshminarayana, B.: An Experimental Study of Three Dimensional Boundary Layers and Turbulence Characteristics Inside a Rotating Channel. Journal of Engineering for Power, Vol. 100, No. 4, 1978, pp. 676-690.

25. Lakshminarayana, B.: On the Shear Pumping Effect in Rocket Pump Inducers. Book chapter in Pumps--Analysis, Design and Application, Vol. 1, Worthington Pump Inc., 1978, pp. 49-68.

26. Wislicenus, G. F.: Fluid Mechanics of Turbomachinery, Dover, Vol. II, 1965, pp. 646-683.

27. Gracey, .: Wind Tunnel Investigation of a Number of Total Pressure Probes at High Angles of Attack, Subsonic, Transonic and Supersonic Speeds. NACA Report 1303, 1957.

28. Lakshminarayana, B.: Techniques for the Measurement of Rotor Flow in Turbomachinery. Proceedings of ASME Symposium on Measurement Methods in Rotating Components of Turbomachinery, Edited by B. Lakshminarayana and P. Runstadler, Jr., 1980 (to be published in the Journal of Engineering for Power, 1981).

29. Ravindranath, A. and Lakshminarayana, B.: Three Dimensional Mean and Turbulence Flow Characteristics of the Near Wake of a Compressor Rotor Blade. NASA CR 159518, May 1980.

30. Lakshminarayana, B. and Wislicenus, G. F.: Investigations and Analysis of Flow Phenomena in Axial Flow Inducers. Report to NASA, August 1965.

31. Iura, T.: Discussion of Reference [1], p. 554.

32. Mager, A.: Generalization of Boundary Layer Momentum Integral Equations to Three Dimensional Flow Including Those of Rotating Systems. NASA Report 1067, 1952.

33. Klebanoff, P. S.: Characteristics of Turbulence in a Boundary Layer with Zero Pressure Gradient. NASA Report 1247, 1955.

34. Huppert, M. C., et al.: Some Cavitation Problems in Rocket Propellant Pumps. Unpublished report, Rocketdyne.

35. Cooper, P. and Bosch, H.: Three Dimensional Analysis of Inducer Fluid Flow. NASA Contractor Report CR-54836, TRW ER-6673A, February 1966.

36. Mullan, P. J.: An Investigation of Cavitating Inducers for Turbopumps. M.I.T. Gas Turbine Lab. Report 53, May 1959.

37. Bosch, H. B., et al.: Advanced Inducer Study. TRW ER-5288, May 1963.

38. Lewis, R. I. and Horlock, J. H.: Flow Disturbances Due to Blade Thickness in Turbomachines. Journal of Mechanical Engineering Science, Vol. 11, No. 1, 1969.

39. Giesing, J. P.: Extension of the Douglas-Neumann Program to Problems of Lifting, Infinite Cascades. Douglas Aircraft Division Report LB-31653, July 1964.

40. Lakshminarayana, B. and White, M. T.: Airfoil in a Contracting or Diverging Stream. Journal of Aircraft, Vol. 9, No. 5, May 1972, pp. 354-360.

1. Report No.
NASA CR-3471

2. Government Accession No.

3. Recipient's Catalog No.

4. Title and Subtitle
ANALYTICAL AND EXPERIMENTAL STUDY OF FLOW PHENOMENA IN NONCAVITATING ROCKET PUMP INDUCERS

5. Report Date
October 1981

6. Performing Organization Code

7. Author(s)
B. Lakshminarayana

8. Performing Organization Report No.
PSU-TURBO-R81-3

10. Work Unit No.

9. Performing Organization Name and Address
The Pennsylvania State University
Department of Aerospace Engineering
233 Hammond Building
University Park, Pennsylvania 16802

11. Contract or Grant No.
NGL-39-009-007

13. Type of Report and Period Covered
Contractor Report

12. Sponsoring Agency Name and Address
National Aeronautics and Space Administration
Washington D.C. 20546

14. Sponsoring Agency Code
505-32-52

15. Supplementary Notes
Final report. Project Manager, Werner R. Britsch, Transport Propulsion Office, NASA Lewis Research Center, Cleveland, Ohio 44135.

16. Abstract

The investigation of the flow phenomena in rocket pump inducers is summarized in this report. All the experimental investigations were carried out with air as the test medium. The major characteristic features of the rocket pump inducers are low flow coefficient (0.05 to 0.2), large stagger angle (70° to 85°) and high-solidity (few blades of very long chord length as opposed to short chord of many bladed compressor rotor) blades of little or no camber. The resulting configuration, even though beneficial from the point of view of cavitation, results in highly viscous, turbulent, and almost invariably, fully developed flow inside these passages. While the characteristic form of the inducer is dictated by the cavitation requirements, the flow is subjected to major effects of viscosity and turbulence of the flow in the long and narrow passages. The investigations reported here are concerned with the effect of viscosity, not the effects of cavitation. One of the major objectives of this investigation is to understand the flow phenomena in these inducers, through flow visualization, conventional and hot-wire probe measurement inside and at the exit of the blade passage, and to provide analytical methods above, the experimental was carried out using four-, three-, and two-bladed inducers with cambered blades. Both the passage and the exit flow were measured. The basic research and boundary layer investigation was carried out using a helical flat plate (of same dimensions as the inducer blades tested), and a flat plate helical inducer (four-bladed). Detailed mean and turbulence flow field inside the passage as well as the exit of the rotor were derived from these measurements. The boundary layer, endwall and other passage data revealed extremely complex nature of the flow, with major effects of viscosity present across the entire passage. Several analyses were carried out to predict the flow field in inducers. These included an approximate analysis, the shear pumping analysis, and a numerical solution of exact viscous equations with approximate modelling for the viscous terms. The agreement between these analyses and the experiment is reasonably good.

17. Key Words (Suggested by Author(s))
Rocket pump inducer
Turbomachinery
Three dimensional flow

18. Distribution Statement
Unclassified - unlimited
STAR Category 02

19. Security Classif. (of this report)	20. Security Classif. (of this page)	21. No. of Pages	22. Price*
Unclassified	Unclassified	101	A06

* For sale by the National Technical Information Service, Springfield, Virginia 22161

NASA-Langley, 1981